University of Kentucky Doctoral Dissertations   Graduate School

2003

TRANSMISSION ELECTRON MICROSCOPY AND FLOW FIELD-FLOW FRACTIONATION: EXPLORATION OF THE NANOSCOPIC COMPONENTS IN PARTIALLY REDUCED POLYOXOMOLYBDATES BY KINETIC PRECIPITATION WITH DE NOVO ORGANIC MOLECULES

Yan Zhu
University of Kentucky, yzhu1@uky.edu

Right click to open a feedback form in a new tab to let us know how this document benefits you.

ABSTRACT OF DISSERTATION

Yan Zhu

The Graduate School

University of Kentucky

2003

TRANSMISSION ELECTRON MICROSCOPY AND FLOW FIELD-FLOW
FRACTIONATION: EXPLORATION OF THE NANOSCOPIC COMPONENTS IN
PARTIALLY REDUCED POLYOXOMOLYBDATES BY KINETIC
PRECIPITATION WITH *DE NOVO* ORGANIC MOLECULES

_____

ABSTRACT OF DISSERTATION

_____

A dissertation submitted in partial fulfillment of the
requirements for the degree of Doctor of Philosophy
in the college of Arts and Sciences
at the University of Kentucky

By

Yan Zhu

Lexington, Kentucky

Director: Dr. Arthur Cammers-Goodwin, Associate Professor of Chemistry

Lexington, Kentucky

2003

ABSTRACT OF DISSERTATION

TRANSMISSION ELECTRON MICROSCOPY AND FLOW FIELD-FLOW
FRACTIONATION: EXPLORATION OF THE NANOSCOPIC COMPONENTS IN
PARTIALLY REDUCED POLYOXOMOLYBDATES BY KINETIC
PRECIPITATION WITH *DE NOVO* ORGANIC MOLECULES

Although molybdenum blue solutions have been known for more than two
centuries, an understanding of their chemical nature is only beginning to emerge.
This dissertation aimed at elucidating the structural nature of the polydisperse,
nanoscopic components in the solution phases and the solid states of partially
reduced polyoxomolybdate (Mo-POM). The study offered at least four
contributions to the area: (1) a rational protocol for the molecular recognition of
Mo-POM with *de novo* organic hosts. (2) demonstration of kinetic precipitation of
a dynamic mixture of polyoxomolybdates and application of the technique to the
study of the dynamic mixture by TEM (3) characterization of the Mo-POM
nanostructures by an unusual combination of complementary analytical
techniques. (4) a general approach for the synthesis of crown-ethers-containing
tripodal molecules.

The molecular recognition of Mo-POM with designer tripodal hexamine-
tris-crown ethers opened a window to the solution phase structures of Mo-POM

nanoscopic components. Studies with a series of structurally analogous hosts probed the relationship between the structure of the molecular host and the formation of nanostructures.

An unusual combination of complementary analytical protocols: flow field-flow fractionation, electron microscopy (transmission and scanning), and inductively coupled plasma – emission spectroscopy, was used to monitor the solution-phase evolution of Mo-POM nanostructures. The crystallization – driven formation of keplerate Mo-POM and solution-phase evolution of structurally related nanoscopic species were apparent in the self-assembling process of partially reduced Mo-POM.

KEYWORDS: Molecular recognition, Nanostructure, Polyoxomolybdate, Electron microscopy, Field flow fractionation

Yan Zhu

November 25, 2003

TRANSMISSION ELECTRON MICROSCOPY AND FLOW FIELD-FLOW
FRACTIONATION: EXPLORATION OF THE NANOSCOPIC COMPONENTS IN
PARTIALLY REDUCED POLYOXOMOLYBDATES BY KINETIC
PRECIPITATION WITH *DE NOVO* ORGANIC MOLECULES

By

Yan Zhu

Dr. Arthur Cammers-Goodwin
(Director of Dissertation)

Dr. Mark S. Meier
(Director of Graduate Studies)

RULES FOR THE USE OF DISSERTATIONS

DISSERTATION

Yan Zhu

The Graduate School

University of Kentucky

2003

TRANSMISSION ELECTRON MICROSCOPY AND FLOW FIELD-FLOW
FRACTIONATION: EXPLORATION OF THE NANOSCOPIC COMPONENTS IN
PARTIALLY REDUCED POLYOXOMOLYBDATES BY KINETIC
PRECIPITATION WITH *DE NOVO* ORGANIC MOLECULES

_____

DISSERTATION

_____

A dissertation submitted in partial fulfillment of the
requirements for the degree of Doctor of Philosophy
in the college of Arts and Sciences
at the University of Kentucky

By

Yan Zhu

Lexington, Kentucky

Director: Dr. Arthur Cammers-Goodwin, Associate Professor of Chemistry

Lexington, Kentucky

2003

Dedicated to

My parents

Acknowledgments

Although the following dissertation is an individual work, it benefits from the insight and supports of many people. Firstly, I would like to thank my mentor, Dr. Arthur Cammers-Goodwin, for instilling me the desire and qualities to be a good chemist and pushing me to evaluate myself all the time. Thanks for his patience I have improved immensely over the years.

I would like to thank all my committee members: Dr. Anne-Frances Miller, Dr. D. Allan Butterfield, Dr. Stephen Testa and Dr. Lynn Penn for their guidance and valuable advice through my graduate career. Thanks also go to current and former members in the Cammers research group for their support and assistance. I am grateful for being a part of the group. In addition, I would like to thank Dr. Robert Grossman and members of his group for timely and valuable suggestions for my research over the years.

I would like to take the opportunity to acknowledge and thank my collaborators: Dr. John Selegue and Dr. Bailin Chen for their help in flow field-flow fractionation and scanning electron microscopy measurements. And to Dr. Huijian Jiang for her assistance with Inductively coupled plasma analyses. Thanks also go to Dr. Alan Dozier and Dr. Wentao Xu for instrumental assistance on transmission electron microscopy. Their assistance and helpful suggestion really made a difference.

My special thanks go to my parents for their long-time support for my education. I owe everything today to one person, my father Peimin Zhu. His trust and encouragement inspires me to be the person I am today. Thanks, Dad, for

Table of contents

List of tables

List of figures

List of files

YanZhuPHDthesis.pdf   11.9 MB

Chapter 1

Kinetic Precipitation of Solution Phase Mo-POM by Designed Organic Hosts: A Window to Solution Phase Nanostructures

1.1 Overview

The nature of the solution state species in partially reduced aqueous polyoxomolybdates has puzzled scientists for 200 years. Great breakthroughs in this area have only been made in recent years with the discovery of self-assembled giant polyoxomolybdates (Mo-POM), such as the spherical "keplerates".[1,2] Keplerates are supramolecular inorganic clusters with icosahedral symmetry. The spherical keplerate $\{Mo_{132}\}$ is unique due to its discrete nature, size (~2.9 nm, Mo_{132}), charge (-42), and fascinating aesthetic beauty.[1] While the crystal structure has been elucidated, the solution state characteristics are unknown.

Keplerate $\{Mo_{132}\}$ could possibly function as a discrete, nanoscale, multivalent building block for the construction of novel composite materials. The high negative charge that keplerate $\{Mo_{132}\}$ carries could be used to establish strong electrostatic interactions between the organic host and inorganic guest, leading to solid self-assembly processes. Furthermore the keplerate is already at the nanoscale.

Organic chemists seldom study molecules with such huge size (d ≈ 2.9 nm). The theme of the present dissertation is a systematic study for the characterization of solution-phase nanoscopic components in aqueous polyoxomolybdate solutions. The dissertation speaks to the following questions: (1) can we use the keplerate $\{Mo_{132}\}$ as a building block to make structures on the nanoscale? (2) what is the nature of the solution-state species in polyoxomolybdate solutions related to keplerate $\{Mo_{132}\}$? **Figure 1.1** describes the studies that have been done to characterize nanoscopic species in aqueous solution of polyoxomolybdates.
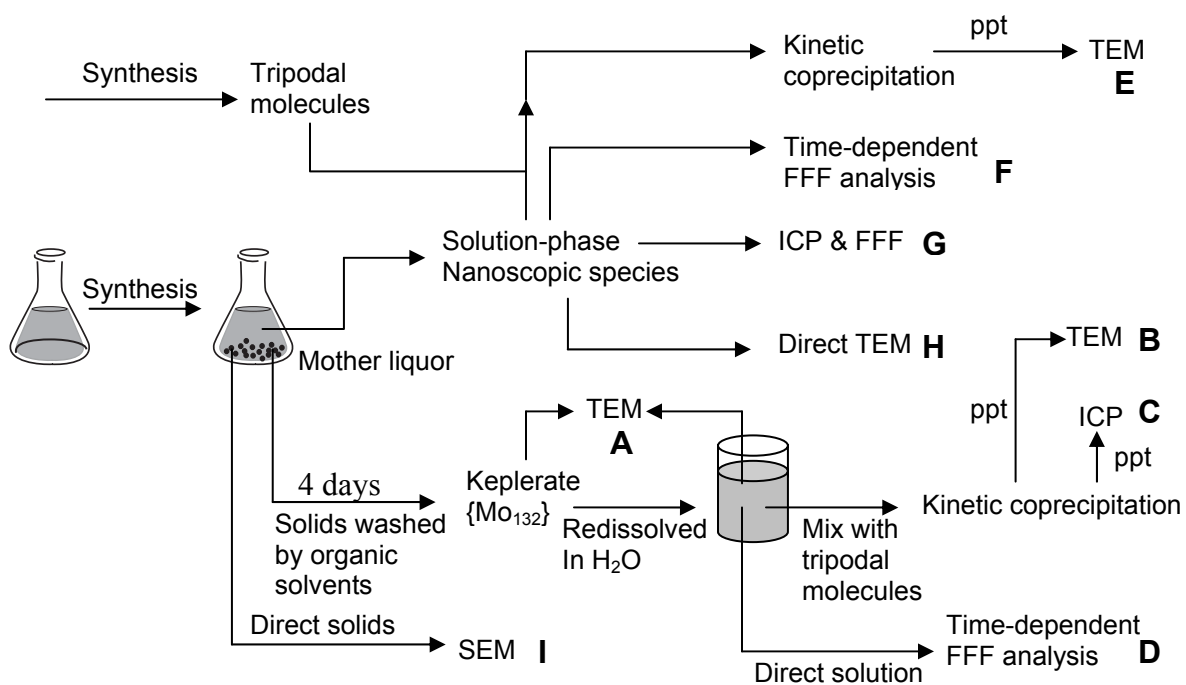
Figure 1.1. Flow chart of the studies for characterization of solution-state nanoscopic species in aqueous polyoxomolybdate.

In **Figure 1.1**, material keplerate $\{Mo_{132}\}$ represents the solids filtered after 4 days from crystallization-driven preparation of keplerate $\{Mo_{132}\}$. Material mother liquor represents the solution-phase of the keplerate $\{Mo_{132}\}$ preparative system (no any attempts to filter solids from the solution).

The dissertation is divided into four chapters. The first chapter, entitled "*Kinetic Precipitation of Solution Phase Polyoxomolybdate by Designed Organic Hosts: A Window to Solution Phase Nanostructures*", develops a protocol for the kinetic precipitation of polyoxomolybdates (Mo-POM) with designed chelating agents **1.1** and **1.2** (**Figure 1.2**) and makes the argument that with tripodal crown ether **1.1** the distributions of particle sizes and the particle morphologies revealed by TEM studies generated repeatable snap shots of dynamic equilibrium of Mo-POM in solution. A similar argument was recently developed for the dynamic conformational behavior of an oligomeric polyelectrolyte. In that study, kinetic entrapment on surfaces followed by atomic force microscopy probed solution phase folding.[3]

To invoke kinetic precipitation, the phase transition from the solution state to the solid state must occur faster than structural changes in the material. From this work and previous studies, the dynamic structure in the solution state of Mo-POM easily satisfies these conditions.[4,5] A hypothetical mode for the interaction between aqueous Mo-POM super structures and tripodal **1.1** or **1.2** is suggested in **Figure 1.2**. In this chapter, we present the evidence for kinetic entrapment of dynamic solution phase Mo-POM with *de novo* organic hosts.
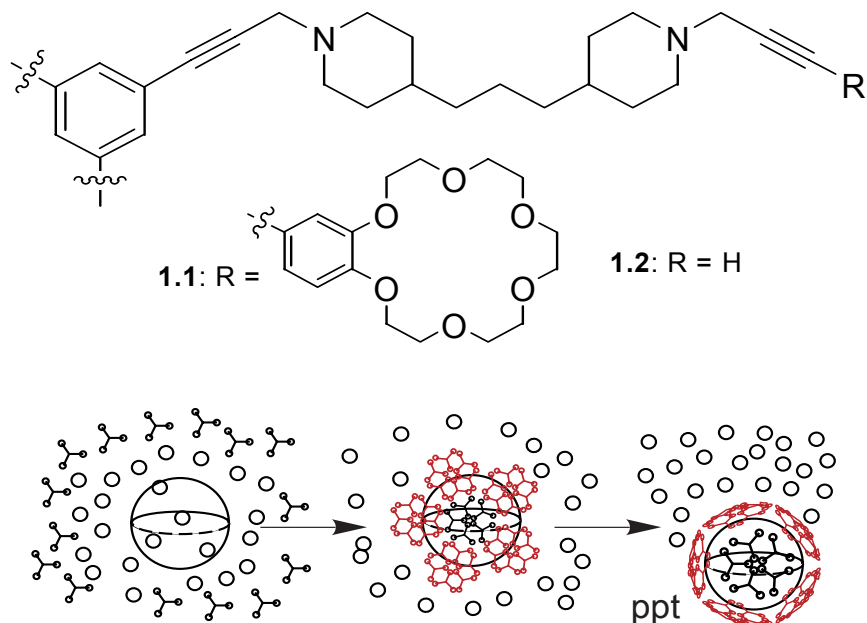
Figure 1.2. (Top) Tripodal molecules used to trap Mo-POM. (Bottom) Schematic representation of kinetic precipitation of Mo-POM. The circles represent solvent; the triangles represent tripodal molecules **1.1**; and the large sphere represents nanoscale Mo-POM aqueous species. Solution state structure is preserved in the solid.

The second chapter, entitled "*Guest-induced Molecular Recognition of Mo-POM*", focuses on kinetic precipitation with a series of structurally analogous hosts and probes the relationship between the structure of the molecular host and the formation of nanostructures. Largely these were failed attempts to perform kinetic precipitation with different designed organic hosts. The third chapter is devoted to "*Dynamic Behavior/Evolution of Nanoscale solution-state species in Partially Reduced Polyoxomolybdate Solution*". An unusual

combination of complementary analytical techniques was used to characterize the time-dependent, partially reduced, aqueous polyoxomolybdate. The dissertation has demonstrated for the first time the feasibility of flow field-flow fractionation (FlFFF) in the separation and characterization of nanoscopic components in partially reduced polyoxomolybdate solutions. Certainly this work is the first time that time-dependent FFF has been applied to the study of any polyoxometallates. The last chapter, entitled "*Conclusion*", summarizes the results obtained from the dissertation work.

1.2 Introduction

Polyoxometallates (POMs), inorganic oligomers that consist of early transition metals bridged by oxide anions, have fascinating molecular properties.[6,7,8] POMs can crystallize into a wide variety of sizes and morphologies.[9] Of these, arguably the most structurally intriguing is polyoxomolybdate (Mo-POM). Early investigations aimed at understanding the nature of partially reduced aqueous solutions of Mo-POM suggested that the solution state probably involved equilibria between nano-mesoscale molecules or perhaps a colloidal mixture of extremely hydrophilic particles.[10-13] Some structural details of molybdenum blue were elucidated by the solid state studies of Müller and associates.[1,14] However, the nature of the solution state species was unknown when this work began. Structural diversity that includes discrete nano-mesoscale scale toroids and spheres arising from the modular construction of molybdate makes these materials unique.[15,16] Further structural diversity at the

nanoscale awaits discovery by efforts aimed at the reduction of symmetry in the super structures.[17] The diverse morphologies reported for Mo-POM solid states invite speculation that media-dependent solution state equilibria might also involve multiple sizes and perhaps non-spherical morphologies. Sorting out which solid state morphologies result from nucleation phenomena and which reflect solution state preferences would be a step closer to understanding the dynamic nature of the Mo-POM solution state and that of related structures.

Molybdenum blue solutions are generally obtained from the reduction of Mo^{VI} species in acid conditions (pH ≤ 3) by various reducing agents. The first composition of these species ($Mo_5O_{14} \cdot nH_2O$) dates back to J. J. Berzelius' work from 1826.[18] Details about the nature of molybdenum blue solutions waited two centuries to be elucidated by Müller and coworkers after they developed a high-electrolyte-concentration strategy to successfully isolate well-ordered crystals from molybdenum blue solutions.[1,14] With recent discoveries of self-assembly strategies for the construction of giant polyoxomolybdates, more derivatives of polyoxomolybdates are available now.[2,19] However, modification of surface chemistry of Mo-POMs, especially through noncovalent-bonded organic components, is still an almost uncharted territory. Developing rational strategies to modify the surface of these Mo-POMs should lead to novel supramolecular structures. Furthermore, the variable nature of the organic components and the inorganic clusters should allow for tunable molecular properties.

1.3 Functionalization of polyoxomolybdates with organic species

To develop a method for kinetic precipitation, modifying the chemical characters of the surface of polyoxomolybdate is necessary because the solubility of polyoxomolybdate depends on good interactions with the hydration shell. Developing rational approaches to modify the surface chemistry of polyoxomolybdate has been a flourishing interest to chemists in recent years. However, most research efforts on the derivation of Mo-POMs relied on the modification of Mo=O functionalities by direct replacement of terminal oxo-ligands with covalently-bonded organic or organometallic groups.[6,20] Most of the examples in the literature performed on the hexamolybdate, $[Mo_6O_{19}]^{2-}$. In this approach, the parent structure was preserved in the structures of derivatives. To date, many synthetic efforts have led to organoimido derivatives of hexamolybdate, but only a few types of reactions have been developed, involving the reactions with phosphinimines, isocyanates, sulfinylamines and aromatic amines.[20,21] Since this approach is not the focus in current work, for more detailed discussion, the reader is referred to reviews in the chemical literature.[20,21,22]

Due to the low density of surface charge, the terminal Mo=O bonds on Mo-POM are generally unreactive. Thus aforementioned modifications of the Mo-POM are often difficult, requiring harsh reaction conditions and prolonged reaction time. An alternative technique has been developed recently based on a self-assembling protocol.[23] The strategy uses cationic surfactants to replace the cations associated with the anionic Mo-POM to form discrete supramolecular

assemblies, the so-called "surfactant-encapsulated clusters" (SECs) by the authors.[23] To apply this technique, a water-immiscible organic solvent of cationic surfactant was added drop-wise to an aqueous solution of keplerate $\{Mo_{132}\}$ until the phase transition was complete (color disappearance in aqueous phase).[23] The authors found that the phase transition of keplerate anions from aqueous phase to organic phase was only achieved with DODA (dimethyldioctadecyl ammomium) surfactant among the surfactants tested so far, presumably due to the complementary geometrical requirements between the organic species and the inorganic cluster. The characteristic feature of these novel SECs was their remarkable inclusion geometry. The structures of these isolated clusters were such that all DODA molecules organized around the central keplerate anionic surface in a monolayer, resulting in a remarkably spherical core-shell supramolecular ensemble.[23] Such novel material combined the properties of the inorganic clusters with the advantages of the organic species, such as tunability and bio-compatibility, promising potential technical applications.

Upon comparing both synthetic strategies, the way of making SECs definitely has its own advantages over direct substitution of Mo-POM. Although the driving force for the SEC process is still unknown, it presumably reflects synergy between electrostatic interactions and hydrophobic interactions.

1.4 The approach for molecular recognition of Mo-POM

1.4.1 Design principles for organic hosts

Optimum encapsulation might allow solution state structures of polyoxomolybdate to be preserved in the solid state. Human endeavors in the design of supramolecular architecture benefit from versatility and simplicity when multi-partite, molecular hosts possess three-fold symmetric components.[24] The designer molecular hosts in the current work for Mo-POM incorporated design principles intrinsic to structural problems encountered when three dimensional enclosures are created from two dimensional polygons. There are only a limited number of ways in which identical regular polygons may be adjoined at the edges and vertices to form three-dimensional enclosures. Equilateral triangles may be joined in three ways while squares and pentagons may be joined in only a single manner to make symmetric three-dimensional polygons. Moreover, joining the edges of uniform two-dimensional shapes that have six or more sides can not produce enclosures because the sum of the angles around each vertex would be equal to or greater than 360°. These principles give rise to the five 'perfect' platonic solids: tetrahedron, cube, octahedron, dodecahedron and icosahedron.
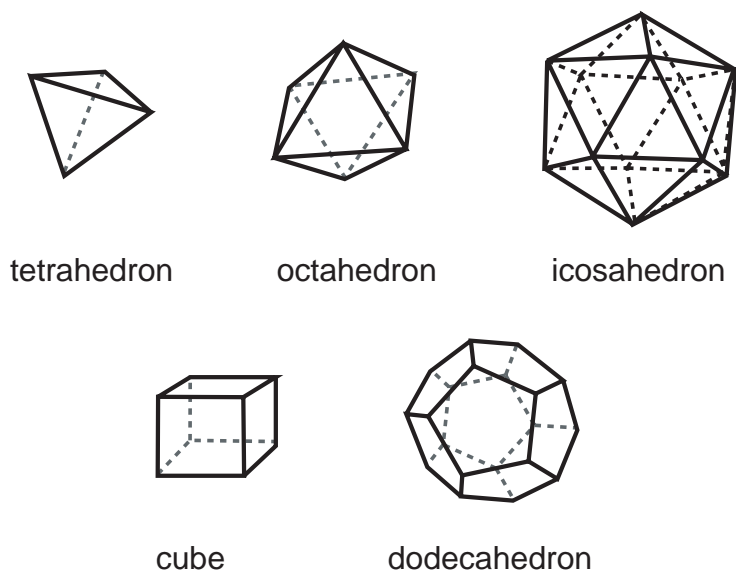
Figure 1.3. The five platonic solids.

On the molecular level, C_3 symmetric subunits are the most efficient building blocks for the construction of high-symmetry superstructures because molecular instructions for edgewise self-assembly are present in triplicate in the equilateral triangle motif whereas structures composed of squares or pentagons incorporate instructions for edgewise self–assembly four times and five times respectively in the same molecules.[24] Thus C_3 components, as a starting point of self-assembly, minimize synthetic efforts.

1.4.2 Selection of Mo-POM guest

The nature of solution state species in partially reduced aqueous polyoxomolybdate has fascinated chemists for more than two centuries. Great breakthroughs have only been made in recent years with the discovery of self-assembling giant polyoxomolybdates (Mo-POM), such as "giant wheels"[25] and

"keplerates"[1,2, 26]. The spherical "keplerate" Mo-POMs have unique values among the Mo-POMs discovered so far, owing to their sizes, structural complexity and striking aesthetic beauty.[2] **Figure 1.4** shows the crystal structure of keplerate $\{Mo_{132}\}$ and its pentagonal building blocks $\{(Mo)Mo_5\}$.
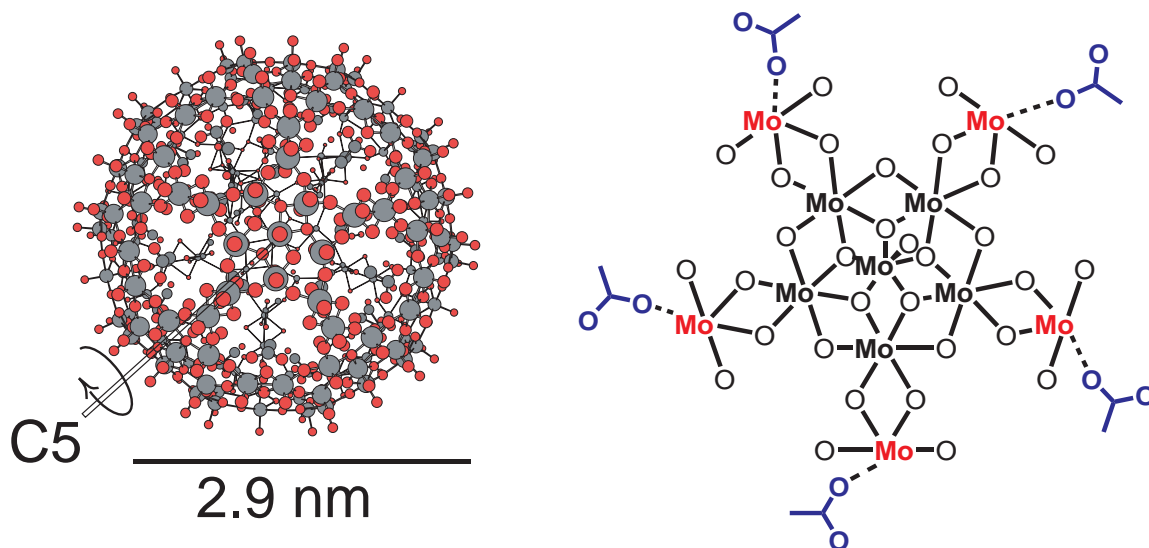
Figure 1.4. Crystal Structure of keplerate $\{Mo_{132}\}$ giant molecule (left) and the corresponding pentagonal building blocks $\{(Mo)Mo_5\}$ (right). The structure was constructed from crystal data of depository number: CSD-410097. The center of the structure is the locus of one of the C_5 axes of symmetry. In the pentagonal building block (right), the Mo atoms in black are oxidation state VI and the Mo atoms in red are oxidation state V. The pentagonal building block occurs at the center of the C_5 axis in the keplerate.

All the keplerates are made from the basic $(pentagon)_{12}(linker)_{30}$ structure. The pentagonal building block $\{(Mo)Mo_5\}$ is constructed with a central

MoO$_6$(OH$_2$) bipyramid sharing edges with five MoO$_6$ octahedra. In the case of keplerate {Mo$_{132}$}, the {Mo$^V_2$O$_4$}CH$_3$CO$_2$ units are the linkers that connect the twelve pentagonal building blocks in an icosahedral super structure (**Figure 1.4**). Our interests in modification of Mo-POMs through non-covalent bonded organic segments aimed at keplerate {Mo$_{132}$}, for the following reasons: 1) Keplerate {Mo$_{132}$} is large, very symmetric, discrete structure that is already at the nanoscale. It could possibly be used in the construction of supramolecular assemblies. 2) The high negative charge that keplerate {Mo$_{132}$} carries could be used to establish strong electrostatic interactions between the organic host and inorganic guest, leading to solid self-assembly processes.

Ideal molecular hosts for encapsulation of Mo-POM should control the molecular structure of the anionic guest, its surface chemical properties and perhaps bioavailability. With these goals in mind, molecular hosts were designed that might selectively stabilize Mo-POM polyanions in an aqueous medium. In a demonstration of principle, an icosahedral virus devoid of nucleic acids has been used to encapsulate polyoxometalates and control nucleation.[27] Furthermore, electrostatic interactions between keplerate-like forms of Mo-POM and positively charged surfactant molecules resulted in crystalline keplerate surrounded by surfactant.[23]

Tripodal **1.1** and **1.2** have the potential to assemble spherical enclosures around keplerate-like structures in a manner analogous to the construction of the platonic solids by joining the edges and the vertices of equilateral triangles. Differences in the interactions of **1.2** and Mo-POM from those of **1.1** and Mo-

POM were used to unveil the effect of the crown ether. The solubility of Mo-POM decreases with increasing ionic strength, presumably due to destruction of the hydration shell.[28] Likewise, electrostatic interactions between the tripodal chelating agents and Mo-POM should have cooperatively destroyed the hydration shell and lead to an insoluble Mo-POM complex. The amine functionalities in **1.1** and **1.2** protonate below pH 7. Likewise crown ethers associate with H_3O^+, NH_4^+ or K^+ and thereby can take on positive charges. In the molecular recognition of Mo-POM**,** the crown in **1.1** probably forms chelates with NH_4^+, the Mo-POM counter ion. The amines and the crown ethers in **1.1** are expected to perturb the POM species less than the ammonium cation due to increased steric parameter of the tertiary amine compared to ammonia. In any surface-bound state, the positively charged benzocrown ethers in **1.1** would have to be proximal. Precedent exists for cation-associated crown ether moieties interacting favorably in the solid state.[29]

1.5 Results and discussion

Early investigations for the nature of partially reduced aqueous solutions of Mo-POM aimed at Mo-POM solid states; the nature of solution state is still not well-understood. Müller and coworkers observed the formation of mono-distributed aggregates with a hydrodynamic radius of 40 nm (from dynamic light scattering (DLS) technique) by dissolving Mo-POM crystals in some organic solvents.[4] More specially, the colloidal mixture aggregated into even larger structures upon evaporation of the solvent.[4] Although weight-average, size-

average and multi-modal distribution of particle sizes are available from DLS techniques, the large extinction coefficient of the keplerate {Mo$_{132}$} (ε = 1.85 X 10^5 M^{-1}cm^{-1}) and related structures in molybdenum blue hinder DLS sizing of Mo-POM particles. Enough data is available to conclude that Mo-POM in water is more disperse than Mo-POM in other solvent systems. DLS techniques gave good results with the relatively transparent, aqueous Fe-Mo-POM, of which the {Fe$_{30}$Mo$_{72}$} is the smallest discrete structure with a closed surface characterized thus far. The DLS studies indicated two size regimes in solution and implied vesicular instead of aggregate structures for the Fe-Mo-POM aqueous state.[5,30] SEM (scanning) and TEM (transmission) techniques have also been applied to Mo-POMs derived from molybdenum blue.[4,31,32] As a whole, these previous studies suggest that media-dependent, solution state equilibria involve multiple sizes, perhaps non-spherical morphologies and aggregation into larger structures instead of maintenance of status as single anions in Mo-POM solutions.

In current work, on the basis of TEM investigations, we present evidence for the kinetic precipitation of Mo-POM with designed chelating agents **1.1** and **1.2**. Coprecipitates **ppt1.1** and **ppt1.2** were very insoluble; titration of Mo-POM$_{(aq)}$ with excess **1.1** or **1.2** left little Mo-POM in solution detectable by UV at 455 nm. Tripodal **1.1** in 0.1 M KCl became soluble below pH 5 as determined by simultaneously decreasing pH and monitoring the UV absorbance of the liquid at 290 nm. A titration monitored at 455 nm showed that Mo-POM, 4.0 X 10^{-9} M, irreversibly decomposed above pH 6. This result was expected because synthesis of Mo-POM required low pH and high polyoxomolybdate concentration

and Mo-O should form reversibly under aqueous conditions. In contrast, coprecipitate **ppt1.1** and **ppt1.2** did not dissolve after agitation in water from pH 1-11 at room temperature.

1.5.1. The morphology of keplerate {Mo_{132}}

To obtain more information about the nature of the keplerate {Mo_{132}}, we examined solid material derived from keplerate {Mo_{132}} with transmission electron microscopy (TEM). **Figure 1.5A** shows the micrographs of keplerate {Mo_{132}} samples obtained by directly depositing the powders into the lacey carbon copper grid. Polydisperse size distributions of near-spherical particles were observed with radii of 25-40 nm, which were apparently much larger than single keplerate molecules (d ≈ 2.9 nm). This study confirmed the speculation that medium-dependent solution state equilibrium probably involved multiple sizes and perhaps non-spherical morphologies. However, the nature of these nanoscopic species remained unclear. The nanostructures could be solid or hollow or perhaps the morphology of the particles in the solid state might not reflect the actual morphology of the solution state. The formation of large features was probably the result of self-assembly of single keplerate molecules. The loss of solvent from within the structures could have explained the instability and the difficulty in imaging this material. When the crystalline keplerate was dissolved in water, the TEM graphs of the solution state were devoid of features with radii greater than 3 nm (**Figure 1.5B**). Thus, individual keplerate {Mo_{132}} species probably merged with the granularity of the micrographs. Therefore, it is

much easier to image the larger, less popular species on which this study focused. Furthermore, at high magnification (10^6 X), a clear crystalline lattice was presented in solution state sample.
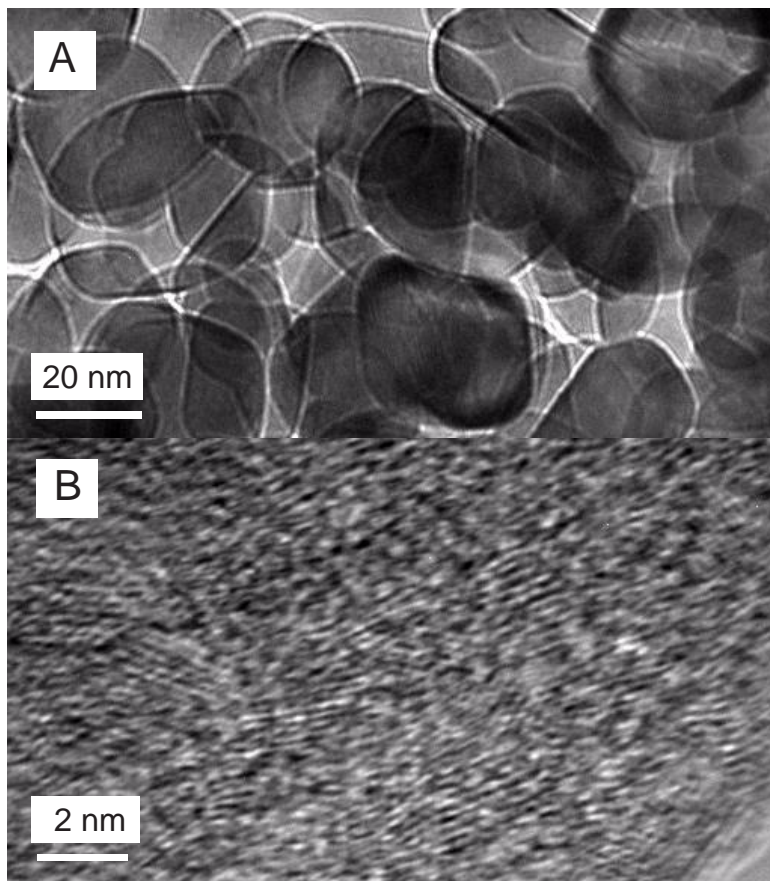
Figure 1.5. (**A**): HR-TEM micrograph of keplerate {Mo_{132}} solid (directly deposited powders on the copper grid). (**B**): HR-TEM micrograph of solidified keplerate {Mo_{132}} species from dilute aqueous solution (3 mg crystalline material dissolved in 2 ml deionized water). Step **A** in page 2: **Figure 1.1**.

1.5.2 Kinetic trapping of solution phase Mo-POM by tripodal molecule 1.1

TEM analysis repeatedly revealed nanoscopic spherical features in **ppt1.1** whereas micrographs of **ppt1.2** were repeatably devoid of features with radii

greater than 4 nm (compare **Figures 1.6A** and **1.6B**). Hypothetically, **1.1** and **1.2** kinetically trapped polydisperse Mo-POM before any structural deviations from the solution state occurred. However, composite material **ppt1.1** was stable enough to image under the high vacuum conditions of the sample preparation and analysis (4.0×10^{-7} torr), whereas **ppt1.2** decomposed. This hypothesis has the nanostructure in **ppt1.1** dependent solely on native structure in Mo-POM and not dependent on synergism between **1.1** and Mo-POM. Matching previous SAXS particle sizing experiments[4] to the current data and the fact that structure in material derived from Mo-POM alone was less stable than **ppt1.1** supported the kinetic precipitation of solution state Mo-POM by **1.1**. Definitive evidence for kinetic precipitation is presented in section **1.5.3** in which TEM morphologies of **ppt1.1** from the preparative mother liquor are compared to TEM morphologies of **ppt1.1** from the dissolution of keplerate {Mo$_{132}$} and coprecipitation of Mo-POM.

Ppt1.1 formed within seconds whereas the super-sized structures of aqueous state Mo-POM require two to three days to evolve. When a chemically related Mo-POM is prepared fresh, small angle X-ray scattering (SAXS) does not detect particles in the solution phase with radii greater than 5 nm. After the material is allowed to stand for two days, rerunning the SAXS analysis results in the evolution of particles with sizes in the r~20 nm range.[4] A parameter that would have made kinetic precipitation of Mo-POM impossible would have been a fast chemical process that would have removed large Mo-POM particles from the distribution. The slow forward rate process for the evolution of nanostructured species implicated by the SAXS study guarantees an even slower reverse

17

process for the decomposition of the nanoscopic species. Slow assembly of Fe-Mo-POM has also been recently reported by Liu.[5]
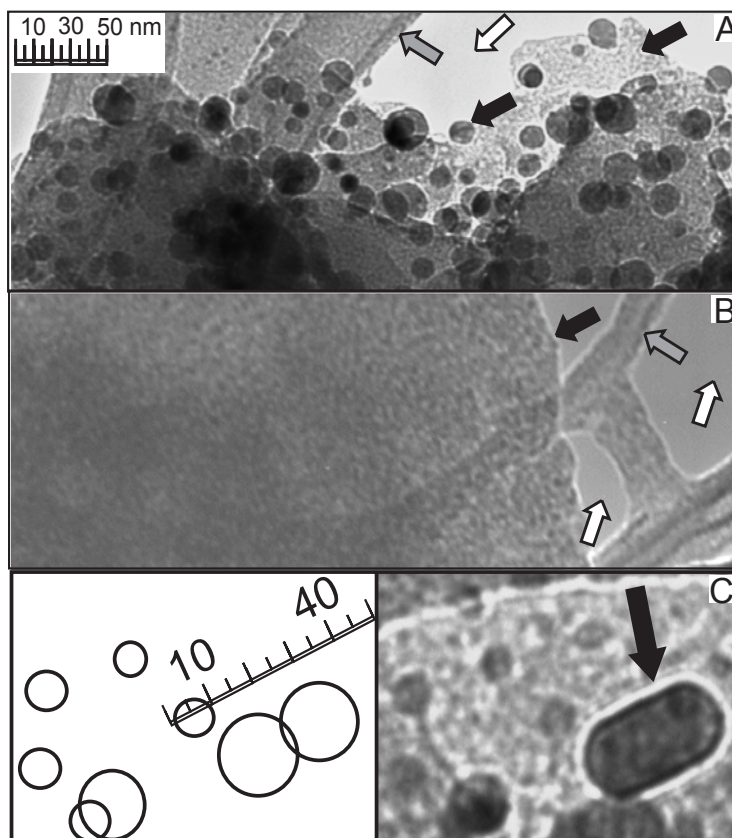
Figure 1.6. Micrographs (JEOL 2000FX, TEM) of **ppt1.1** (**A**) and **ppt1.2** (**B**) formed upon quick addition of **1.1** and **1.2** respectively to Mo-POM in a 20: 1 ratio (Step **B** in page 2: **Figure 1.1**). Analysis of the solid confirmed the 20: 1 ratio of **1.1** (C, H, N elemental analysis) to total Mo by inductively coupled plasma atomic emission based on keplerate $\{Mo_{132}\}$ (Step **C** in page 2: **Figure 1.1**). Micrographs **A** and **B** have identical scale and magnification. Solids **ppt1.1** and **ppt1.2** were similar in appearance. Preparations of the solids for TEM were identical. Grey and white arrows indicate the lacey carbon substrate and voids respectively. The black arrows indicate material that contained Mo by energy dispersive x-ray spectroscopy. Ellipsoidal features were also located in the micrograph (**C**). These were assumed to be transition materials between larger and smaller structures.

Observed structural instability in the materials supported kinetic precipitation of **ppt1.1**. The large features in **ppt1.1** merged over the course of 3-4 weeks into larger features until continua, featureless by TEM, were reached. The new material resembled the Mo-containing material in **Figure 1.6B** (black arrow). In a few micrographs, the restructuring of the spherical features might have been caught on camera. **Figure 1.6C** shows a micrograph containing a rare elliptical feature that is approximately twice as long as it is wide (33 x 17 nm). Anisotropic features should have been kinetically unstable because **ppt1.1** should have sought a spherical shape to minimize the surface area to volume ratio. With less information and a lower-resolution microscope, this hypothesis for the observation of asymmetric transition structures of Mo-POM was offered sixty years ago.[31] Furthermore a 20: 1 ratio of **1.1**: Mo-POM (based on keplerate $\{Mo_{132}\}$) produced the large spherical features in micrograph **1.6A** whereas a 5: 1 ratio gave rise to featureless micrographs like the one in **1.6B**. High stoichiometric ratios of **1.1** to Mo-POM[†] should have kinetically and thermodynamically favored the mechanism outlined in **Figure 1.2**.

Observation of nanostructures in the Mo-POM particles in the absence of **1.1** linked the observations of nanostructures and elliptical transition structures in **ppt1.1** to Mo-POM and not to synergy between Mo-POM and **1.1**. While structural differences between samples of **ppt1.1** and Mo-POM were obvious from differences in the TEM images, differences in elemental content were also apparent upon examination of the energy dispersive X-ray spectra (EDS). Material can absorb high-energy electrons and releases the energy by the

emission of X-rays with energies and intensities semi-quantitatively characteristic of elemental composition.[33,34] **Figure 1.7** displays two representative EDS spectra of keplerate $\{Mo_{132}\}$ (top) and **ppt1.1** (bottom). The relative amount of Mo versus lighter elements was lower in keplerate Mo-POM than in **ppt1.1**. Also much potassium, presumably sequestered from solution by the benzocrown moiety in **1.1**, was detected in **ppt1.1** but not in keplerate Mo-POM.
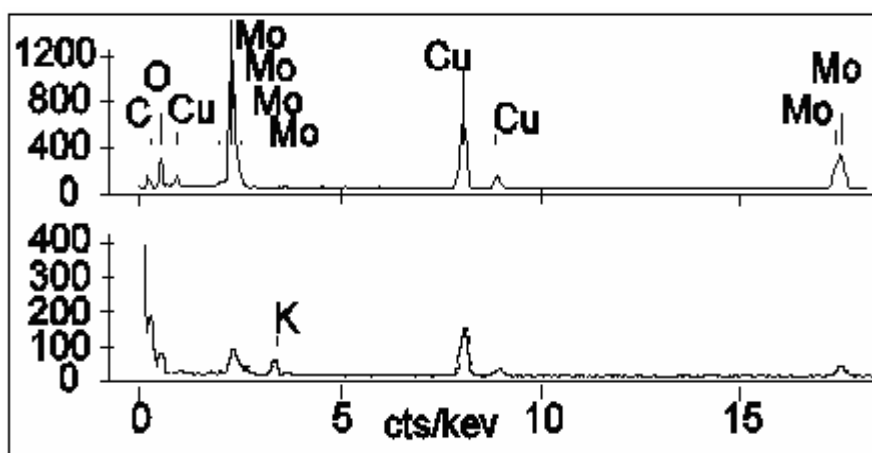
Figure 1.7. Energy dispersive spectral differences between keplerate Mo-POM (top) and **ppt1.1** (bottom). The lacey carbon Cu grid produced the Cu peaks.

Figure 1.8 shows two more samples of **ppt1.1** in addition to **Figure 1.6A** and **C**. The micrographs were used to produce particle size distributions by measuring and counting the particles in the field with the aid of image processing software. Examples of the counting/ measuring process are shown in **Figure 1.6C** and **1.8A** in which boundaries were drawn around the features. In the image analysis process ellipses were mathematically fitted to the closed curves and evaluated statistically in terms of size, and circularity.
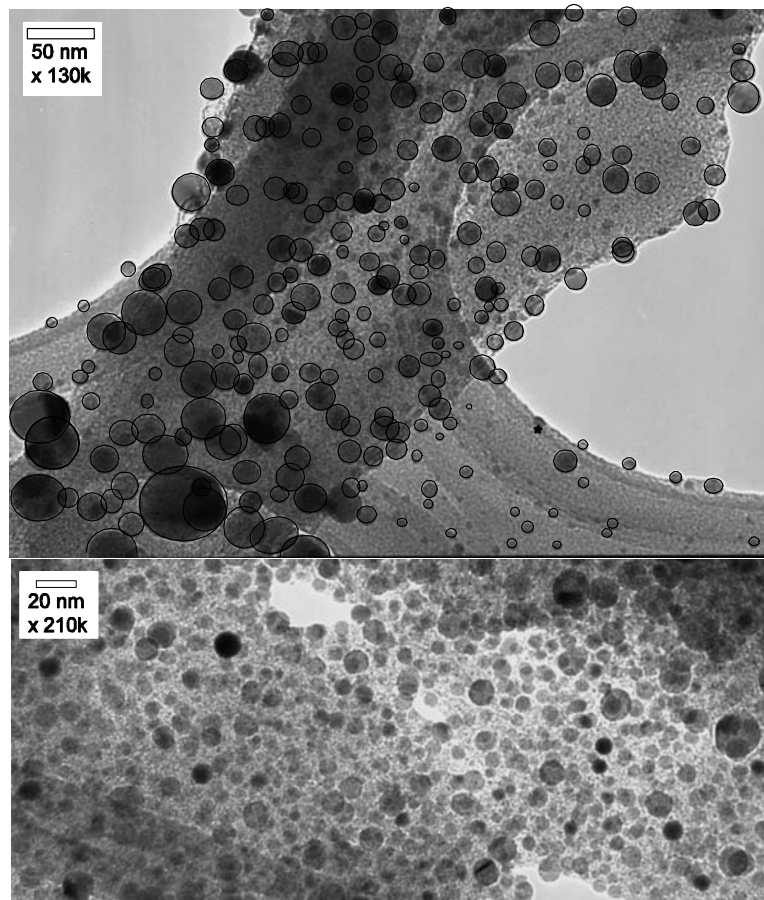
Figure 1.8A (upper) and **1.8B** (lower). Two more samples of **ppt1.1** other than **Figure 1.6A** and **C** (Step **B** in page 2: **Figure 1.1**). Circles for measurement are drawn around features in **1.8A**.

Quantitatively, the ratio of anisotropic to spherical structures was higher in solid keplerate Mo-POM than in **ppt1.1**. **Figure 1.9A** is a distribution of particle morphologies by the index function: asymmetry = (major axis–minor axis)/(average width) which is the deviation from circularity of the feature normalized by its average size. When the index is zero, the feature is a perfect circle. At 0.2, the two axes of the ellipse differ by 18% and at 0.6 the major is

twice as long as the minor axis. The nanostructures in the micrographs of keplerate Mo-POM in the absence of tripodal molecules were not as circular as those of **ppt1.1**, presumably due to their decreased stability compared to **ppt1.1**. Asymmetry in these structures was most probably the result of loss of internal solvent molecules.
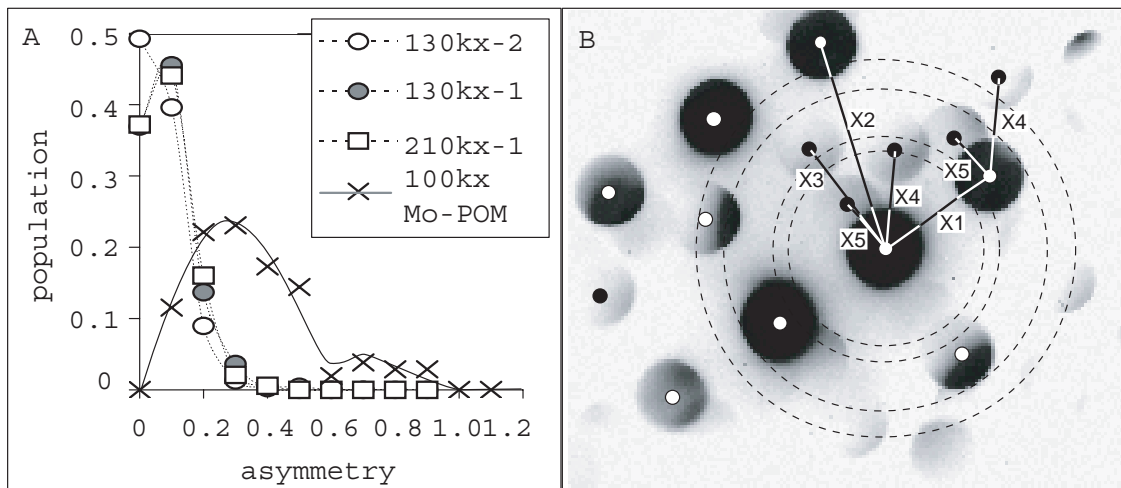
Figure 1.9. A: plots the number of particles as a function of a unitless asymmetry index. One lot is analyzed at magnification 130 and 210K. **B:** is a spot diffraction pattern of a feature in **Figure 1.6A** that indicated that the Mo-atom lattice was intact in the superstructure. The superimposed dashed lines are a diffraction pattern produced by a gold calibration standard to determine the camera constant of the TEM. Segments X1-X5 correspond to layers spacing 1.8, 1.1, 1.7, 2.2 and 4.1 ± 0.4 Å respectively.

The features in the micrographs of **ppt1.1** produced ordered spot diffraction patterns, signaling a microcrystalline lattice in these objects. The diffraction pattern shown in **Figure 1.9B** had Bragg lattice spacing 1.1, ~1.8, 2.2

and 4.2 Å. These distances are too small to indicate nanostructure. Most of the spacings in the spot diffraction in **1.9B** were likely produced from high-Miller index phenomena, through the Mo-lattice edges of one or more nanoscopic species. The lattice spacing of 4.2 ± 0.4 Å matched Mo-Mo distances in the X-ray structure of keplerate $\{Mo_{132}\}$, ~3.8 Å.[35]
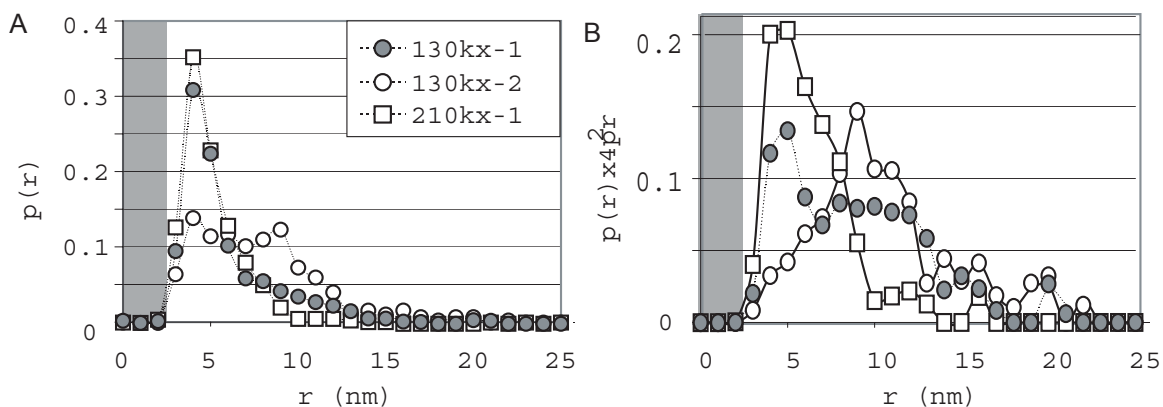
Figure 1.10. A represents lot-dependent, and magnification-independent distributions of particle sizes. **B** converts the data in **A** to mass distributions. The shaded line at left is the TEM resolution limit for particle selection and measurement. These graphs are not equilibrium distributions.

Figure 1.10A indicates that the TEM-derived particle size distributions were skewed toward the size the smallest discrete closed structures, the keplerate. The resolution of these electron micrographs is ~2-3 nm, approximately the diameter of keplerate $\{Mo_{132}\}$. Analyses of two samples of **ppt1.1** at magnification 130k and 210k showed sample-dependent size distributions of Mo-POM. The technique used to prepare **ppt1.1** should not have

resulted in the trapping of equilibrium distributions of particle sizes. Crystalline Mo-POM solid was dissolved in aqueous media at low dilution and then precipitated by **1.1** to produce **ppt1.1** immediately. The sizing depended minimally on magnification. At higher magnification smaller particles, if present, can be identified. Particles derived solely from solid keplerate Mo-POM were larger.

Compare average particles sizes in **ppt1.1** of the three graphs in **Figure 1.10A**, r = 7 ± 3, 8 ± 4, and 5 ± 2 nm to the average sizes of two lots of the Mo-POM material, r = 22 ± 11 and 32 ± 7 nm, particles derived solely from solid keplerate Mo-POM were larger. Due to the ephemeral nature of the Mo-POM sample under the conditions of TEM preparation and analysis, the large structures found in the Mo-POM solid should not necessarily characterize the equilibrium Mo-POM solution state from which they were derived.

Most experimental results scale with the mass distribution of the material instead of the number distribution of particles. For example, larger particles scatter light more efficiently, skewing the measurement toward larger values. An argument is presented for hollow Mo-POM structures in the following paragraph. Therefore, conversion of a size distribution to mass distribution should employ the formula for the surface area of a sphere. The ith population element in the distribution is expressed as: $P(r)_i = n_i/N \cdot 4\pi r^2$. The mass distribution, thus derived, is shown in **1.10B**. The noise in the heavy region of the mass distribution is understandable when one considers that one heavy particle out of hundreds raised the graph off the zero line.

The features in all the micrographs above were hollow by the following argument. In general the optical densities of micrographic features scale with the atomic weight and the number of atoms encountered by the electron beam. Heavier and more numerous atoms scatter more electrons which gives rise to darker images. **Figure 1.11** indicates that doubling the mass through which the electron beam passed detectably changed the optical density of the image. However, the optical densities of the features versus the radii of the features were essentially constant.
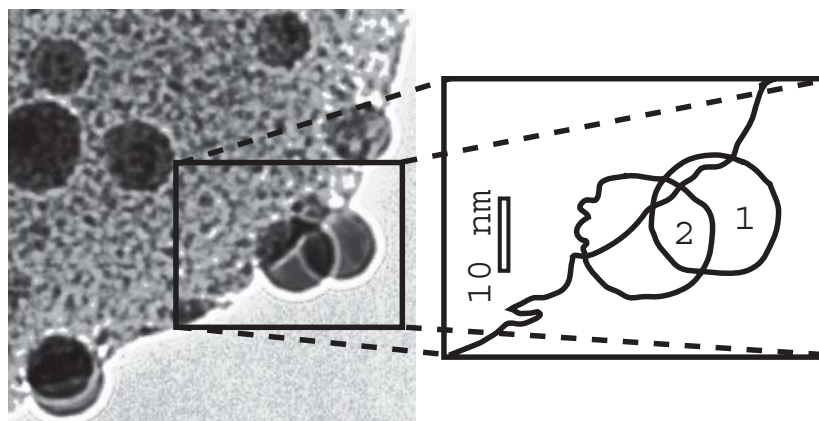
Figure 1.11. The morphology of the Mo-POM and **ppt1.1** spheres (**Figure 1.6A**) is smooth when not set against the granular Mo-containing background. Imaged electrons scatter through one sphere in region 1 and two spheres in region 2. The grey scale value of region 1 is 13 versus 48 for region 2 (0 = black, 255 = white).

Objects possessing radii from 3 to 30 nm were detected. If the features were structurally homologous from surface to core, this range corresponds to a 1000 fold increase in mass through which the electron beam would pass. Optical

densities independent of mass can only be met if the features in the TEM were either hollow or flat. However, surface to volume forces do not drive two dimensional structures toward circularity, therefore spherical structures with Mo at the surface is the best interpretation of the data. Less symmetric Mo-POM species in **Figure 1.5** might have deformed as a result of loss of internal solvent molecules under the TEM vacuum. Hollow structures are in accordance with Liu's light scattering studies of the Fe-Mo-POM.[3,30]

1.5.3 TEM study of ppt1.1 from mother liquor: unambiguous kinetic precipitation

A precipitate, **ppt1.1'**, formed immediately when the mother liquor of the synthetic protocol of keplerate $\{Mo_{132}\}$ (about 700 µL) was mixed with an aqueous solution of tripodal compound **1.1** (pH~3). The TEM analysis showed that the mother liquor of the preparation of the keplerate $\{Mo_{132}\}$ after four days revealed large species (r=20-30 nm) in the coprecipitate. The nanoscopic species derived from the mother liquor of the preparation (**Figure 1.12**) were unambiguously larger than those derived from the redissolved keplerate material; therefore, the time scale of coprecipitation is shorter than the solution-phase rearrangement and shorter than the evolution of nanoscopic species. This strongly confirms the hypothesis of kinetic precipitation.

The size distributions of the nanoscopic features in **Figure 1.12** (r~25 nm) were probably representative of a solution phase near equilibrium conditions. The nanoscopic features in the micrographs of **ppt1.1'** produced ordered spot

diffraction patterns (the inserted figure in **Figure 1.12** upper right), indicating a microcrystalline lattice in these objects.
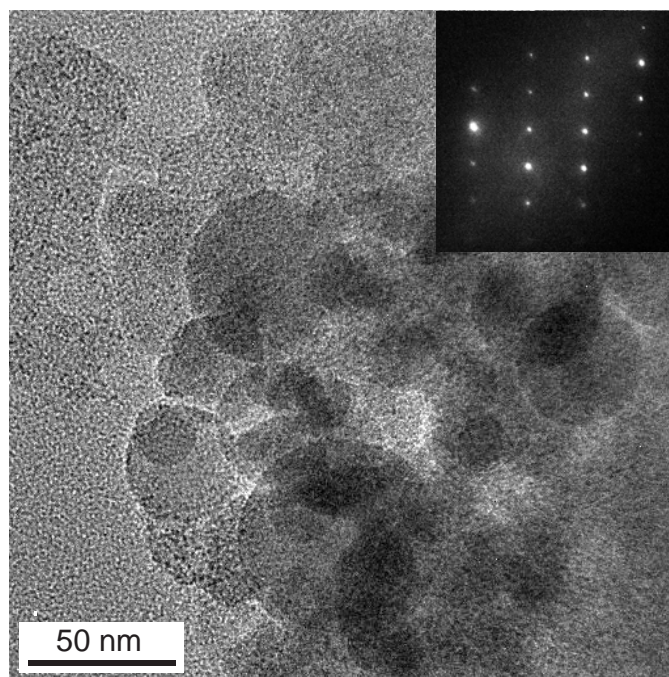
Figure 1.12. TEM analysis of nanoscopic species in **ppt1.1'** (Step **E** in page 2: **Figure 1.1**). The inserted figure is a spot diffraction pattern of a feature in the image.

1.6 Synthesis

One of the most straightforward synthetic methodologies to connect terminal alkynes and aryl groups is the palladium(0)/CuI catalyzed coupling, first reported by Sonogashira and co-workers.[36] The synthesis of key intermediate, **1.2**, proceeded smoothly. Treatment of commercially available 4,4'-trimethylenedipiperidine **1.3** with propargyl bromide and Et_3N in THF afforded compound **1.4** (N,N'-dipropargyl-4,4'-trimethylenedipiperidine). Compound **1.4** is a *bis*-alkyne, S_N2 substitution of *bis*-alkynes was best done with the sp terminus

capped with a surrogate proton. The TBDMS group served this purpose very well. Consequently, employing the typical Sonogashira reaction conditions for the coupling of mono-TBDMS-protected alkyne **1.5** and 1,3,5-tribromobenzene furnished **1.6**. Subsequent deprotection of the TBDMS group resulted in the intermediate **1.2** (**Figure 1.13**). However, it was found that further connections on the way to tripodal compound **1.1** required significant modifications of Sonogashira-based protocols.
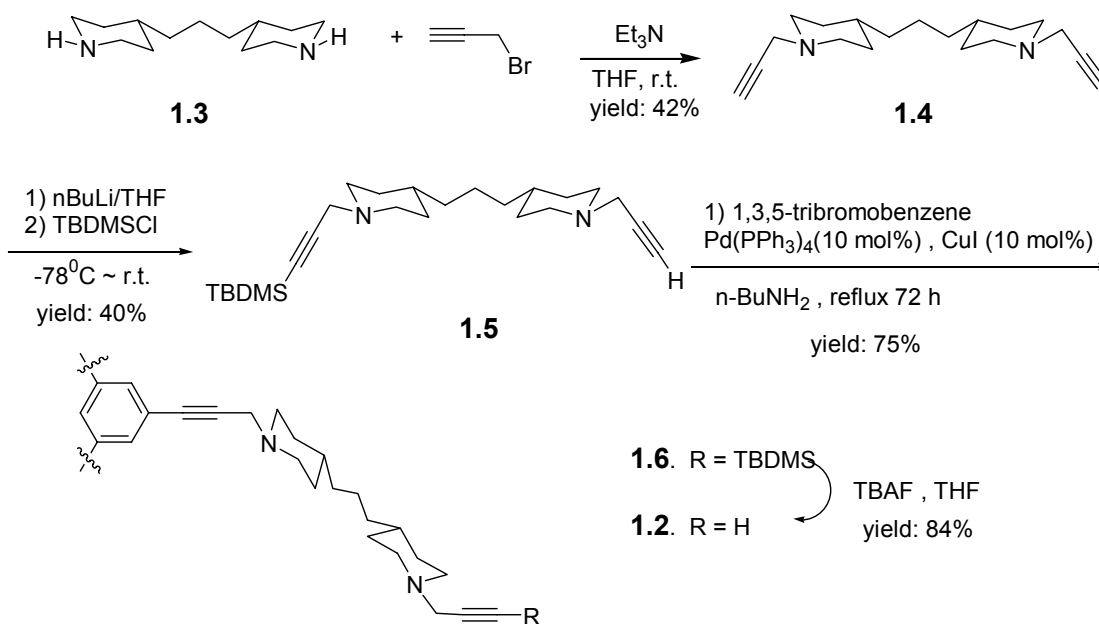
Figure 1.13. Synthetic scheme of tripodal molecule **1.2**.

Initially commercially available 4'-bromobenzo-18-crown-6, a very electron-rich and unreactive aryl bromide, was chosen as the substrate. Only one example of Sonogashira reaction of this substrate was reported previously.[37] The published reaction conditions (Pd(OAc)$_2$/CuI and piperidine as solvent) used in the case of **1.1** produced no *tris*-acetylenic product (entry 1, **Table 1.1**).

Subsequent attempts at typical Sonogashira reaction conditions, Pd/CuI in conjunction with amines as solvent or cosolvent and heating to ~80 °C (entry 2~5, **Table 1.1**), also proved inefficient. Furthermore, the elevated temperatures resulted in undesired products. Obviously, milder reaction conditions, such as room temperature reactivity, were highly desirable in the case of **1.1**.

Table 1.1. Optimization of Sonogashira Couplings of **1.2** with 4'-bromobenzo-18-crown-6.
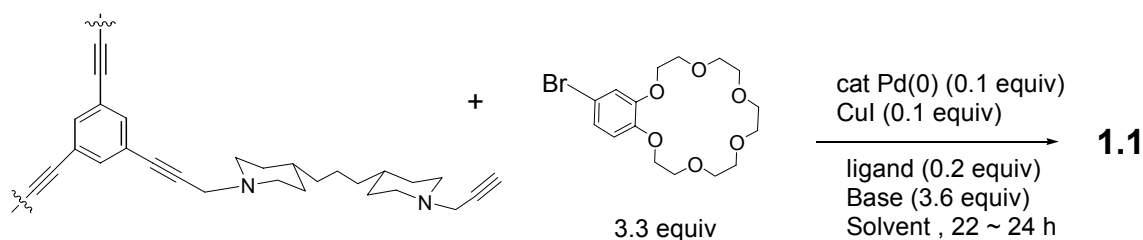
entry	Pd reagent	ligand	base	solvent	T (^{0}C)	Yield of 1.1(%)
1	Pd(OAc)$_2$	PPh$_3$	piperidine	piperidine	80	< 2
2	Pd(PPh$_3$)$_2$Cl$_2$	N/A	piperidine	piperidine	80	0
3	Pd(PPh$_3$)$_2$Cl$_2$	N/A	Et$_2$NH	Et$_2$NH	80	0
4	Pd(PPh$_3$)$_2$Cl$_2$	N/A	n-BuNH$_2$	n-BuNH$_2$	80	0
5	Pd(PPh$_3$)$_2$Cl$_2$	N/A	HN(i-Pr)$_2$	HN(i-Pr)$_2$	80	0
6	Pd$_2$(dba)$_3$	PPh$_3$	piperidine	DMF	r.t.	< 2
7	Pd(PhCN)$_2$Cl$_2$	TFP	piperidine	THF	r.t.	< 2
8	Pd(PhCN)$_2$Cl$_2$	P(t-Bu)$_3$	piperidine	THF	r.t.	< 2
9	Pd$_2$(dba)$_3$	TFP	piperidine	DMF	r.t.	< 2
10	Pd$_2$(dba)$_3$	P(t-Bu)$_3$	piperidine	DMF	r.t.	< 2

Several groups have demonstrated the successful applications of Pd(PhCN)$_2$Cl$_2$ catalyst system in the Sonogashira reactions.[38,39] In addition, Pd$_2$(dba)$_3$ as a palladium source in conjunction with phosphine ligands served as
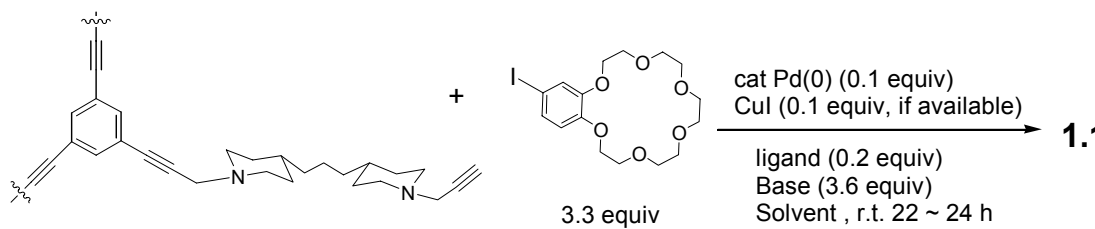
an efficient and versatile catalyst for Sonogashira coupling reactions.[40,41,42] Applications of phosphine ligands other than PPh$_3$ have been used successfully in the Sonogashira-type reactions and apparently activated the couplings. Fu and co-workers have demonstrated that Pd catalysts in conjunction with the bulky and electron-rich P(t-Bu)$_3$ functioned as an efficient catalyst for Sonogashira reactions of aryl bromides at room temperature.[38] Herrmann *et al* also observed that Pd$_2$(dba)$_3$/P(t-Bu)$_3$ catalyst system promoted room-temperature Sonogashira couplings of aryl bromides even in the absence of CuI.[42] Other groups have observed that the use of tri-2-furyl phosphine (TFP) produced dramatically enhanced reactivity in Sonogashira-type coupling reactions.[39,43,44] The enhanced reactivity was presumably attributed to the low electron donating ability of TFP ligand.[45]

To optimize the coupling conditions for the synthesis of tripodal crown ether **1.1**, a systematic study of the coupling reactions with various combinations of Pd catalysts and phosphine ligands was done. However, in the case of 4'-bromobenzo-18-crown-6 as substrate, none of the catalyst systems afforded an acceptable result (entry 6~10, **Table 1.1**). Essentially no reaction was observed.

The initially disappointing results required the replacement of bromobenzo crown ether substrate. The general order of reactivity of functional groups in Sonogashira reactions is: vinyl iodide ≈ vinyl bromide > aryl iodide > vinyl chloride >> aryl bromide.[46,47] Therefore, the replacement of 4'-bromobenzo-18-crown-6 with 4'-iodobenzo-18-crown-6 was presumable to increase the reactivity and we do observed the dramatically enhanced reactivity of iodo-functions under

the same reaction conditions (**Table 1.2**). The 4'-iodobenzo-18-crown-6 was prepared by the previously reported method.[48] By using $Pd_2(dba)_3$ or $Pd(PhCN)_2Cl_2$ as palladium source, in the presence of PPh_3 and TFP ligands, an acceptable yield was obtained and $Pd_2(dba)_3$ proved to be the highest active catalyst (entry 5, **Table 1.2**). The superiority of TFP ligand over PPh_3 and P(*t*-Bu)$_3$ was revealed. In contrast to the previously reported results;[14] the use of bulky electron-rich P(*t*-Bu)$_3$ ligand afforded poor results. The replacement of amine with DMF or THF as solvent afforded a better yield, the present results were similar to those reported previously.[49,50,51]

Table 1.2. Optimization of Sonogashira Couplings of **1.2** with 4'-iodobenzo-18-crown-6

entry	Pd reagent	ligand	base	solvent	Yield of 1.1 (%)
1	Pd(PPh$_3$)$_2$Cl$_2$	N/A	Et$_2$NH	Et$_2$NH	0
2	Pd$_2$(dba)$_3$	PPh$_3$	piperidine	piperidine	15
3	Pd$_2$(dba)$_3$	PPh$_3$	piperidine	DMF	40
4	Pd$_2$(dba)$_3$	P(*t*-Bu)$_3$	piperidine	DMF	< 5
5	Pd$_2$(dba)$_3$	TFP	piperidine	DMF	75
6	Pd(PhCN)$_2$Cl$_2$	P(*t*-Bu)$_3$	piperidine	THF	< 5
7	Pd(PhCN)$_2$Cl$_2$	TFP	piperidine	THF	51
8	Pd$_2$(dba)$_3$	PPh3	KF(no CuI)	DMF	48
9	Pd$_2$(dba)$_3$	TFP	KF(no CuI)	DMF	53

The coupling reaction proceeded smoothly in the presence of potassium fluoride (KF) as an activator and without CuI as a co-catalyst. Albeit the reactivity seemed slightly inferior to that of modified Sonogashira-type protocol. It is worth pointing out that this is the first example of using KF as a direct activator in the Pd-catalyzed coupling reactions of terminal alkynes.[52] Good reactivity of KF as activator in this case is presumably due to the complexion of K^+ with benzocrown ether moiety and fluoride acting as a base. Furthermore, the work-up procedure of the current protocol was much easier, accomplished by filtering the solid precipitate and followed by isolation and purification of the residues by column chromatography. It should be noted that column separating agent was quite important on the purification of target compound **1.1**. When silica gel was used, the target compound sticked and decomposed on the column, poor yield was obtained. In contrast, purification on the alumina column afforded much better yield.

1.7 Conclusion

In this work a protocol was developed to trap solution state structures of Mo-POM with designed chelating agents **1.1** and **1.2**. Especially with **1.1** the distribution of particle sizes and the particle morphologies revealed by TEM study generated repeatable snap shots of dynamic equilibrium of Mo-POM in solution state. Morphological studies and sizing indicated that the nanostructured Mo-POM material in solution is probably best described as hollow spheres with sizes between 3 and 30 nm in radius.

Speculatively, the micrographs obtained thus far indicate that solution state nanostructures can be both smoothly constructed from Mo atomic/molecular building blocks and constructed from discrete clusters the size of keplerates or larger (radii 3-7 nm). While some of the features appeared to be smooth like the objects in **Figure 1.11** (p.25), some features in the micrographs appeared to be the result of the aggregation of nanoscopic species. The distribution of solution state structures of Mo-POM are metrically inhomogeneous but structurally symmetric. The next chapters will describe attempts to characterize equilibrium Mo-POM in solution and attempts to control the distribution of sizes in TEM features by other organic hosts.

1.8 Experimental section

ImageJ, Java^{TM} freeware for image processing and statistical analysis, from (NIH, USA): http://rsb.info.nih.gov/ij/ was used to analyze graphic files generated from the TEM studies.

Solids for TEM analysis. Mo-POM was prepared according to literature procedure.[6] Mo-POM (3.0 mg) dissolved in 2.0 mL H_2O gives a reddish brown solution. Tripodal compound **1.1** (4.0 mg) dissolved in 3.0 mL 0.1 M $KCl_{(aq)}$ with addition of 1N HCl to give a clear yellow solution (pH~3). A precipitate formed immediately upon mixing Mo-POM and **1.1**. Centrifugation, air drying at 25 °C gave **ppt1.1**; All the other precipitates were obtained analogously. **Ppt1.1** (~1 mg) was dispersed in water in a small vial and sonicated for 30 min. A drop of the

dispersion was placed on a lacey carbon copper grid (Lacey Carbon Type-A, Ted Pella, Inc.). After soaking the grid for 2~3 min, the excess solution was removed by filter paper and the grid was allowed to air dried at 25 °C. The material was examined using an Electron Microscope JEOL JEM-2000FX or JEOL JEM-2010F.

Ppt1.1': Approximately 700 µL of the mother liquor of the published procedure[6] were transferred to a 15 mL plastic centrifuge tube, and diluted to 1 mL with deionized water to give a reddish brown solution. A precipitate formed immediately upon mixing this solution with tripodal compound **1.1** (4.0 mg) dissolved in 3.0 mL H_2O (0.1 M $KCl_{(aq)}$ pH~3). Centrifugation followed by air-drying at 25 °C gave **ppt1.1'**.

The solid referred to as keplerate Mo-POM was quickly filtered from a near saturated solution of Mo-POM$_{(aq)}$; subsequently washed with 90% ethanol$_{(aq)}$, absolute ethanol, diethyl ether and finally air-dried at 25 °C. The solid on weighing paper was crushed between the fingers. The TEM lacey carbon grids were used to collect a small amount of the dry material. The samples for keplerate {Mo_{132}} aqueous solution resulted in TEM images devoid of nanostructured material.

Electron Microscopy. The camera constant (CC) of the TEM was determined by adjusting the electron microscope to the same settings for the acquisition of the diffraction pattern in **Figure 1.9** and creating a standard ring diffraction pattern Gold on "Holey" Carbon Film, Ted Pella Inc. product #613. The four rings

34

in this sample correspond to four known lattice spacings: CC = r(ring)$_n$ x (d$_n$) for n=1-4, CC = 48.5 ±0.6mm·Å. The patterns were superimposed and the lattice spacings in the nanostructure of **ppt1.1** were measured from the lengths of segments Xn: d(Xn) = CC/Xn.

General Methods. All reactions were carried out under N_2 or Argon atmosphere. THF was pre-dried over CaH_2 and distilled from sodium and benzophenone. DMF was distilled from CaH_2 and stored over 4-Å molecular sieves under nitrogen. All the other reagents were used as received from commercial sources. ^{1}H NMR and ^{13}C NMR spectra were recorded at 400 MHz and 100MHz respectively. Flash column chromatography was performed on ICN-silica 32-63 (ICN Biomedicals) or Alumina.

N,N'-di-(2-propynyl)-4,4'-trimethylenedipiperidine, **1.4**. Neat propargyl bromide (4.41 mL, 49.5 mmol) was added to commercial 4,4'-trimethylenedipiperidine **1.3** (5.08 g, 24.1 mmol) in 50 mL THF. After the addition of 14.9 mL Et$_3$N, the resulting emulsion was stirred vigorously at 25 °C for 20 h. Diethyl ether and 10% HCl$_{(aq)}$ 50 mL each were added to the reaction mixture and the phases were separated. The aqueous phase was made basic (2M NaOH, 30 mL) and extracted with diethyl ether (3x60 mL). The organic phase was dried over MgSO$_4$. Column chromatography (40-60% EtOAc/hexane gradient elution) gave a light yellow oil pure by NMR (2.90 g, 42%). ^{1}H NMR (400 MHz, CDCl$_3$): δ 1.20-1.34 (m, 12H), 1.68-1.72 (m, 4H), 2.15-2.21 (m, 4H), 2.24 (t, 2H, J=2.4 Hz), 2.86-

2.90(m, 4H), 3.30 (d, 4H, J=2.4 Hz). ^{13}C NMR (100 MHz, CDCl$_3$): δ 23.8, 32.2, 35.1, 36.6, 47.2, 52.6, 73.1, 78.9. EI-MS: m/z: 285 [M-H], 247 [M-C$_3$H$_3$]. Anal. Calcd. for C$_{19}$H$_{30}$N$_2$: C, 79.66; H, 10.56; N, 9.78. Found: C, 79.27; H, 10.88; N, 9.69.

N-(t-butyldimethylsilyl-2-propynyl)-*N'*-(2-propynyl)-4,4'-trimethylenedipiperidine, **1.5**. n-Butyllithium (14.6 mL, 29.2 mmol) was added dropwise to a THF solution of **1.4** (8.35 g, 29.2 mmol, −78 °C, in 100 mL THF) and kept cold for 30 min followed by dropwise addition of TBDMSCl (4.40 g, 29.2 mmol in 40 mL THF). The vessel was allowed to warm to r.t. overnight. The solvent was evaporated and the resulted slurry was dispersed in biphasic diethyl ether and water; the phases were separated and the aqueous phase was exacted with ether, the combined organic phase was dried over MgSO$_4$. Column chromatography (20-60% EtOAc/Hexane gradient elution) gave the title compound as a colorless oil (4.67g, 40%). ^{1}H NMR (400 MHz, CDCl$_3$): δ 0.10 (s, 6H), 0.94 (s, 9H), 1.20-1.34 (m, 12H), 1.68-1.72 (m, 4H), 2.13-2.20 (m, 4H), 2.23 (t, 1H, J=2.4 Hz), 2.83-2.90 (m, 4H, J=10.9 Hz), 3.28-3.29 (d, 2H, J=2.4 Hz), 3.33 (s, 2H) . ^{13}C NMR (100 MHz, CDCl$_3$): δ −4.6, 16.5, 23.9, 26.1, 26.1, 31.9, 32.1, 35.1, 36.5, 36.6, 47.2, 48.1, 52.3, 52.6, 73.1, 73.2, 78.8. EI-MS: m/z: 400 M, 361 [M-C$_3$H$_3$], 343 [M-C$_4$H$_9$], 285 [M-C$_6$H$_{15}$Si], 247 [M-C$_9$H$_{17}$Si]. Anal. Calcd. for C$_{25}$H$_{44}$N$_2$Si: C, 74.93; H, 11.07; N, 6.99. Found: C, 74.87; H, 11.17; N, 7.07.

1,3,5-*tris*-[*N'*-(t-butyldimethylsilyl-2-propynyl)-4,4'-trimethylenedipiperidino-*N*-(2-propyn-3-yl)]benzene, **1.6**. 1,3,5-tribromobenzene (0.99g, 3.145 mmol) and **1.5** (4.155g, 10.38 mmol) was dissolved in 40 mL n-butylamine. The resulting solution was treated with Pd(PPh$_3$)$_4$ (0.363g, 0.314 mmol) and CuI (0.12g, 0.630 mmol) and the solution was refluxed for 72 h. After cooling to r.t., the solvents were evaporated and the residue was extracted into EtOAc, the organic phase was washed with water and brine and dried over MgSO$_4$. Column chromatography (gradient elution: 50-100% EtOAc/Hexane followed by 2-8% MeOH/CHCl$_3$) give a yellow oil (3.0g, 75%) ^{1}H NMR (400 MHz, CDCl$_3$): δ 0.11 (s, 18H), 0.94 (s, 27H), 1.22-1.38 (m, 36H), 1.71-1.75 (m, 12H), 2.25 (dd, 6H, J=11.5, 11.5 Hz), 2.30 (dd, 6H, J=11.5, 11.5 Hz), 2.91 (d, 6H, J~11.5), 2.97 (d, 6H, J=11.5), 3.40 (s, 6H), 3.51 (s, 6H), 7.42 (s, 3H). MALDI-TOF-MS: m/z 1275 [M+H].

1,3,5-*tris*-[*N'*-(2-propynyl)-4,4'-trimethylenedipiperidino-*N*-(2-propyn-3-yl)]benzene, **1.2**. Compound **1.6** (2.28 g, 1.79 mmol) in 20 mL THF at 0 °C, was treated with TBAF (6.5 mL, 1 M, dropwise); the reaction mixture was stirred at 0 °C for 10 min, and then stirred at room temperature for 4 h. After quenching with NH$_4$Cl$_{(aq)}$, extracting into CHCl$_3$, and washing with water, the CHCl$_3$ phase was dried over Na$_2$SO$_4$. Column chromatography (gradient elution: 3-8% MeOH/CHCl$_3$) yielded a hygroscopic residue (1.4 g, 84%). ^{1}H NMR (400 MHz, CDCl$_3$): δ 1.21-1.36 (m, 36H), 1.68-1.74 (m, 12H), 2.13-2.20 (m, 12H), 2.23 (t, 3H, J=2.4 Hz), 2.87 (d, 6H, J=11.5 Hz), 2.94 (d, 6H, J=11.5 Hz), 3.28 (d, 6H,

J=2.4 Hz), 3.47 (s, 6H), 7.40 (s, 3H). ^{13}C NMR (100 MHz, CDCl$_3$): δ 23.9, 32.3, 32.4, 35.2, 35.2, 36.66, 36.68, 47.2, 48.0, 52.7, 53.0, 72.8, 79.2, 83.5, 86.2, 123.7, 134.2. MALDI-TOF-MS: m/z: 932.5 [M+H]. Anal. Calcd. for C$_{63}$H$_{90}$N$_6$·2H$_2$O: C, 78.21; H, 9.79; N, 8.69. Found: C, 78.47; H, 9.76; N, 8.80.

Typical procedure for the preparation of 1.1:

1,3,5-*tris*-[*N'*-(4'-benzo-18-crown-6)-2-propynyl)-4,4'-trimethylenedipiperidino-*N*-(2-propyn-3-yl)]benzene, **1.1.** Pd$_2$(dba)$_3$ (7.9 mg, 8.6 μmol) and CuI (1.6 mg, 8.4 μmol) and TFP (4.1 mg, 17.6 μmol) were added to a dry, 5-mL septum-capped round flask, which was then sparged with argon and charged with 0.5 mL dry DMF. Neat piperidine (32 μL, 323 μmol) and 4'-Iodobenzo-18-crown-6 (124 mg, 283 μmol, dissolved in 1.5 mL DMF) were added via syringe to the stirred reaction mixture. The resulted mixture stirred for 15 minutes at r.t., then compound **1.2** (80 mg, 86 μmol, dissolved in 1 mL DMF) was added dropwise via syringe in a period of 20 minutes. The whole reaction mixture was stirred at r.t. for 24 h. Then the resulted solid was filtered, the solvent was concentrated and the residue was purified by Alumina column chromatography (gradient elution, EtOAc followed by 2-5% MeOH/CHCl$_3$), which yielded a yellow sticky solid (120 mg, 75%). ^{1}H NMR (400 MHz, CDCl$_3$): δ 1.18-1.34 (m, 36H), 1.66-1.80(m, 12H), 2.14-2.22(m, 12H), 2.95 (t, 12H, J=11.8 Hz), 3.46 (d, 12H), 3.69 (s, 12H), 3.70-3.73 (m, 12H), 3.76-3.78 (m, 12H), 3.90-3.93 (m, 12H), 4.12-4.16 (m, 12H), 6.78 (d, 3H, J=8.28 Hz), 6.95 (d, 3H, J=2.00 Hz), 7.01 (dd, 3H, J=8.28, 2.00 Hz), 7.40 (s, 3H). ^{13}C NMR (100 MHz, CDCl$_3$): δ 23.9, 32.4, 35.25, 35.30, 36.7, 48.0, 48.2,

53.0, 53.1, 69.0, 69.5, 70.8, 70.9, 83.5, 83.6, 84.8, 86.2, 113.5, 115.9, 117.2, 123.7, 125.3, 134.2, 148.4, 149.2. MALDI-TOF-MS: m/z 1863 [M+H], 1885 [M+Na]. Anal. Calcd. for $C_{111}H_{156}N_6O_{18}\cdot4H_2O$: C, 68.92; H, 8.13; N, 4.34. Found: C, 69.02; H, 8.26; N, 4.42.

References:

†   The keplerate {Mo_{132}} is the smallest structure with a closed surface found in solid states derived from molybdenum blue; this species was also a convenient basis for the concentration of the many species involved in the aqueous equilibrium of Mo-POM. The concentrations of aqueous Mo-POM blue in this work are always expressed in terms of M keplerate {Mo_{132}}.

(1) Müller, A.; Krickemeyer, E.; Bögge, H.; Schmidtmann, M.; Peters, F. *Angew. Chem. Int. Ed.* **1998**, *37*, 3360.

(2) Müller, A.; Kögerler, P.; Dress, A. W. M. *Coord. Chem. Rev.* **2001**, 222, 193.

(3) Kiriy, A.; Gorodyska, G.; Minko, S.; Jaeger, W.; stepánek, P.; Stamm, M. *J. Am. Chem. Soc.* **2002**, 124, 13454.

(4) Müller, A.; Diemann, E.; Kuhlmann, C.; Eimer, W.; Serain, C.; Tak, T.; Knöchel, A.; Pranzas, P. K. *Chem. Comm.* **2001**, 1928.

(5) Liu, T. *J. Am. Chem. Soc.* **2003**, 125, 312.

(6) Pope, M. T. *Heteropoly and Isopoly Oxometalates*; Springer-Verlag: New York, **1983**.

(7) Pope, M. T.; Müller, A. *Angew. Chem. Int. Ed. Engl.* **1991**, 30, 34.

(8) *Polyoxometalates: From Platonic Solids to Anti-Retroviral Activity:* Pope, M. T., Müller, A., Eds.; Kluwer Academic Publishers: Dordrecht, The Netherlands, **1994**.

(9) Pope, M. T. in *Comprehensive Coordination Chemistry*, *Vol. 3.* Eds.: Wilkinson, G.; Gillard, R. D.; McCleverty, J. A. Pergamon Press, **1987**, pp. 1023-1058.

(10) Müller, A.; Meyer, J.; Krickemeyer, E.; Diemann, E. *Angew. Chem. Int. Ed.* **1996**, *35,* 1206.

(11) Souchay, P. 'Polyanions et polycations', Oauthier-Villars, **1963**.

(12) Treadwell, W. D.; Schaeppi, Y. *Helv. Chim. Acta.*, **1946**, *29*, 771.

(13) Glemser, O.; Lutz, G. *Z. Anorg. Allg. Chem.* **1951**, *264*, 17.

(14) Müller, A.; Meyer, J.; Krickemeyer, E.; Beugholt, C.; Bögge, H.; Peters, F.; Schmidtmann, M.; Kögerler, P.; Koop, M. J. *Chem. Eur. J.* **1998**, *4*, 1000.

(15) Müller, A.; Sarkar, S. S. Q. N.; Bögge, H.; Schmidtmann, M.; Sarkar, S.; Kogerler, P.; Hauptfleisch, B.; Trautwein, A. X.; Schunemann, V. *Angew. Chem. Int. Ed.* **1999**, *38*, 3238.

(16) Müller, A.; Kögerler, P.; Bögge, H. *Structure and Bonding*, **2000**, *96*, 203.

(17) Müller, A.; Diemann, E.; Shah, S. Q. N.; Kuhlmann, C.; Letzel, M. C. *Chem. Commun.* **2002**, *222*, 440.

(18) Berzelius, J. J. Beitrag zur näheren Kenntniss des Molybdäns. *Poggend. Ann. Phys. Chem.* **1826**, 6, 369-392.

(19) Müller, A.; Serain, C. *Acc. Chem. Res.* **2000**, 33, 2.

(20) Gouzerh, P; Proust, A. *Chem. Rev.* **1998**, 98, 77.

(21) Proust, A.; Villanneau, R. In *Polyoxometallate Chemistry, From Topology via Self-Assembly to* Applications; Pope, M. T., Müller, A., Eds.; Kluwer Academic Publishers: Dordrecht, The Netherlands, **2001**, p23-38.

(22) Clegg, W.; Errington, R.; Fraser, K. A.; Lax, C.; Richards, D. G. In *Polyoxometalates: from Platonic Solids to Anti-Retroviral Activity;* Pope, M. T., Müller, A., Eds.; Kluwer Academic Publishers: Dordrecht, The Netherlands, **1994**, p113.

(23) Volkmer, D.; Du Chesne, A.; Müller, A.; *J. Am. Chem. Soc.* **2000**, 122, 1995.

(24) MacGillivray, L. R.; Atwood, J. L. *Angew. Chem. Int. Ed.* **1999**, 38 , 1018.

(25) Müller, A.; Krickemeyer, E.; Meyer, J.; Bögge, H.; Peters, F.; Plass, W.; Diemann, E.; Dillinger, S.; Nonnenbruch, F.; Randerath, M.; Menke, C. *Angew. Chem., Int. Ed.* **1995**, 34, 2122.

(26) Müller, A.; Sarkar, S.; Shah, S. Q. N.; Bögge, H.; Schmidtmann, M.; Sarkar, S.; Kögerler, P.; Hauptfleisch, B.; Trautwein, A. X.; Schünemann, V. *Angew. Chem., Int. Ed.* **1999**, 38, 3238.

(27) Douglas, T.; Young, M. *Nature* **1998**, 393, 152.

(28) Müller, A.; Koop, M.; Bogge, H.; Schmidtmann, M.; Beugholt, C. *J. Chem. Soc. Chem. Comm.* **1998**, 1501.

(29) Sharma, C. V. K.; Clearfield, A. *J. Am. Chem. Soc.* **2000**, *122*, 1558.

(30) Liu, T. *J. Am. Chem. Soc.* **2002**, 124, 10942.

(31) Schinner, F. B. J.; Audrieth, L. F.; Gross, S. T.; McClellan, D. S.; Seppi, L. J. *J. Am. Chem. Soc.* **1942**, *64*, 2543.

(32) Liu, T.; Wan, Q.; Xie, Y.; Burger, C.; Liu, L. –Z.; Chu, B. *J. Am. Chem. Soc.* **2001**, 123, 10966.

(33) Russ, J. C. *Fundamentals of energy dispersive x-ray analysis*, Butterworths, **1984**.

(34) Dziunikowski, B. *Energy dispersive x-ray fluorescence analysis*, Elsevier, 1989.

(35) The X-ray structure of Mo$\{_{132}\}$ keplerate (CSD-410097, Fachinformationszentrum Karlsruhe, CRYSDATA@FIZ-Karlsruhe.DE) had Mo-Mo distances 2.6-3.9 Å.

(36) Sonogashira, K.; Tohda, Y.; Hagihara, N. *Tetrahedron Lett.* **1975**, 4467.

(37) Xia, W-S.; Schmehl, R. H.; Li, C-J. *Tetrahedron* **2000**, 56, 7045.

(38) Hundertmark, T.; Littke, A. F.; Buchwald, S. L.; Fu, G. C. *Org. Lett.* **2002**, 2, 1729.

(39) Davidson, L.; Freebairn, K. W.; Russell, A. T.; Trivedi, H. S.; Hayes, W. *Synlett* **2002**, 251.

(40) Shen, W.; Thomas, S. A. *Org. Lett.* **2000**, 2, 2857.

(41) Mori, A.; Kawashima, J.; Shimada, T.; Suguro, M.; Hirabayashi, K.; Nishihara, Y. *Org. Lett.* **2000**, 2, 2935.

(42) Böhm, V. P. W.; Hermann, W. A. *Eur. J. Org. Chem.* **2000**, 3679.

(43) Lee, H. B.; Huh, D. H.; Oh, J. S.; Min, G-H.; Kim, B. H.; Lee, D. H.; Hwang, J. K.; Kim, Y. G. *Tetrahedron* **2001**, 57, 8283.

(44) Ander, N. G.; Keay, B. A. *Chem. Rev.* **2001**, 101, 997.

(45) Farina, V.; Baker, S. R.; Benigni, D. A.; Sapino, C. *Tetrahedron Lett.* **1988**, 29, 5739.

(46) Sonogashira, K. In *Metal-Catalyzed Cross-Coupling Reactions*; Diederich, F., Stang, P. J., Eds.; Wiley-VCH: New York, **1998**, Chaper 5.

(47) Sonogashira, K. In *Comprehensive Organic Synthesis*; Trost, B. M., Eds; Pergamon: New York, **1991**, Chapter 2.4.

(48) Kajigaeshi, S.; Kakinami, H.; Yamasaki, H.; fujisaki, S.; Kondo, M.; Okamoto, T. *Chem. Lett.* **1988**, 795.

(49) Saito, I.; Yamaguchi, K.; Nagata, R.; Murahashi, E. *Tetrahedron Lett.* **1990**, 31, 7469.

(50) Buszek, K. R.; Yeong, J. *Synth. Commun.* **1994**, 24, 2461.

(51) Miller, M. W.; Johnson, C. R. *J. Org. Chem.* **1997**, 62, 1582.

(52) Although one reference has demonstrated that Sonogashira couplings of aryl iodides with terminal alkynes occurred on Pd-KF/Al_2O_3 under microwave activation, Pd and KF must be supported on Al_2O_3. Without Alumina, the reaction would be out of control. Kabalka, G. W.; Wang, L.; Namboochiri, V.; Pagni, R. M. *Tetrahedron Lett.* **2000**, 41, 5151.

Chapter 2

Guest-induced Molecular Recognition of Mo-POM

In **Chapter 1**, we developed a rational protocol for the kinetic precipitation of Mo-POM with designed chelating agents **1.1** and made the argument that with **1.1** the distribution of particle sizes and the particle morphologies revealed by TEM generated repeatable snap shots of dynamic equilibrium of Mo-POM in solution. To further assay the feasibility of this protocol, we synthesized bipodal and tripodal derivatives of crown **1.1** and hexamine **1.2** (**Figure 2.1**).

1.1, X =

2.1, X =

2.2, X =

1.2

2.3

2.3a: Y, Z = benzocrown-3-yl
2.3b: Y = H, Z = benzocrown-3-yl
2.3c: Y = TBDMS, Z = benzocrown-3-yl
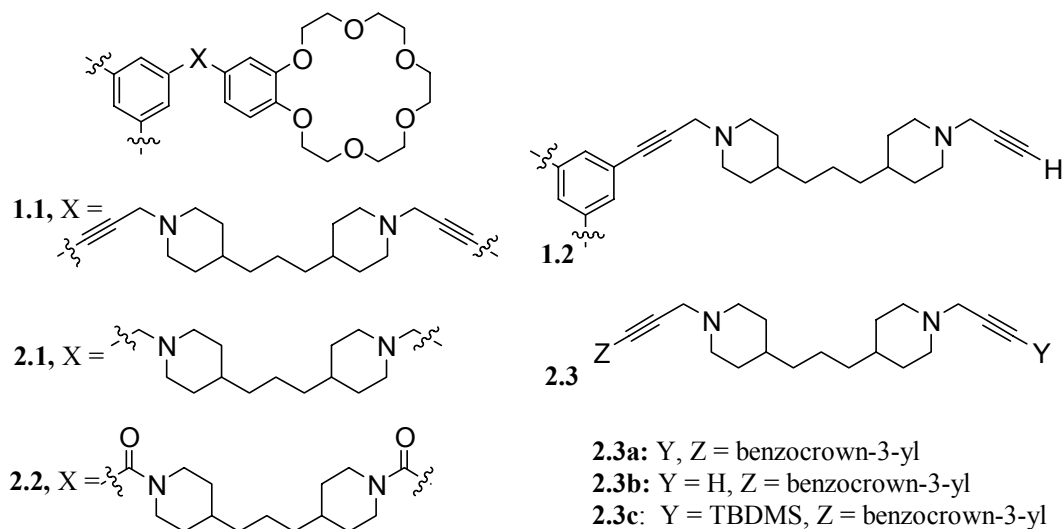
Figure 2.1. The polyamine crown ether derivatives used in this study.

Diamines related to crown **1.1** and to hexamine **1.2** did not succeed in trapping and stabilizing the Mo-POM solution state. Likewise, other tripodal structures, which have different sizes and electronic properties with **1.1**, were

also less successful. Another interesting aspect of the study was the observation of guest-induced molecular recognition when different Mo-POM was assayed. Studies with a series of structurally analogous hosts probed the relationship between the structure of the molecular host and the formation of nanostructural Mo-POM.

2.1 Introduction (of the chemical literature on molecular-level encapsulation)

The changes in properties incurred when molecules are entrapped have interested scientists for several decades. The first examples of these enclosed structures based on covalent bonds in which the near-spherical hosts enclose their guests, remarkable examples are cryptophanes[1] and carcerands.[2,3] Shortly after the optimization of the synthesis of fullerene C_{60}, investigators encapsulated heavy metal atoms, noble gases and diatomic molecules in the fullerene cage.[4,5] Likewise, fullerene itself has also been encapsulated by calixarenes[6,7] and amphiphilic block polymers.[8,9] Viruses devoid of nucleic acids have been used to encapsulate polyoxometallates and control nucleation.[10] Subsequently, well-defined supramolecular architectures have been constructed by means of simultaneous self-assembly of multi-components with noncovalent interactions. A characteristic feature of these architectures is that they all contain inner cavities for inclusion of a guest. Various supramolecular assemblies have been constructed in the past few decades; the following section presented a brief overview of the literature that inspired the current work.

2.2 Molecular recognition by self-assembly and encapsulation

2.2.1 Hydrogen-bonded encapsulated enclosures

Studies designed to probe the chemical significance of molecular encapsulation indicate that molecules with mild curvature and compatible edges can form enclosures;[11] remarkable examples are glycoluril-derived hydrogen-bonded capsules possessing curvature and complimentary hydrogen bonds donors and acceptors on the perimeter dimerized effectively and produced cavities in which other molecules fit. The first examples were called "tennis-balls",[12,13] a series of homodimeric capsules assembled through hydrogen bonding of two self-complimentary glycoluril-based subunits **2.4**. Tennis balls can accommodate small organic molecules in their interior cavities. Continuous work on the modification of glycouril spacers led to larger self-assembled capsules, "softballs".[14-16] Of those, the enclosed cavities were capable of encapsulating larger organic molecules, such as 1-adamantanecarboxylic acid and 1-ferrocenecarboxylic acid. Another remarkable aspect of these capsules is their ability of binding two suitable guests simultaneously, making them potential molecular vessels for bimolecular chemical reactions.
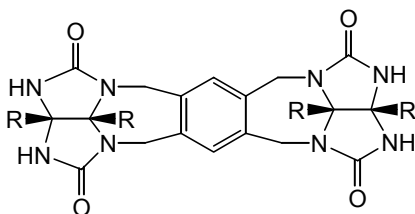
2.4a: R = Ph
2.4b: R = COOEt
2.4c: R = 4-dimethylaminophenyl
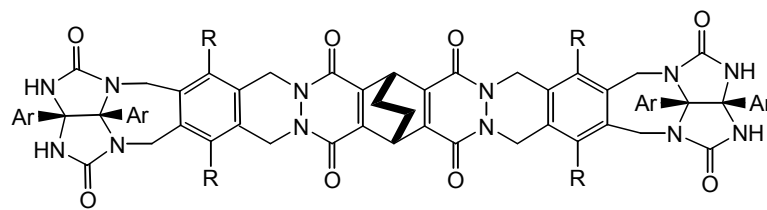
2.5a: R = H
2.5b: R = OH
Ar = 4-n-heptylphenyl

Figure 2.2. Glycoluril-type molecular subunits for the construction of supramolecular structures.

Calixarene and resorcinarene are also attractive subunits for self-assembled enclosures. Both molecules accommodate various modifications imposed on their innate perimeters. Atwood and co-workers[17] reported a virus-like structural mimic, a chiral and spherical structure assembled by six resorcinarene subunits **2.6** through 60 hydrogen bonds which enclose a cavity of about 1375 $Å^3$. Rebek and co-workers[18] synthesized a cylindrical molecular container based on the resorcinarene motif. The authors installed four imides functions around the rim of vase-shaped resorcinarene **2.7** acting as both hydrogen-bonding donors and acceptors; the self-assembling result was a dimeric supramolecular capsule.[18] The capsule was capable of encapsulating elongated aromatic compounds. Furthermore, the two encapsulated aromatic compounds were arranged in an edge-to-edge manner and selected pair-wise on the basis of their particular sizes and shapes, making them potential candidates as carriers for bimolecular reactions.[18]

2.6a: R=Me
2.6b: R=C$_{11}$H$_{23}$

R=C$_{11}$H$_{23}$

2.7
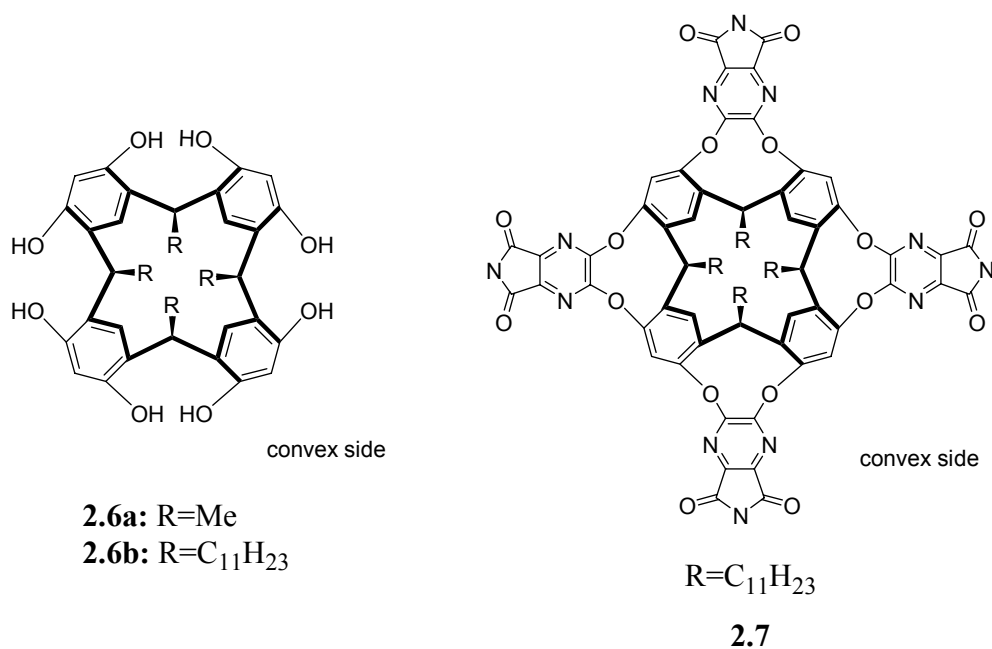
Figure 2.3. Calixarene and resorcinarene subunits for the construction of supramolecular structures.

A glycoluril-resorcinarene hybrid supramolecular capsule has been developed[19] and reversibly encapsulated by ionic cryptate complex within the enormous cavity, leading to a "host-within-host" complex, a molecular analogy of the well-known Russian Matryoshka dolls. A molecular gyroscope based on the same "host-within-host" motif has been published recently by Day and co-workers.[20] The inclusion of a smaller cucurbit[5]uril which can rotate freely and independently in a larger analogue cucurbit[10]uril ring was observed for the first time. The authors named this novel supramolecular complex "gyroscane', a molecular analogy to a gyroscope.

2.2.2 Metal-ligand interactions-based encapsulated enclosures

Hydrogen bonds are not the only weak forces that can contribute to the construction of supramolecular enclosures. Synthesis of supramolecular structures from transition-metal ions and organic ligands by self-assembling strategy has also received much attention in the past decade. Whilst enclosures with hydrogen bonds require molecular components with complimentary curvature elsewhere, metal-ligand-directed assemblies required complimentary convergent/divergent binding sites elsewhere. Of these assemblies, the protected metals act as linkers to connect multiple molecular templates to construct well-defined enclosures.

A great breakthrough for the construction of supramolecular systems through metal-directed self-assembling methodology was mainly contributed by Fujita's group. In their design, they exploit triangular motifs, the most efficient building blocks for the construction of three-dimensional polyhedron,[21] coupled with *cis*-protected square-planar Pd and Pt complexes, for the construction of highly symmetric supramolecular assemblies.[22] Of these systems, metal ions linked triangular templates at the corners or edges, the enclosed cavities are capable of binding a series of organic guests. By carefully installing binding sites at the triangular ligands, a variety of polyhedral architectures can be constructed by rational design. **Figure 2.4** shows the triangular templates used for the construction of supramolecular structures and the resulting polyhedral complexes. A general review of these striking systems has been published.[22]
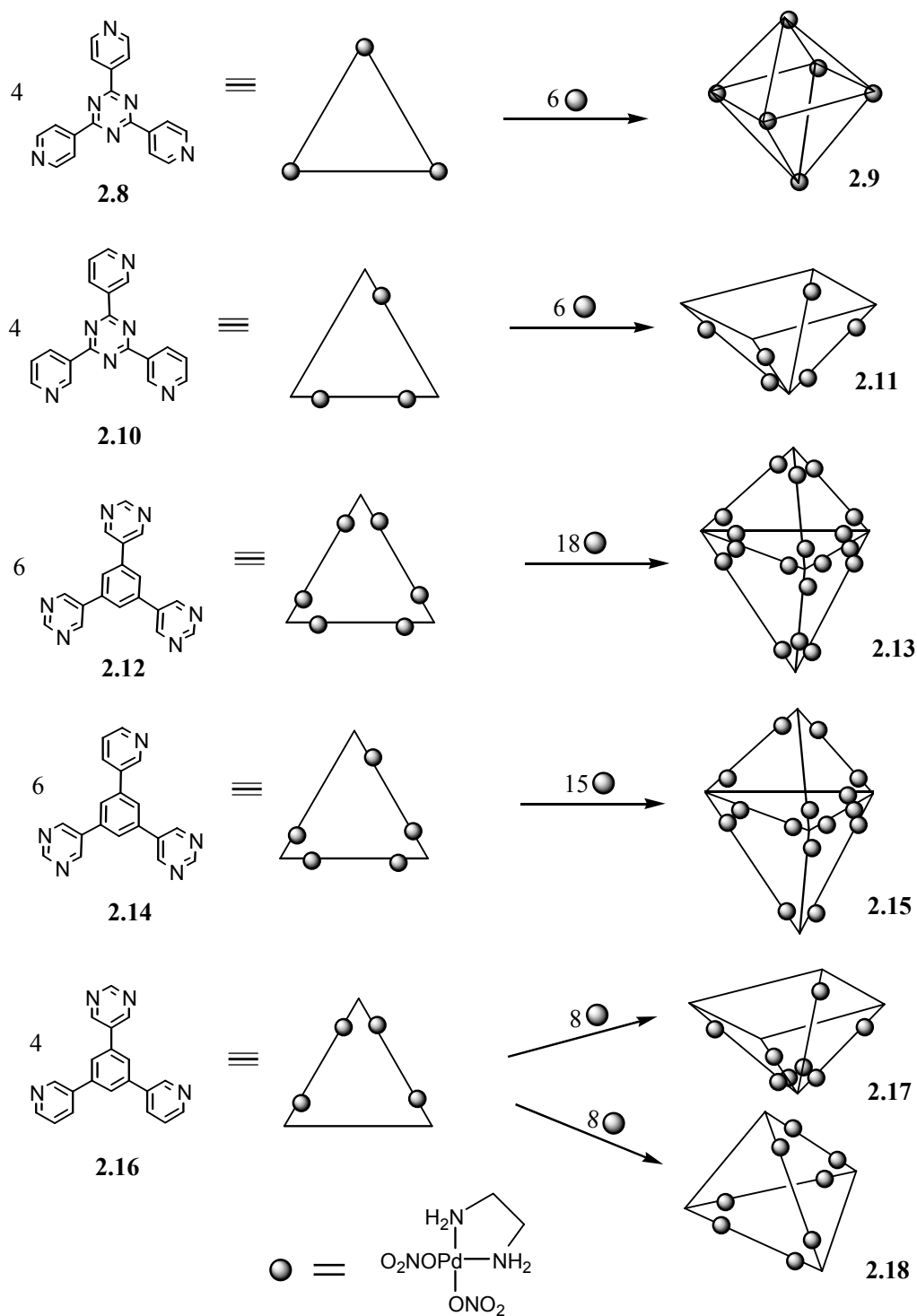
Figure 2.4. Triangular templates for the construction of supramolecular structures and the resulting supramolecular capsules in Fujita's work.

Among the striking systems constructed by triangular building blocks in Fujita's work, a remarkable system should be mentioned specially, in which a guest-induced mechanism was observed with a C_2-symmetric ligand **2.16**.[23] Since ligand **2.16** was C_2-symmetric, two arrangements in the self-assembling process were possible: parallel and anti-parallel fashions. The results were two conformations based on different guests. That is, an open core structure **2.17** was formed in the presence of some large guests (e.g. dibenzoyl), whereas a closed-shell tetrahedral structure **2.18** was induced by guest CBr_4. Both structures consist of four triangular units and eight metal atoms and are interconvertable by guest exchange.

In a different approach but based on the same design principles, a particularly beautiful molecular sphere corresponding to M_6L_8 was constructed from a more flexible tripodal ligand **2.19** and $Pd(NO_3)_2$.[24] In this system, each Pd(II) center coordinated with four tripodal molecules and the surface of sphere was spanned by eight tripodal molecules.
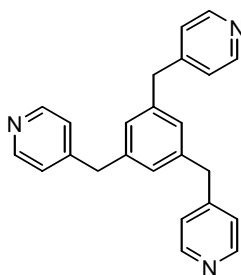
2.19

The triangular motif was also exploited by Stang's group. In their systems, they again used a square-planar metal Pd or Pt complex with one labile ligand (OTf) and two stable ligands (PPh_3).[25] Firstly, the metal complex was substituted

directly on the triangular subunit through chemical transformations, then the pre-designed structure was achieved by addition of another molecular component, a pyridyl-containing ligand **2.21** with a V-shape. The result was a nanoscaled cubeoctahedron, one of the Archimedian solids. Based on the same design principles, a similar cuboctahedron was constructed by pyridyl-contaning triangular ligand **2.22** and V-shaped Pt-derived benzophone derivative **2.23**. Unfortunately, the authors didn't obtain discrete crystal structures for the two cuboctahedrons.
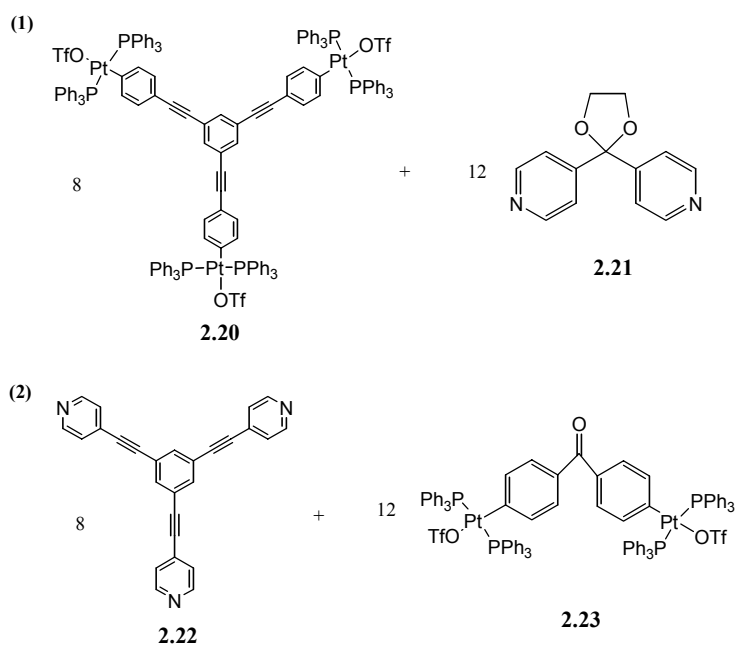
Figure 2.5. Self-assembly of cubeoctahedron in stang's work.

Not only triangular motifs have been exploited in supramolecular chemistry; other molecular subunits have also been explored. In contrast to aforementioned systems, an important work should be mentioned.[26, 27] Raymond and co-workers exploited a rigid C_2-symmetric subunit **2.24**, which contained

catechol functions as binding sites to metal ions (e.g. Fe^{III}, Ga^{III}, Ti^{IV}), leading to an impressive M_4L_6 tetrahedron. The resulting tetrahedron carried "–12" charges, making it potential host for cationic guests. Indeed, the selective binding of Et_4N^+ over Et_4Si has been demonstrated.[27] More remarkable is the tunability of the volume of the isolated cavity, namely changing from 250 to 350 $Å^3$ according to the sizes of guests.
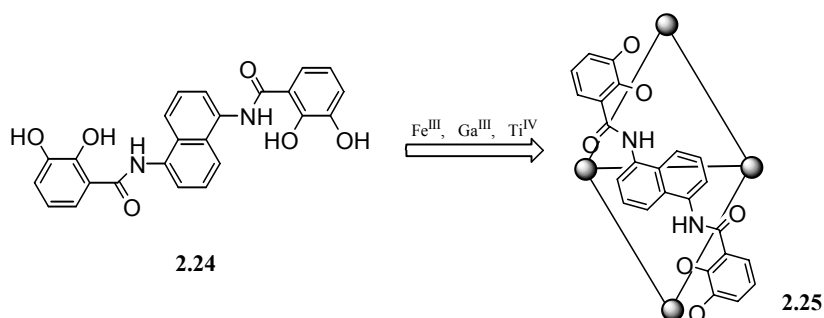
Figure 2.6. Self-assembly of tetrahedral supramolecular assembly.

Calixarene and resorcinarene are also potent molecular components for metal-directed self-assembling process. Atwood and co-workers reported a nanoscale, spherical cluster[28] assembled from a water-soluble *p*-sulfonatocalix[4]arene by addition of 1 equivalent of pyridine N-oxide and 0.5 equivalent of $Ln(NO_3)_3$. The assembly process is driven by synergism between many non-covalent forces, such as hydrogen bonds, van der Waals forces, metal-ligand interactions and electrostatic interactions. The internal volume was impressive (about 1700 $Å^3$) and was occupied by two sodium ions and 30 water molecules. They found the stoichiometry of the reagents determined the shape of the resulting superstructure, in some cases the same three subunits formed open-ended helical tubes instead.[28] In recent work, Shinkai and co-workers

combined both advantages of cyclophane and pyridyl ligand.[29] The rigid pyridyl-derived calix[4]arenes assembled with square-plannar Pd complex to form a dimeric capsule. The bis-crown functions at the lower rim of calixarenes were an essential point for the stability of C_{4V}-symmetric calix[4]arenes, only this monomer led to metal-mediated self-assembling.

2.2.3 Encapsulated enclosures induced by electrostatic interactions

Highly symmetric supramolecular architecture based on noncovalent interactions is a general motif adopted in nature. For example, viruses have perfected molecular-level encapsulation for the delivery of genetic material to host cells.[30,31] Among the possible geometric forms that the viral capsid could have adopted, nature seems to have its own selection exclusively for the symmetrical structures. The fact that different viruses adopt similar structures hints at a general optimized utility for the self-assembly process. Even though questions still remain about the structural and functional nature of the viral capsid/polynucleotide ensemble, the general interaction with the protein coat is probably coulombic, non-specific and non-directional. The great losses in entropy incurred upon assembly of the virus must be compensated by an enthalpy benefit due to complementary coulombic interactions between the polycationic protein coats and the polyanionic nucleotide chains. The strong cationic protein-anionic polynucletide motif reappears often in nature. However, encapsulation complexes assembled by electrostatic or coulombic interactions are largely underestimated in molecular-level encapsulation. Caruso and co-workers[32]

reported a reversible hollow capsule based on DNA and a naturally occurring polyamine, spermidine (SP) which carries positive charges when protonated. The hollow capsule has potential applications in drug delivery.

A beautiful virus-like superstructure has been recently published by Dubois *et al*.[33] A hollow icosahedral structure was assembled in a salt-free mixtures of anionic and cationic surfactants. The resulting structures have an impressive size of about one micrometer, making them larger than any known icosahedral viruses.[34] The structure carries negative charges due to the excess of anionic surfactant, making them potential hosts for cationic guests. More remarkable is the formed aggregates stabilized by the presence of pore (diameter of about 150 Å) at the vertices of the icosahedron, making them attractive candidates for controlled drug or DNA release.

Although there are some examples of complexes constructed by ionic building blocks such as charged surfactants, lipids, polyelectrolytes and charged dyes, generally they do not form enclosed superstructures. For a more detailed discussion on the topic of ionic self-assembly, the readers can see a very recent review by Faul and Antonietti.[35]

2.3 Model compounds for molecular recognition of Mo-POM

The current work focused on the development of a recognition motif that can be described as viral-like. Derivatives **1.1, 2.1** and **2.2** are tripodal, amino-benzocrowns with the potential to assemble spherical enclosures around keplerate-like structures in a manner analogous to the construction of the

platonic solids by joining the edges and the vertices of equilateral triangles. Differences in the interaction of **2.2** and Mo-POM were used to evaluate the effect of the ammonium groups. Likewise **1.2** unveiled the effect of the crown ether. Compounds **2.3** probed the structural effect of the tripodal motif. The solubility of Mo-POM decreases with increasing ionic strength due to destruction of the hydration shell.[36] Likewise, strong electrostatic interactions in **1.1** and **2.1-2.2** should have synergistically contributed to the stability of an insoluble complex between tripodal compound and anionic Mo-POM. The amine functionality in **1.1** and **2.1-2.2** takes on positive charge below pH 7 by protonation. Likewise crown ethers associate with H_3O^+, NH_4^+ or K^+ and thereby can take on positive charge. In the recognition of Mo-POM**,** the crowns in **1.1-2.3** would probably chelate NH_4^+, the keplerate counter ion. The host molecules could make Van der Waals contact on the surface of Mo-POM at the crown ethers: a compatible interaction.[37] This would provide a stabilizing element for the molecular recognition of Mo-POM.

2.4 Results and discussion

2.4.1 Aggregation behavior of organic hosts with keplerate Mo-POM

Controlled formation of precipitates required solubility of organic hosts and keplerate $\{Mo_{132}\}$ in similar media. Tripodal **1.1** in 0.1M KCl became soluble below pH 5 as determined by simultaneously decreasing pH and monitoring the UV absorbance of the liquid phase at 290nm. The keplerate $\{Mo_{132}\}$ is one of the smallest structure with a closed surface found in solid states derived from

molybdenum blue solutions;[38] this species was also a convenient basis for the concentration of Mo-POM in these studies. A similar titration monitored at 455 nm showed that Mo-POM (~6 x 10^{-10} M based on keplerate {Mo_{132}}) irreversibly decomposed above pH 7. The result was expected because synthesis of Mo-POM required low pH and high polyoxomolybdate concentration. Tripodal **2.1** and **2.2** can directly dissolve in 0.1M KCl aqueous solution, in order to control all the complexion experiments under the same condition; HCl was added to adjust the pH value of the host solution to ~3. The complexion was simple: Whilst a certain stoichiometric ratio of organic host and keplerate Mo-POM mixed together, concomitant precipitation of a brick red solid formed immediately. The liquid mixture stood at room temperature for 24 h. Then centrifugation for 25 minutes followed by removal of the supernatant and collection of the solid followed by drying at room temperature gave desired aggregates. However, the resulting rust colored coprecipitates **ppt1.1-2.3** were insoluble in water between pH 1-11 and insoluble in organic solvents. The solubility of Mo-POM decreases with increasing ionic strength via destruction of the hydration shell;[35] Tripodal hosts should have precipitate Mo-POM by dehydration. Adding aqueous **1.1-2.3** to Mo-POM and monitoring the absorbance of Mo-POM (455 nm) indicated that coprecipitation removed Mo-POM from solution in stoichimetries of 5:1 to 25:1 (**Figure 2.7).**
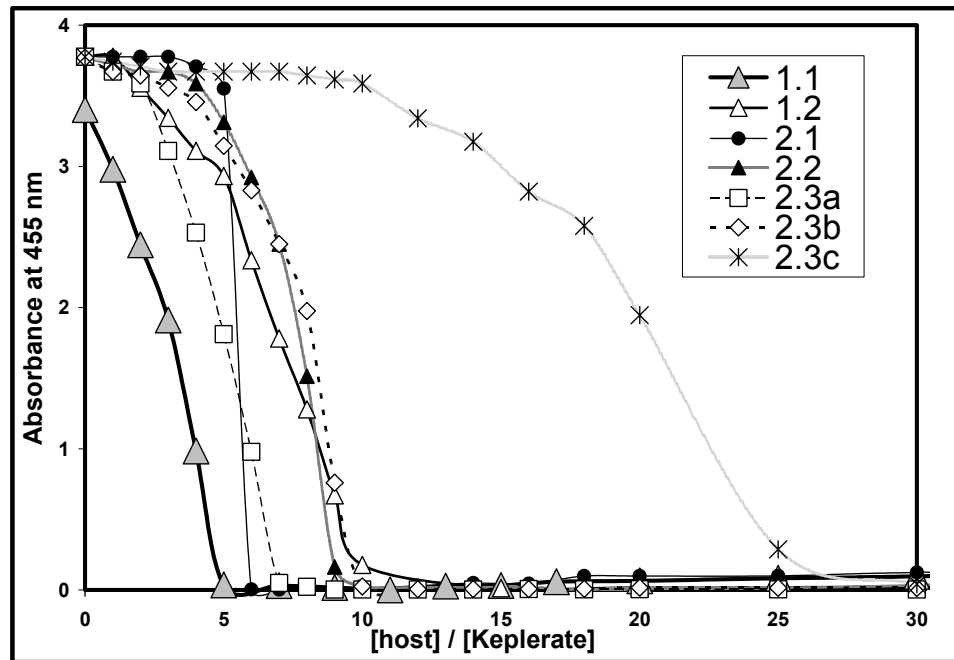
Figure 2.7. Organic hosts were used to precipitate Mo-POM (1.75 X 10^{-5} M). Aqueous Mo-POM was monitored by UV at 455 nm.

Comparing the ability of **1.1-2.3** to precipitate Mo-POM in **Figure 2.7** indicated that tripodal hexamine and benzocrown synergized to chelate Mo-POM. When both crown ether and diamine were present in the tripodal system, precipitation was most efficient. Host **1.2** and **2.3b** behaved similarly even though **1.2** did not possess a crown ether. Steric interactions between **2.3c** and Mo-POM apparently impeded the formation of coprecipitate **ppt2.3c**. This result hinted that precipitation was probably an intimate event, dependent on a good fit between tripodal hosts. Simple destabilization of the aqueous shell of Mo-POM upon binding of the crown should have enhanced formation of **ppt2.3c** over **ppt2.3b** due to the increased hydrophobicity of **2.3c**. The behavior of precipitation of

tripodal **2.1** and **2.2** with Mo-POM was analogous to tripodal crown **1.1**. The tripodal amine **2.1** precipitated Mo-POM more efficient than tripodal amide **2.2** and the appearance of the resulting solid was similar. Furthermore, the titration of keplerate Mo-POM(aq) with excess **1.1-2.3** left very little Mo-POM in solution detectable by UV. Kinetic entrapment of Mo-POM with chelating agents **1.1-2.3** followed by UV spectroscopy didn't proceed well because the precipitation is so fast and the immediate formed precipitates interfered with the detection of absorbance.

2.4.2 Guest-induced fit for molecular recognition of Mo-POM

Coprecipitates formed from bipodal derivatives **2.3** and keplerate Mo-POM were similar in appearance to **ppt1.1** and **ppt1.2**. However, these diamines did not succeed in trapping and stabilizing the keplerate Mo-POM solution state. In the TEM surveys of **ppt2.3**, we can not observe the same spherical features as those in **ppt1.1**, probably suggesting the importance of the three-fold symmetric subunits motif on the molecular recognition of Mo-POM. Furthermore, other tripodal hosts **2.1** and **2.2**, which have different size and electronic properties, were also less successful in trapping and stabilizing keplerate Mo-POM. Micrographs of **ppt2.1** and **ppt2.2** were repeatedly devoid of discrete features with radii greater than 2 nm. However, some interesting features were trapped in high-magnification TEM micrographs; apparently an ordered solid lattice assembled during the precipitation process (**Figure 2.8**).
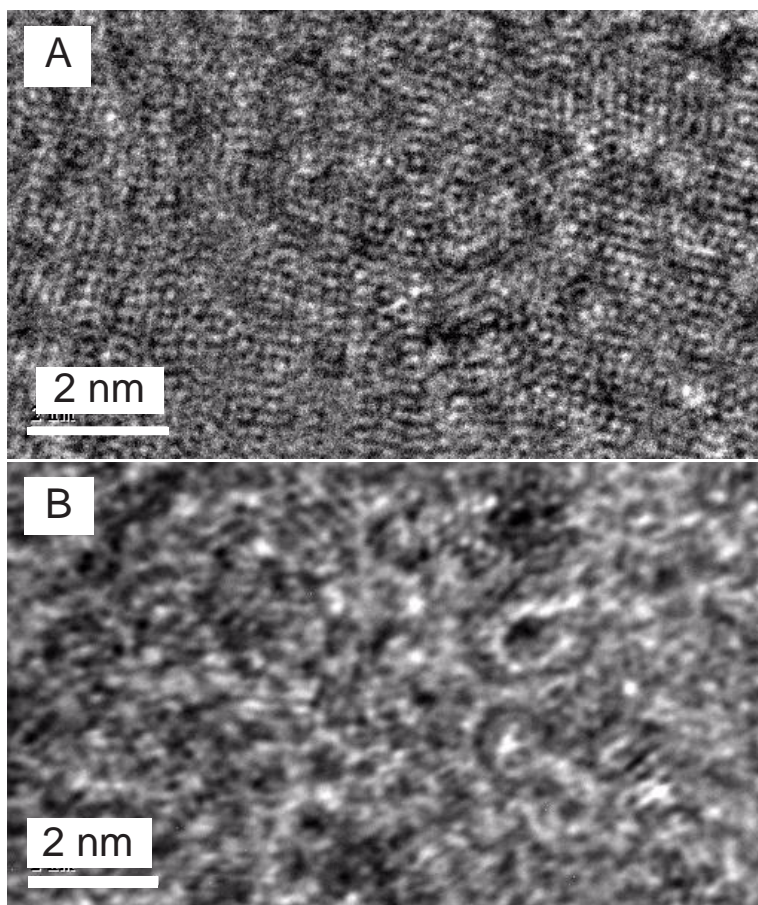
Figure **2.8.** High-resolution TEM micrographs (JEOL 2010F) of **ppt2.1** (**A**) and **ppt2.2** (**B**) (Step **B** in page 2: **Figure 1.1**). The preparations of **ppt2.1** and **ppt2.2** were the same as those of **ppt1.1**.

From the initial results of **Chapter 1**, we know that the Mo-POM solution state hasn't achieved equilibrium state when kinetic precipitation occurs, therefore one of two hypotheses may account for the difference in these micrographs. In the first hypothesis tripodal **1.1** kinetically trapping polydisperse, solution state Mo-POM before reversion to keplerate or before a solid lattice could assemble. The composite material is stable enough to image by TEM, whereas **2.1** and **2.2** either prefer assembly of a solid lattice or the solid state of

ppt2.1 and **ppt2.2** decomposed prior to TEM analysis. In the second hypothesis the discrete nanostructure in **ppt1.1** was not only dependent on native structure in Mo-POM but also relied on complementarity between **1.1** and Mo-POM. That is, the nanoscopic structures in **ppt1.1** depend at least partly on the interactions between Mo-POM and functionality of **1.1**. These two hypotheses are difficult to unambiguously separate. The first hypothesis is favored by the observation that the precipitations were fast complete within seconds and likely diffusion controlled, whereas the super-sized structures of aqueous state Mo-POM require two-three days to evolve.[39] However, more evidence are necessary for the second hypothesis.

In order to gain more information to verify the hypothesis that the formation of nanostructures probably relies partially on the synergism between the molecular host and Mo-POM, a giant wheel-shaped Mo-POM with an outer diameter 3.4 nm and inner diameter about 2.0 nm: **(NH$_4$)$_{28}$[Mo$_{154}$(NO)$_{14}$O$_{448}$H$_{14}$(H$_2$O)$_{70}$·xH$_2$O (x $\approx$ 350)** (Mo-POM2),[40] was assayed as Mo-POM source. {Mo$_{154}$} is a representative of the family of wheel-shaped Mo-POMs prepared by partially reducing Mo^{VI} to Mo^{V} in acidic aqueous solution. New blue coprecipitates formed immediately by mixing **1.1**, **2.1** and **2.2** solution respectively with Mo-POM2 solution in a 20:1 ratio under the same conditions for the preparation of **ppt1.1**. TEM analysis revealed nanoscopic features in **ppt2.2-2** whereas micrographs of **ppt1.1-2** and **ppt2.1-2** were devoid of discrete nanoscopic features with radii greater than 4 nm (**Figure 2.9**).
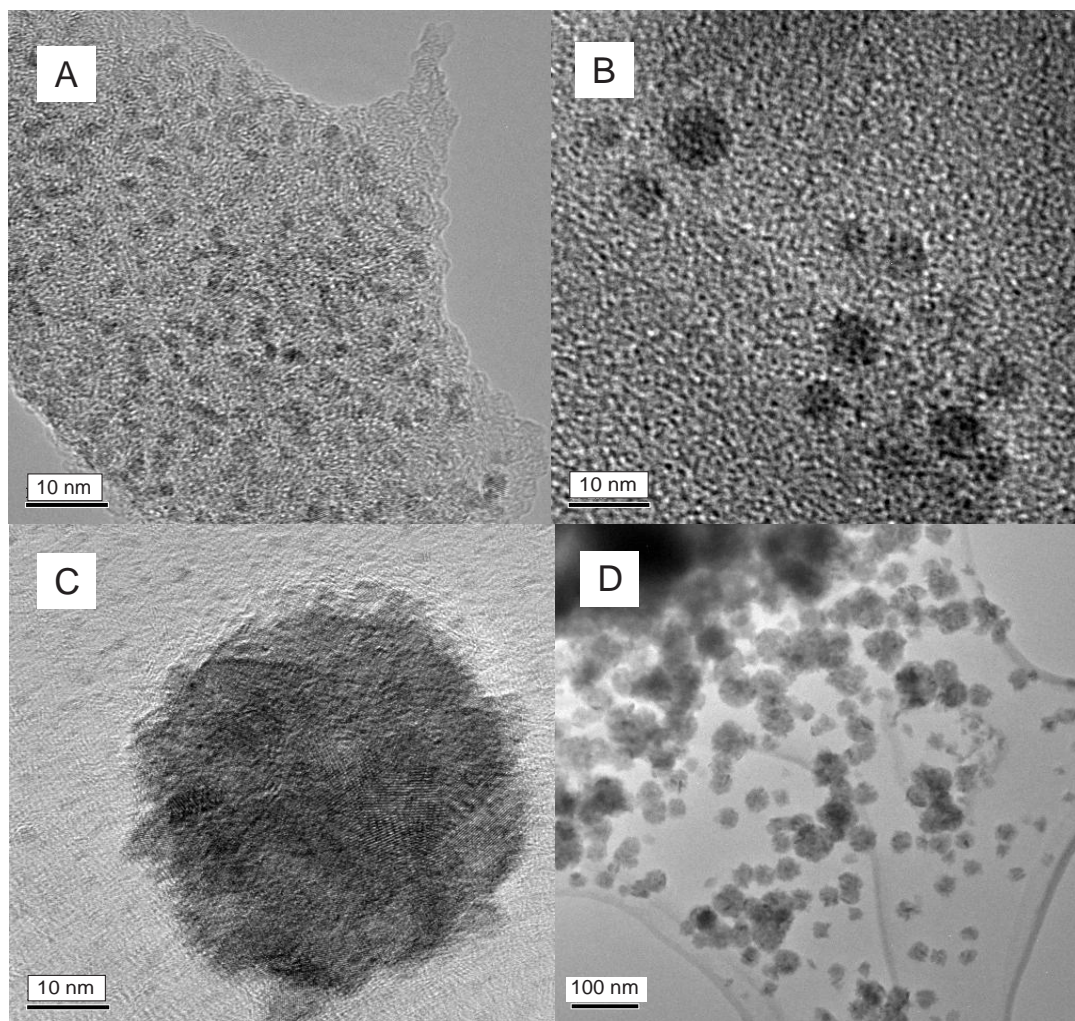
Figure 2.9. Micrographs (JEOL JEM-2010F) of **ppt1.1-2** (**A**), **ppt2.1-2** (**B**) and **ppt2.2-2** (**C** and **D**). These precipitates were prepared analogously to **ppt1.1**.

More remarkably, the crystal growth probably dominated the formation of the Mo-containing features in the micrographs of **ppt2.2-2** because an apparently ordered crystalline lattice was observed in one discrete particle at high magnification (**Figure 2.9C**); indicating the construction of the nanoscopic features appeared to be a shell of molybdate at the molecular level instead of aggregates of stable nanoscopic building blocks such as $\{Mo_{154}\}$ giant wheel.

Furthermore, the nanoscopic features in **ppt2.2-2** were not as circular as those of **ppt1.1**.
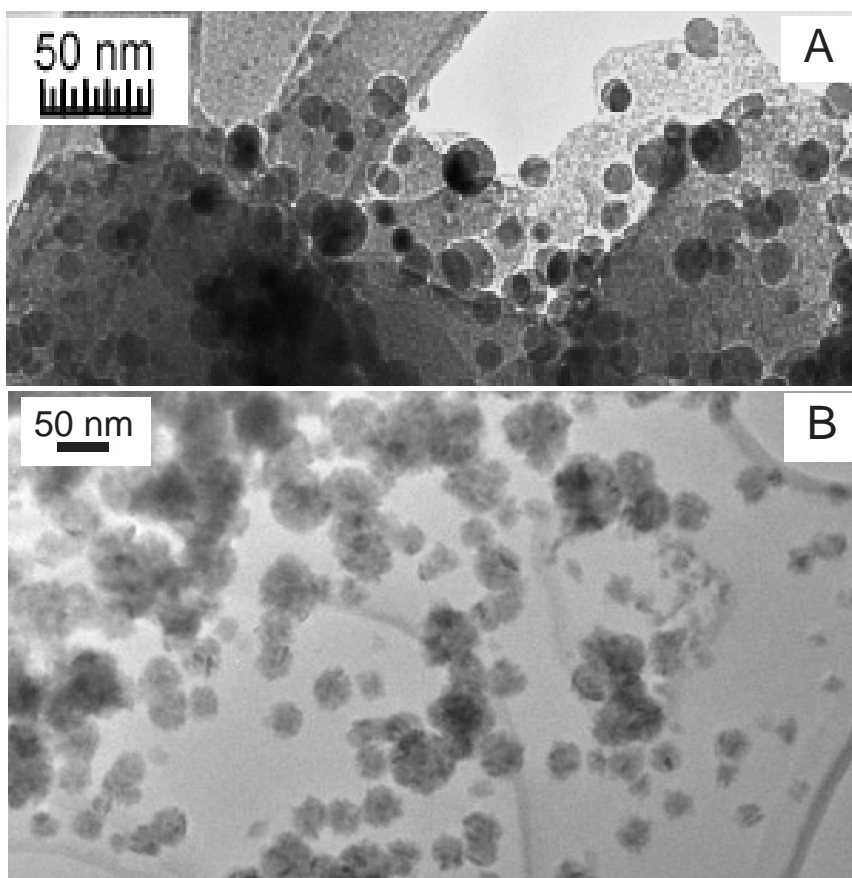
Figure 2.10. TEM micrographs of **ppt1.1** (**A**) and **ppt2.2-2** (**B**).

Compare **Figure 2.10A** with **2.10B**, particles in the **ppt2.2-2** were clearly larger than those of **ppt1.1**. Likewise, the surface of the spheres in **ppt1.1** was continuous and smooth but flat edges and vertices were presented around the surface in the structures of **ppt2.2-2**; presumably due to the domination of crystal growth in the formation of the Mo-containing features.[41]

The observations from the TEM surveys suggest that a guest-induced fit mechanism probably was involved in the molecular recognition of Mo-POM by

designed tripodal hosts; because discrete nanoscopic features only formed in certain cases. Perhaps size/shape and electronic complementarity between molecular host and guest are necessary. Compare the three tripodal hosts, hosts **2.1** and **2.2** are 90% size of host **1.1**. Electronic properties of **2.1** are similar to **1.1** but structure **2.2** removes the cationic character of the host. These differences presumably have influence on synergism between tripodal hosts and Mo-POMs.

2.5 Synthesis

2.5.1 Synthesis of bipodal derivatives 2.3

The synthetic methodologies for bipodal derivatives **2.3a-2.3c** were similar. The synthetic route was outlined in **Figure 2.11**. It was noteworthy that 4'-bromobenzo-18-crown-6 worked well as substrate for the Sonogashira coupling reaction in this case.

Compound **1.4** (N,N'-dipropargyl-4,4'-trimethylenedipiperidine) coupled directly with two equivalents of 4'-bromobenzo-18-crown-6 employing typical Sonogashira reaction conditions afforded bipodal compound **2.3a** in modest good yield. Similarly, treatment mono-TBDMS-protected alkyne **1.5** with 4'-bromobenzo crown under the same conditions yielded intermediate **2.3c**, followed by removal of TBDMS protecting group afforded bipodal derivative **2.3b**.
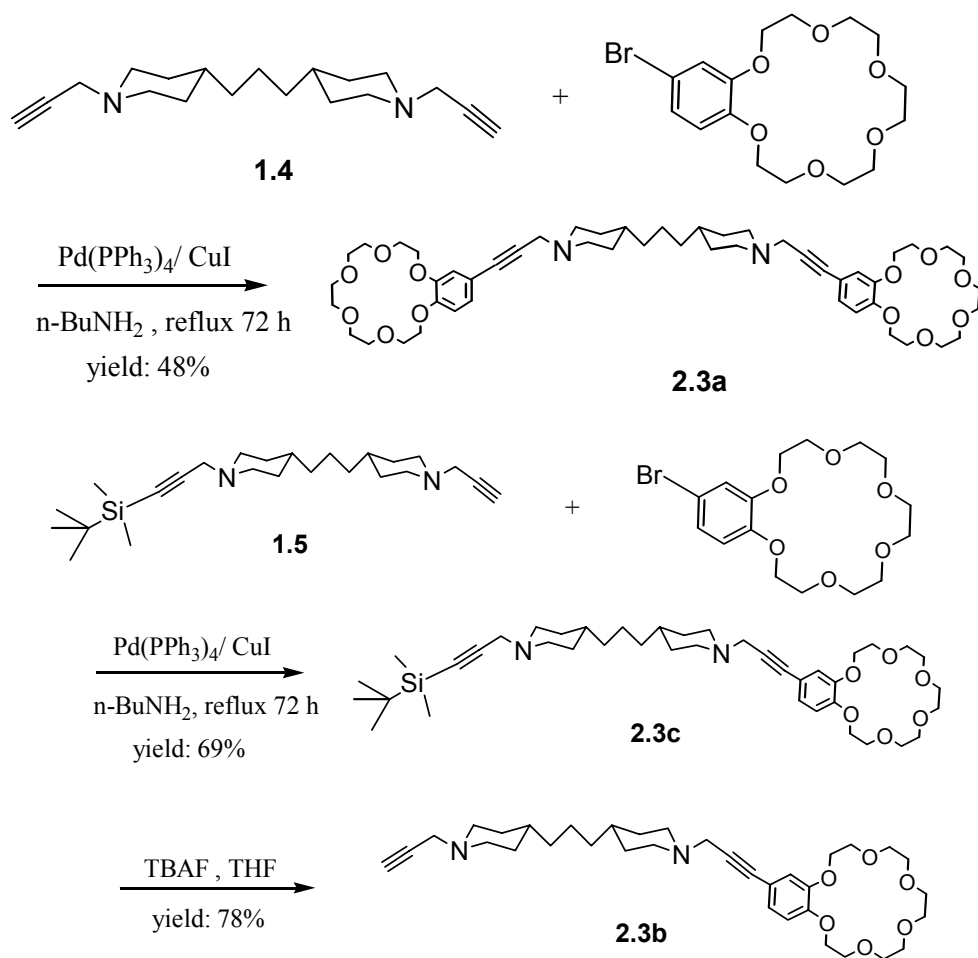
Figure 2.11. Synthesis of bipodal derivatives **2.3a**, **2.3b** and **2.3c**.

2.5.2 Synthesis of tripodal hosts 2.1 and 2.2

The synthetic route to the tripodal hosts **2.1** and **2.2** was outlined in **Figure 2.12**. The commercially available starting material 4,4'-trimethylenedipiperidine was protected with Boc dicarbonate to control reactivity at one end of the molecule, the resulted amine **2.26** was coupled with 1,3,5-tricarbonylchloride benzene to afford end-capped tris-amine **2.27**. The Boc-protected tris-amine **2.27** was then quantitatively deprotected with the use of a 50% v/v solution of TFA/CH₂Cl₂ for removal of the t-Boc protective group.

Subsequently, the terminal tris-amine **2.28** condensed in a facile manner with 4-carboxybenzo-18-crown-6 using HOBT (1-Hydroxybenzotriazole hydrate) and EDCI (1-(3-Dimethylaminopropyl)-3-ethylcarbodiimide hydrochloride) as activators yielded a good yield of triangular host **2.2**, followed by reduction of **2.2** with LiAlH$_4$ offered tripodal host **2.1**.

Figure 2.12. Synthesis of tripodal compounds **2.1** and **2.2**.

2.6 Conclusion

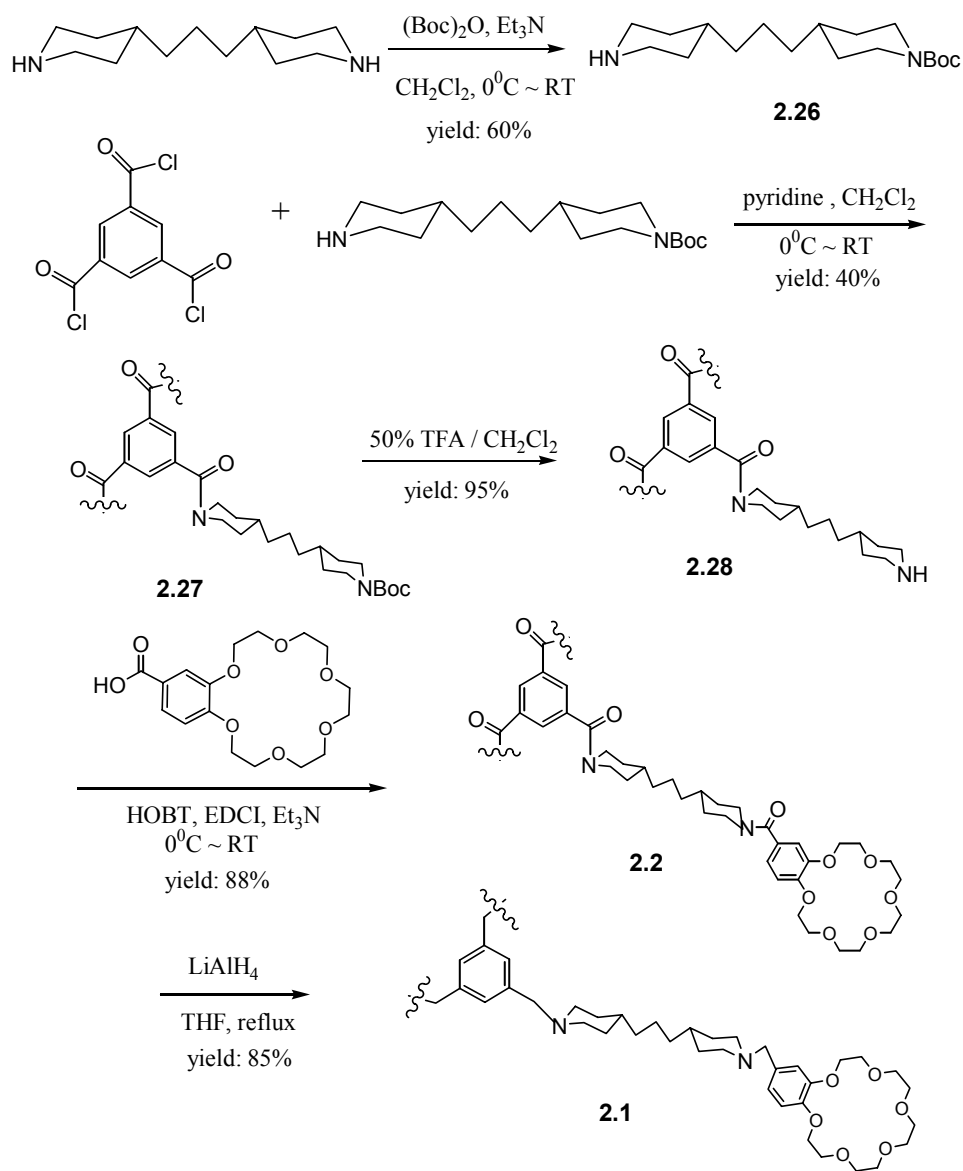We have successfully developed convenient and efficient protocols for the synthesis of bipodal derivatives **2.3** and tripodal tris-crown-ethers **2.1** and **2.2**. In the synthetic strategies there are derivatives on the way to the desired materials that allow us to tune the sizes and electronic properties of organic host molecules. The diamines **2.3a-2.3c** and tripodal structures **2.1** and **2.2** were less successful in trapping and stabilizing the keplerate solution species. Studies probed the relationship between the structure of the molecular host and the formation of nanostructures supported the speculation that the nanostructures were not only dependent on the native nature of Mo-POM solution state but also partially rely on complementarity between Mo-POM and molecular host. Studies with a chemically related Mo-POM, the giant wheel {Mo$_{154}$}, indicated that crystal growth dominated in the formation of Mo-containing nanostructures; the construction of nanoscopic features appeared to be a rough shell of molybdate instead of aggregates of stable nanoscopic building subunits such as {Mo$_{154}$} giant wheel. The evidences from the TEM surveys suggested that size/shape and electronic complementarity probably involved the properties of the inorganic clusters (guest) and organic segments (host). To date, there are very few studies exploring the properties of POMs functionalized with organic groups so the current work opens an exciting research territory.[42]

2.7 Experimental section

General Methods. All reactions were carried out under N_2 or Argon atmosphere. THF was pre-dried over CaH_2 and distilled from sodium and benzophenone. DMF was distilled from CaH_2 and stored over 4-Å molecular sieves under nitrogen. All the other reagents were used as received from commercial sources. ^{1}H NMR and ^{13}C NMR spectra were recorded at 400 MHz and 100MHz respectively.

2.3a.   *N,N'*-di-(2-propynyl)-4,4'-trimethylenedipiperidine **1.4** (0.329 g, 1.150 mmol) and 4'-bromobenzo-18-crown-6 (0.990 g, 2.530 mmol) was dissolved in 20 mL n-butylamine. The resulting solution was treated with $Pd(PPh_3)_4$ (87.7 mg, 0.0759 mmol) and CuI (22 mg, 0.116 mmol) and the solution was refluxed for 72 h. After cooling to r.t., the solvents were evaporated and the residue was extracted into $CHCl_3$, the organic phase was washed with water and brine and dried over $MgSO_4$. Column chromatography (gradient elution: EtOAc followed by 2-8% MeOH/$CHCl_3$) give a dark yellow oil (0.50 g, 48%) ^{1}H NMR (400 MHz, CDCl$_3$): δ 1.18-1.38 (m, 12H), 1.73 (d, 4H, J=11.5 Hz), 2.18-2.30 (t, 4H, J=11.5 Hz), 2.99 (d, 4H, J=11.5 Hz), 3.49 (s, 4H), 3.69 (s, 8H), 3.70-3.74 (m, 8H), 3.74-3.80 (m, 8H), 3.90-3.95 (m, 8H), 4.10-4.18 (m, 8H), 6.76 (dd(rough), 2H, J= 8.33 Hz), 6.97 (dd(rough), 2H, J= 2.05 Hz), 7.01 (dd(rough), 2H, J=2.05, 8.31 Hz). ^{13}C NMR (100 MHz, CDCl$_3$): δ 23.8, 32.1, 35.1, 36.6, 48.0, 52.9, 69.0, 69.2, 69.4, 69.5, 70.7, 70.8, 113.3, 115.3, 117.1, 123.9, 125.3, 148.4, 149.2. MALDI-TOF-MS: m/z 907 [M+H].

2.3c. *N*-(t-butyldimethylsilyl-2-propynyl)-*N'*-(2-propynyl)-4,4'-

trimethylenedipiperidine **1.5** (0.843 g, 2.1054 mmol) and 4'-bromobenzo-18-

crown-6 (0.906 g, 2.3155 mmol) was dissolved in 20 mL n-butylamine. The

resulting solution was treated with Pd(PPh$_3$)$_4$ (0.122 g, 0.1056 mmol) and CuI

(40.1 mg, 0.116 mmol) and the whole solution was refluxed for 72 h. After cooling

to r.t., the solvents were evaporated and the residue was extracted into CHCl$_3$,

the organic phase was washed with water and brine and dried over MgSO$_4$.

Column chromatography (gradient elution: 2-8% MeOH/CHCl$_3$) give a yellow oil

(1.03 g, 68.8%). ^{1}H NMR (400 MHz, CDCl$_3$): δ 0.10 (s, 6H), 0.94 (s, 9H), 1.19-

1.34 (m, 12H), 1.68-1.76 (m, 4H), 2.18-2.30 (m, 4H), 2.87 (d, 2H, J=11.4 Hz),

2.99 (d, 2H, J=11.4 Hz), 3.35 (s, 2H), 3.49 (s, 2H), 3.69 (s, 4H), 3.70-3.74 (m,

4H), 3.74-3.80 (m, 4H), 3.90-3.94 (m, 4H), 4.11-4.19 (m, 4H), 6.78 (d, 1H, J=8.25

Hz), 6.95 (d, 1H, J=1.88 Hz), 7.01 (dd, 1H, J=8.25, 1.88 Hz). ^{13}C NMR (100 MHz,

CDCl$_3$): δ –4.52, -4.51, 16.5, 23.9, 26.1, 32.1, 35.1, 36.56, 36.63, 48.1, 48.2,

52.4, 52.9, 69.0, 69.5, 70.7, 70.8, 113.3, 115.6, 117.0, 125.3, 148.4, 149.3.

MALDI-TOF-MS: m/z: 711 [M+H].

2.3b.   Compound **2.3c** (1.023 g, 1.439 mmol) in 25 mL THF at 0 °C, was

treated with TBAF (3.6 mL, 1 M, dropwise); the reaction mixture was stirred at 0

°C for 10 min, and then stirred at r.t. for another 4 h. After quenching with

NH$_4$Cl$_{(aq)}$, the reaction mixture was extracted into CHCl$_3$ and washed with water,

the organic phase was dried over MgSO$_4$. Column chromatography (gradient

elution: 3-8% MeOH/CHCl$_3$) yielded a light- yellow oil (0.67 g, 78%). ^{1}H NMR

(400 MHz, CDCl$_3$): δ 1.18-1.34 (m, 12H), 1.67-1.75 (m, 4H), 2.14-2.21 (m, 4H), 2.24 (t, 1H, J=2.42 Hz), 2.88 (d, 2H, J=11.5 Hz), 2.98 (d, 2H, J=11.5 Hz), 3.30 (d, 2H, J= 2.42 Hz), 3.49 (s, 2H), 3.69 (s, 4H), 3.70-3.74 (m, 4H), 3.75-3.79 (m, 4H), 3.90-3.95 (m, 4H), 4.12-4.16 (m, 4H), 6.78 (d, 1H, J=8.24 Hz), 6.95 (d, 1H, J=1.85 Hz), 7.01 (dd, 1H, J=8.24, 1.85 Hz). ^{13}C NMR (100 MHz, CDCl$_3$): δ 13.6, 20.2, 23.9, 32.3, 35.1, 35.2, 36.6, 47.2, 48.1, 52.6, 53.0, 69.0, 69.1, 69.5, 70.68, 70.70, 70.74, 70.9, 72.9, 113.4, 115.7, 117.1, 125.3, 148.4, 149.2. MALDI-TOF-MS: m/z: 597 [M+H], 619 [M+Na], 635 [M+K]. Anal. Calcd. for C$_{35}$H$_{52}$N$_2$O$_6$: C, 70.43; H, 8.78; N, 4.70. Found: C, 70.28; H, 8.80; N, 4.87.

2.26. To a cooled solution (0 °C) of 4,4'- trimethylenedipiperdine (5.390 g, 25.622 mmol) and Et$_3$N (3.6 mL) in 30 mL CH$_2$Cl$_2$, was added very slowly a solution of di-t-butyl dicarbonate (1.864 g, 8.541 mmol) in 25 mL CH$_2$Cl$_2$ over a period of 3 h. After addition, remove the ice-bath, the reaction mixture was stirred 24 h at r.t.. Then water (25 mL) and CH$_2$Cl$_2$ (25 mL) were added in order to dissolve the precipitate (the aqueous phase is an emulsion). After separation of the two phases, the organic phase was concentrated under reduced pressure and the residue was dissolved in ether (25 mL) and water (25 mL) (didn't dissolve totally, acidification makes it dissolve). The mixture was acidified to ~ pH 5 by 6N HCl, the bis-protected diamine was extracted with ether (3 X 30 mL). The left aqueous phase was adjusted to ~ pH 11 with 2M NaOH and extrated with EtOAc (6 X 30 mL). The combined organic phase was then dried over Na$_2$SO$_4$, filtered and removal of the solvent and dried in vacuo to yield a white

solid (1.58 g, 60% yield). Without further purification, the resulted white solid was directly used for next step. ^{1}H NMR (400 MHz, CDCl$_3$): δ 1.02-1.38 (m, 12H), 1.45 (s, 9H), 1.61-1.68 (m, 4H), 1.89 (m, 4H), 2.66 (t, 2H), 2.87 (s, 1H), 2.95 (roughly d, 1H), 3.08 (d, 1H). ^{13}C NMR (100 MHz, CDCl$_3$): δ 23.7, 28.4, 32.2, 32.3, 35.9, 36.2, 36.7, 36.8, 44.1, 52.5, 79.1, 155.0.

2.27. To a solution of **2.26** (2.0997 g, 6.762 g) in 30 mL CH$_2$Cl$_2$ cooled in an ice bath was added 1,3,5–benzotricarbonyl trichloride (0.561 g, 2.113 mmol). The reaction mixture was stirred overnight at r.t., after which 0.53 mL pyridine was added and stirring was continued for 2 h. CH$_2$Cl$_2$ (20 mL) was added and the mixture was washed with saturated brine and diluted aqueous HCl (0.5 M). The organic phase was dried over Na$_2$SO$_4$ and solvent was removed. Column chromatography (EtOAc) gave a colorless oil as title compound (0.92 g, 40% yield). ^{1}H NMR (400 MHz, CDCl$_3$): δ 1.02-1.38 (m, 36H), 1.45 (s, 27H), 1.60-1.84 (m, 16H), 2.66 (t, 6H, J=13.0 Hz), 2.75 (roughly t, 2H), 2.99 (roughly t, 2H), 3.69 (roughly d, 2H), 4.07 (d, 6H, J=13.0 Hz), 4.67 (roughly d, 2H), 7.45 (s, 3H). ^{13}C NMR (100 MHz, CDCl$_3$): δ 23.6, 28.5, 31.9, 32.2, 32.9, 35.9, 36.0, 36.5, 36.6, 42.7, 44.0, 48.2, 79.2, 126.4, 137.0, 154.9, 168.5. MALDI-TOF-MS: m/z: 1088 [M+H], 1110 [M+Na], 1126 [M+K].

2.28. Compound **2.27** (0.733 g, 0.674mmol) was dissolved in 3.8 mL 50% TFA/CH$_2$Cl$_2$ (v/v), the whole reaction mixture was stirred at r.t. overnight, then the mixture was diluted into CH$_2$Cl$_2$, washed with 5% NaOH aqueous solution,

saturated brine. The organic layer was dried over Na_2SO_4. After removal of the solvent, colorless oil was collected as product (0.505 g, 95% yield). Without further purification, the crude product was directly used for the next step. ^{1}H NMR (400 MHz, $CDCl_3$): δ 1.02-1.38 (m, 36H), 1.51 (m, 4H), 1.60-1.84 (m, 12H), 2.45 (bs, 3H), 2.63 (bs, 4H), 2.75 (roughly t, 4H, J=12.4 Hz), 3.00 (roughly t, 4H, J=12.4 Hz), 3.13 (bs, 4H), 3.69 (roughly d, 2H), 4.67 (roughly d, 2H), 7.45 (s, 3H). ^{13}C NMR (100 MHz, $CDCl_3$): δ 23.3, 31.9, 32.2, 32.8, 35.4, 35.9, 36.4, 36.7, 42.7, 45.8, 48.2, 126.4, 137.0, 168.5. MALDI-TOF-MS: m/z: 787.6 [M+H], 809.6 [M+Na], 825.6 [M+K].

2.2. HOBT (0.158 g, 1.169 mmol) and EDCI•HCl (0.225 g, 1.174 mmol) were added to a stirred solution of 4'-carboxy-benzo-18-crown-6 (0.38 g, 1.066 mmol) in CH_2Cl_2 (20 mL) at 0 °C under Argon. 20 min later, a solution of compound **2.28** (0.262 g, 0.333 mmol) in CH_2Cl_2 (5 mL) with Et_3N (0.14 mL) was added. The reaction mixture was stirred 24 h at r.t., and then washed with 0.5N HCl (2 X 25 mL), brine, 5% $NaHCO_3$ aqueous solution and brine. The organic layer was dried over Na_2SO_4 and evaporated to give colorless oil. Column chromatography (Alumina: 2 ~ 3% MeOH/$CHCl_3$) gave a colorless sticky oil as title compound (0.53 g, 88% yield). ^{1}H NMR (400 MHz, $CDCl_3$): δ 1.15-1.36 (m, 36H), 1.50 (m, 6H), 1.66-1.80 (m, 12H), 2.75-3.00 (m, 12H), 3.69 (s, 12H), 3.71-3.74 (m, 12H), 3.76-3.79 (m, 12H), 3.91-3.94 (m, 12H), 4.15-4.19 (m, 12H), 4.66 (bs, 6H), 6.85 (d, 3H), 6.95 (d, 2H, J=1.87 Hz), 6.96 (d, 4H, J=1.87 Hz), 7.45 (s, 3H). ^{13}C NMR (100 MHz, $CDCl_3$): δ 23.6, 31.9, 32.9, 36.0, 36.1, 36.4, 36.5, 42.7, 48.2, 69.0,

69.1, 69.4, 69.5, 70.64, 70.67, 70.70, 70.72, 70.8, 113.1, 113.2, 120.3, 126.4, 129.0, 137.0, 148.6, 150.0, 168.4, 170.1. MALDI-TOF-MS: m/z: 1803 [M+H], 1825 [M+Na], 1841 [M+K].

2.1. To a suspension of LiAlH$_4$ (0.126 g, 3.32 mmol) in dry THF 15 mL was added a solution of compound **2.2** (0.199 g, 0.11 mmol) in 5 mL THF dropwise at 0 °C under Argon. The mixture was refluxed for 24 h, then after cooling down the reaction mixture, 1 mL H$_2$O, 1 mL 5% NaOH aqueous solution and 2 mL H$_2$O was added sequentially. The resulted mixture was filtered and the filter cake was washed with THF. The combined filtrate and washings were evaporated and a light-yellow oil was collected. The crude product was separated by flash column chromatography (Alumina: 2% MeOH/CHCl$_3$) to afford a colorless oil (0.16 g, 85% yield). ^{1}H NMR (400 MHz, CDCl$_3$): δ 1.18-1.25 (m, 36H), 1.50-1.62 (d, 12H), 1.83-1.91 (m, 12H), 2.81-2.85 (m, 12H), 3.38 (s, 6H), 3.45 (s, 6H), 3.69 (s, 12H), 3.71-3.73 (m, 12H), 3.76-3.79 (m, 12H), 3.90-3.93 (m, 12H), 4.13-4.18 (m, 12H), 6.80 (s, 6H), 6.88 (s, 3H), 7.11 (s, 3H). ^{13}C NMR (100 MHz, CDCl$_3$): δ 23.9, 32.4, 35.7, 36.8, 53.9, 54.0, 63.1, 63.4, 69.1, 69.3, 69.7, 70.75, 70.81, 70.83, 113.9, 115.2, 121.9, 128.7, 131.9, 138.0, 147.9, 148.8. MALDI-TOF-MS: m/z: 1718 [M], 1719 [M+H], 1741 [M+Na].

References:

(1) Canceill, J.; Lacombe, L.; Collet, A. *J. Am. Chem. Soc.* **1986**, 108, 4230

(2) Cram, D. J.; Tanner, M. E.; Thomas, R. *Angew. Chem. Int. Ed. Engl.* **1991**, 30, 1024.

(3) Sherman, J. C.; Knobler, C. B.; Cram, D. J. *J. Am. Chem. Soc.* **1991**, 113, 2194.

(4) Edelmann, F. T. *Angew. Chem. Int. Ed. Engl.* **1995**, 34, 981.

(5) Bethune, D. S.; Johnson, R. D.; Salem, J. R.; de Vries, M. S.; Yannoni, C. S. *Nature* **1993**, 366, 123.

(6) Atwood, J. L.; Barbour, L. J.; Nichols, P. J.; Raston, C. L.; Sandoval, C. A. *Chem.-Eur. J* **1999**, 5, 990.

(7) Yanase, M.; Haino, T.; Fukazawa, Y. *Tetrahedron Lett.* **1999**, 40, 2781.

(8) Jenekhe, S. A.; Chen, X. L. *Science* **1998**, 279, 1903.

(9) Chen, X. L.; Jenekhe, S. A. *Langmuir* **1999**, 15, 8007.

(10) Douglas, T.; Young, M. *Nature* **1998**, 393, 152.

(11) Rebek, J. Jr. *Acc. Chem. Res.* **1999**, 32, 278.

(12) Wyler, R.; de Mendoza, J.; Rebek, J. Jr. *Angew. Chem. Int. Ed. Engl.* **1993**, 32, 1699.

(13) Branda, N.; Wyler, R.; Rebek, J. Jr. *Science* **1994**, 263, 1267.

(14) Branda, N.; Grotzfeld, R. M.; Valdes, C.; Rebek, J. Jr. *J. Am. Chem. Soc.* **1995**, 117, 85.

(15) Meissner, R. S.; de Mendoza, J.; Rebek, J. Jr. *Science* **1995**, 270, 1485.

(16) Kang, J.; Rebek, J. Jr. Nature 1996, 382, 239.

(17) MacGillivray, L. R.; Atwood, J. L. *Nature* **1997**, 389, 469.

(18) Heinz, T.; Rudkevich, D. M.; Rebek, J. Jr. *Nature* **1998**, 394, 764.

(19) Luetzen, A.; Renslo, A. R.; Schalley, C. A.; O'leary, B. M.; Rebek, J. Jr. *J. Am. Chem. Soc.* **1999**, 121, 7455.

(20) Day, A.; Blanch, R. J.; Arnold, A. P.; Lorenzo, S.; Lewis, G. R.; Dance, I. *Angew. Chem. Int. Ed. Engl.* **2002**, 41, 275.

(21) MacGillivray, L. R.; Atwood, J. L. *Angew. Chem. Int. Ed.* **1999**, *38*, 1018.

(22) Fujita, M.; Umemoto, K.; Yoshimura, M.; Fujita, N.; Kusukawa, T.; Biradha, K. *Chem. Commun.* **2001**, 509.

(23) Umemoto, K.; Yamaguchi, K.; Fujita, M. *J. Am. Chem. Soc.* **2000**, 122, 7150.

(24) Chand, D. K.; Biradha, K.; Fujita, M.; Sakamoto, S.; Yamaguchi, K. *Chem. Commun.* **2002**, 2486.

(25) Olenyuk, B.; Whiteford, J. A.; Fechtenkötter, Stang, P. J. *Nature* **1999**, 796.

(26) Caulder, D. L.; Powers, R. E.; Parac, T. N.; Raymond, K. N. *Angew. Chem. Int. Ed. Engl.* **1998**, 37, 1840.

(27) Parac, T. N.; Caulder, D. L.; Raymond, K. N. *J. Am. Chem. Soc.* **1998**, 120, 8003.

(28) Orr, G. W.; Barbour, J.; Atwood, J. L. *Science* **1999**, 285, 1049.

(29) Zhong, Z.; Ikeda, A.; Ayabe, M.; Shinkai, S.; Sakamoto, S.; Yamaguchi, K. *J. Org. Chem.* **2001**, 66, 1002.

(30) Levine, A.J. *Viruses*, W. H. Freeman, New York, **1992**

(31) Caspar, D. L. D.; Klug, A. *Cold Spring Harbor Symp. Quant. Biol.* **1962**, 27, 1.

(32) Schneler, C.; Caruso, F. *Biomacromolecules* **2001**, 2, 921.

(33) Dubuis, M.; Deme, B.; Culik-Krzywichi, T.; Dedieu, J-C.; Vautrin, C.; Desert, S.; Perez, E.; Zemb, T. *Nature* **2001**, 411, 672.

(34) Pope, M. T.; *Heterpooly and Isopoly Oxometalates*; Springer-verlag: New York, **1983**.

(35) Faul, C. F. J.; Antonietti, M. *Adv. Mater*, **2003**, 15, 673-683.

(36) Müller, A.; Koop, M.; Bogge, H.; Schmidtmann, M.; Beugholt, C. *J. Chem. Soc. Chem. Comm.* **1998**, 1501.

(37) Sharma, C. V. K.; Clearfield, A. *J. Am. Chem. Soc.* **2000**, *122*, 1558.

(38) Müller, A.; Krickemeyer, E.; Bögge, H.; Schmidtmann, M.; Peters, F. *Angew. Chem. Int. Ed.* **1998**, *37*, 3360.

(39) Müller, A.; Diemann, E.; Kuhlmann, C.; Eimer, W.; Serain, C.; Tak, T.; Knöchel, A.; Pranzas, P. K. *Chem. Comm.* **2001**, 1928.

(40) Müller, A.; Krickemeyer, E.; Meyer, J.; Bögge, H.; Peters, F.; Plass, W.; Diemann, E.; Dillinger, S.; Nonnenbruch, F.; Randerath, M.; Menke, C. *Angew. Chem. Int. Ed.* **1995**, 34, 2122.

(41) Petroski, J. M.; Green, T. C.; El-sayed, M. A. *J. Phys. Chem. A.* **2001**, 105, 5542-5547.

(42) Rhule, J. T.; Hill, C. L.; Judd, D. A.; Schinazi, R. F. *Chem. Rev.* **1998**, 98, 327.

Chapter 3

Dynamic Behavior/Evolution of Nanoscale Solution-state Species in Partially Reduced Polyoxomolybdate Solution

An unusual combination of analytical protocols has been used to study the solution-phase growth of a partially reduced Mo-POM. The evolution of Mo-POM nanoscopic features over the course of weeks was monitored by flow field-flow fractionation and corroborated by electron microscopy (Transmission and Scanning). Unusual, polydisperse size distributions of nanostructures were observed in the flow field-flow fractionation (FlFFF) and TEM measurements. Total Mo content in the solution and precipitate phases was followed off-line by inductively coupled plasma-optical emission spectroscopy (ICP-OES). During the self-assembling process of Mo-POM, we observed crystallization-driven formation of keplerate $\{Mo_{132}\}$ and solution-phase-driven evolution of structurally related nanoscopic species (3 ~ 75 nm).

3.1 Introduction

The mystery of molybdenum blue solutions has attracted scientists' attentions for over two centuries. Structural details of molybdenum blue solutions have been elucidated in only recent years by the solid state studies of Müller and co-workers.[1,2] However, the solid state studies were limited to the nature of the

well-ordered crystals which were isolated from the solution; isolated species frequently have little to do with what are present in solution state. The characterization of complicated polydisperse Mo-POM is a challenging task; it is particularly difficult to determine which species are present and which species are more stable in molybdenum blue solutions. Ensemble analytical techniques such as dynamic light scattering (DLS) can measure the averages of size distributions whereas non-ensemble techniques such as electron microscopy can highlight the properties of individual structures such as particle morphology and composition.[3] DLS techniques have been applied in studies of Mo-POM solution states; one study showed that in polar solvents, species in Mo-POM presented a distribution of aggregates instead of single anions.[4] Similar results were obtained for a chemically related Mo-POM aqueous system.[5] In that study, the structures of the uniformly large aggregates have been demonstrated to be vesicular. However, such techniques are not compatible with the Mo-POM under current study because its high absorbance precludes their use.[6] Therefore a different analytical protocol is necessary to separate and characterize nanoscopic components in Mo-POM solution state. The versatile high-resolution separation technique, field-flow fractionation (FFF), is a good choice.

FFF is an elution-based, chromatography-like separation and sizing technique uniquely capable of separating materials within a wide size range (1 nm to 100 μm).[7,8] The main difference between FFF and chromatography is that in FFF, separation is conducted in a thin, unpacked open channel instead of in a column filled with packing agents. Unlike the many kinds of chromatographies

that are based on exclusion or adsorption, FFF functions solely by physicochemical interactions with an external field perpendicular to the flow. The nature of the external field gives rise to different FFF sub-techniques. Currently, the common FFF sub-techniques are flow,[9,10] sedimentation,[11,12] thermal,[13,14] electrical[15,16] and magnetic FFF.[17] Among the members of the FFF family, flow field-flow fractionation (FlFFF) is the most versatile technique tested so far.[7,8] FlFFF has wide applications in biomedicine, environmental science, and industry.[18-22]

However, the use of FFF to separate inorganic clusters has not been reported so far. Certainly no time-dependent chemistries have been elucidated with any FFF technique. These facts make the current work unique. In this study, we assessed the feasibility of FlFFF for the separation and characterization of partially reduced polyoxomolybdate species chemically related to keplerate $\{Mo_{132}\}$. Material redissolved from the crystallization-driven preparation of keplerate $\{Mo_{132}\}$ and material from the mother liquor was used in the study.

3.2 Theory

3.2.1 Flow field-flow fractionation

Conventional FFF separation occurs in a thin, ribbon-like, open channel. The sample is introduced into the channel by a carrier fluid. The channel flow rate is controlled so that a parabolic flow profile is achieved in which the maximum flow velocity occurs at the center of the channel. In FlFFF, a cross-flow of fluid functions as the external field. This cross-flow fluid is applied

79

perpendicularly to the channel flow, driving the sample towards the accumulation wall while different diffusion rates of sample components move them away from the wall (**Figure 3.1**). Since each component has different diffusion coefficients and interacts differently with the external field, the components of the same size are retained at similar transverse positions across the channel and are eluted at different times. In the normal mode of FFF separation, d < 1 µm, small particles elute faster than larger particles. However, for particles with d > 1 µm, the steric/hyperlayer mode prevails in separation and larger particles elute faster.[23] Since the polydisperse Mo-POM in this study had d < 1 µm, the normal mode of separation is active.

Channel Flow in   External Field   Channel Flow out

(A)

(B)

Accumulation Wall
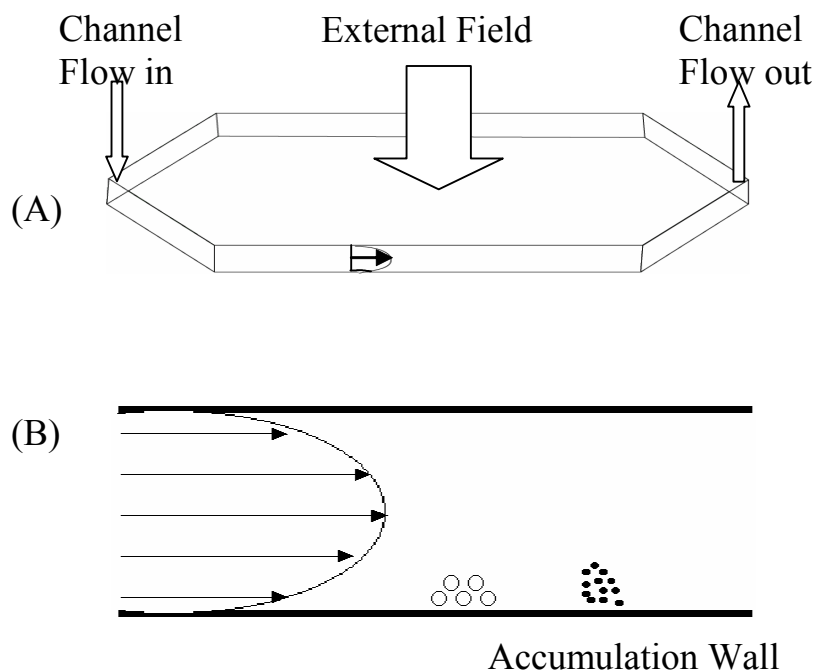
Figure 3.1. (**A**) Schematic representation of FlFFF channel. (**B**) Exploded view of channel (normal mode).

The theory of FFF has been detailed elsewhere;[7, 24-26] the basic principles are described briefly. In FFF measurements, the retention of a sample component is expressed as the retention ratio R ($R = t^0/t_r = V^0/V_r$); t^0 is the retention time of void peak; t_r is the retention time of sample component; V^0 is the geometric volume of the channel while V_r is the elution volume of sample component.

The interaction of sample with the external field is best defined by the retention parameter λ, which can be related to R:

$$R = 6\lambda \left(\coth\left(\frac{1}{2\lambda}\right) - 2\lambda \right)$$
(**3.1**)

In FlFFF, λ is defined for each component by the following equation:

$$\lambda = \frac{V^0 D}{V_c \cdot w^2}$$
(**3.2**)

where w is the channel thickness, V_c is the volumetric cross-flow rate and D is the component's diffusion coefficient. Under a given set of conditions, the parameters V^0, V_c and w are constant, t_r and V_r can be directly measured from experiments and thus λ can be calculated from R. Therefore the diffusion coefficient D can be determined by eq. **3.2**. From the Stokes–Einstein equation, we can derive the relation between the particle diameter d and the diffusion coefficient D, which is expressed as:

$$d = \frac{kT}{3\pi\eta D}$$
(**3.3**)

here k is Boltzmann constant, T is the absolute temperature and η is viscosity. Diffusion coefficient and particle diameter are two parameters can be provided by FFF measurements.

3.2.2. Fractograms and particle size distributions

The raw data from FIFFF experiment is a plot of UV signal *versus* elution time or elution volume, which is called as a fractogram. The equivalent spherical particle diameter at any given elution time or volume can be calculated as aforementioned. Provided that the UV detector response, which is designated UV_i at point i along the elution profile, is proportional to the particle mass concentration in the flow streamline (dm^c_i/dV_i), a particle size distribution (dm^c_i/dd_i) can be converted from the UV fractogram based on the following equation:[21]

$$\frac{dm^c_i}{dd_i} = \frac{dm^c_i}{dV_i} \cdot \frac{dV_i}{dd_i} \propto UV_i \cdot \frac{dV_i}{dd_i} \qquad\qquad (3.4)$$

where m^c_i is the cumulative mass of the sample eluted up to elution volume V_i; d_i is the particle diameter fractionating at V_i and dd_i is the increment in d_i corresponding to dV_i increment in V at point i along the fractogram. The quantity dV_i / dd_i can be calculated with the FIFFF theory indicated above. The superscript c in the equation emphasizes the cumulative amount eluted up to point i on the fractogram.

3.2.3. Mo content distributions

If the FIFFF fractions are fed into an ICP-OES instrument, for element Mo, the mass concentration in the eluent (dm^c_{Moi}/dV_i) can be determined by calibration with standard solutions; thus a Mo-based particle size distribution can be determined by equation **3.5**:[21]

$$\frac{dm^c{}_{Mo_i}}{dd_i} = \frac{dm^c{}_{Mo_i}}{dV_i} \cdot \frac{dV_i}{dd_i} \qquad \textbf{(3.5)}$$

where m^c_{Moi} is the cumulative mass of element Mo eluted up to point i on the fractogram; the Mo-based particle size distribution is obtained by plotting dm^c_{Moi}/dd_i against particle diameter d.

3.2.4. Mo concentrations in particles

The distribution of element Mo mass per unit of particle mass at any point i along the elution time or volume axis is calculated as follows:[21]

$$\frac{dm^c{}_{Mo_i}}{dm^c{}_i} = \left[\left(\frac{dm^c{}_{Mo_i}}{dV_i} \right) \middle/ \left(\frac{dm^c{}_i}{dV_i} \right) \right] \propto \left(\frac{dm^c{}_{Mo_i}}{dV_i} \right) \middle/ UV_i \quad \textbf{(3.6)}$$

here dm^c_{Moi}/dV_i is the Mo concentration in the eluent and is determined by ICP analysis; UV_i is the UV response at elution volume V_i. This calculation is based on the assumption that the mass concentration of particles in the eluent is proportional to the UV signal.

3.2.5 Surface density distributions of Mo

The amount of Mo on the particle surface can be described as surface density distribution, which is a plot of the amount of Mo per unit particle surface area ($dm^c_{Mo_i}/dA^c_i$) as a function of particle size. The surface density of Mo can be determined as follows based on the assumption that a constant spherical shape (single-layer) and density present for the particles:[21]

$$\frac{dm^c_{Mo_i}}{dA^c_i} = \left[\left(\frac{dm^c_{Mo_i}}{dm^c_i} \right) \times \left(\frac{\delta m^c_i}{\delta A^c_i} \right) \right] \propto \left[\left(\frac{dm^c_{Mo_i}}{dV_i} \right) \middle/ UV_i \right] \times d_i \quad \textbf{(3.7)}$$

3.3 Particle sizing and characterization of redissolved keplerate {Mo$_{132}$} solution by FlFFF

Chapter 1 describes the development of a protocol for the kinetic precipitation of Mo-POM with *de novo* chelating agents and makes the argument that with tripodal **1.1** the distributions of particle sizes and the particle morphologies revealed by TEM generated repeatable snap shots of dynamic equilibrium of Mo-POM in solution. To apply such techniques, the phase transition needs to occur faster than structural rearrangement in solution. Although definitive evidences for kinetic precipitation has been shown in **chapter 1**, elucidation of the nature of keplerate {Mo$_{132}$} solution structures could benefit from a time-dependent assay. Here we applied time-dependent FlFFF technique to fractionate and characterize the keplerate {Mo$_{132}$} background solution. The aqueous keplerate {Mo$_{132}$} solution was prepared exactly the same as that used in the precipitation experiments by dissolving 3 mg keplerate {Mo$_{132}$} solid in 2 ml

deionized water. Since Mo^{VI}/Mo^{V} mixed valence has a characteristic absorption at 455 nm, the particle sizing of Mo-POM nanoscopic components was monitored at 455 nm.

Figure 3.2A shows the FlFFF fractograms of homogeneous keplerate $\{Mo_{132}\}$ solution as a function of time on the scale of days. Surprisingly, freshly prepared keplerate $\{Mo_{132}\}$ solution fractionated into a trimodal distribution of sizes instead of eluting as one uniform peak. Provided that the UV response is proportional to the particle mass concentration in the FlFFF stream, the size distribution of each fraction can be calculated from the UV fractogram based on the equation **3.4**. As shown in **Figure 3.2B**, the aqueous keplerate $\{Mo_{132}\}$ has three distinct size distributions.

In **Figure 3.2B**, the particles with average diameter of approximately 3 nm corresponded clearly to the single keplerate molecules. At this scale material with strong absorbance at 455 nm and UV-transparent material were observed. The second and third size distributions, with average diameter of 8 and 18 nm respectively, could have contributed to self-assembled aggregates from keplerate building blocks. The FlFFF measurements on the same solution after different days indicated significant changes on the contribution from each fraction.

A time-dependent decrease in the population of single keplerate molecules with concomitant formation of larger aggregates was observed. More interestingly, the maximum particle size of the largest aggregate increased by ~2-3 nm per day over the period of monitoring.
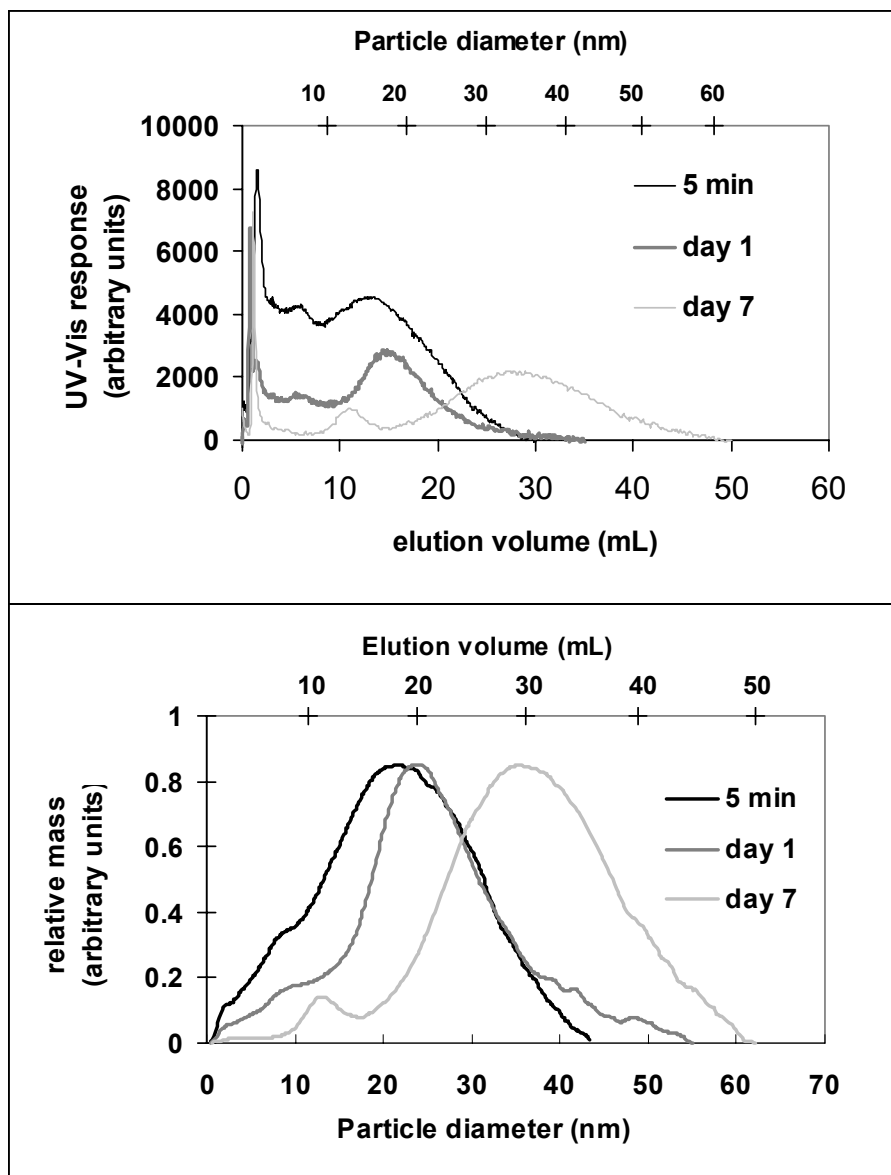
Figure 3.2. (**A**) FIFFF fractograms of redissolved keplerate $\{Mo_{132}\}$ aqueous solution. (**B**) Particle size distributions of redissolved keplerate $\{Mo_{132}\}$ solution (Step **D** in page 2: **Figure 1.1**). FIFFF experimental conditions: cross-flow rate = 3.00 mL/min; channel flow rate = 0.5 mL/min.

In order to gain more information about the unusual solution-state behavior of redissolved aqueous keplerate $\{Mo_{132}\}$, the FlFFF cross-flow rate was decreased; similar results were obtained as showed in **Figure 3.3**. The slow assembly process observed in this study is in accordance with the results of chemically related Mo-POMs reported by Müller and Liu respectively.[4,5]
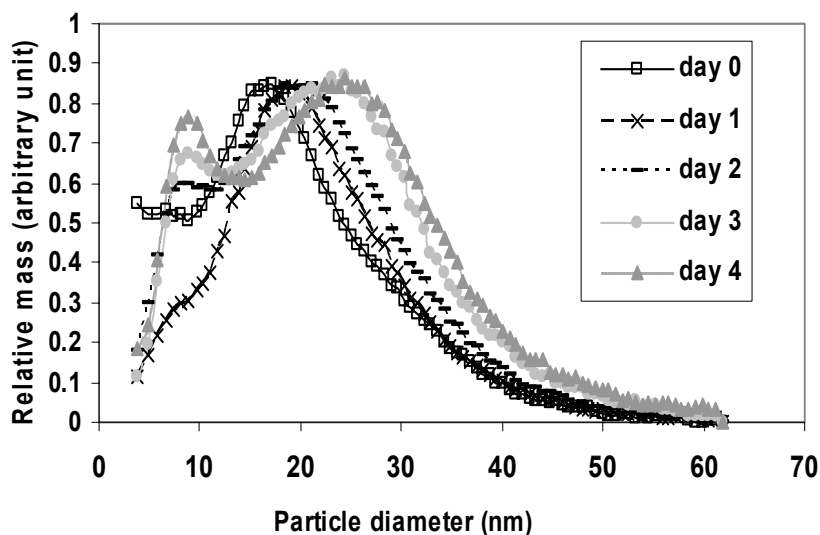
Figure 3.3. Particle size distributions of keplerate $\{Mo_{132}\}$ aqueous solution over the time (Step **D** in page 2: **Figure 1.1**). FlFFF experimental conditions: cross-flow rate = 0.77 mL/min; channel flow rate = 0.5 mL/min. Calculation based on equation **3.4**.

FlFFF measurements applied to the keplerate $\{Mo_{132}\}$ solution state gave similar results as kinetic precipitation with tripodal **1.1** described in **Chapter 1**. The size regime early in the dissolution of keplerate $\{Mo_{132}\}$ found in the FlFFF distributions approximated the features present in the transmission electron micrographs of the coprecipitate. These experiments lead to the conclusion that

Mo-POM solution-state structure is not at equilibrium upon dissolution of keplerate $\{Mo_{132}\}$. Evolution toward nanoscopic species requires days. These facts directly support the hypothesis that tripodal **1.1** kinetically trapped polydisperse aqueous Mo-POM before any structural deviations from the solution state occurred.

3.4 Separation and characterization of Mo-POM mother liquor by FlFFF

By FlFFF, solution phase Mo-POM anionic species slowly and continuously self-assembled into large aggregates (r~3-35 nm). The aforementioned crystalline keplerate $\{Mo_{132}\}$ is only the species isolated from partially reduced Mo-POM. The formation of this material is likely driven by favorable interactions in the cubic crystal lattice. The dynamic behavior of the solution state species is more complicated. To unveil the long-term mystery of the aqueous behavior of polymeric polyoxomolybdate in more details, we focused on the Mo-POM mother liquor of the preparation of keplerate $\{Mo_{132}\}$.

The Mo-POM mother liquor was prepared as published procedure.[1] To allow the system to come to a stable state, we did not make any attempts to filter solids from the solution. Samples from the mother liquor were subjected to FlFFF and TEM measurements at different reaction times. **Figure 3.4** shows the UV fractograms of Mo-POM mother liquor. Apparently three fractions can be observed in the fractograms. Since the intensity of UV/Vis signal is proportional to the particle mass concentration in the eluent, it is reasonable to assume that the intensity of UV/Vis signal reflects the mass content from each fraction. Time-

dependent studies of these fractograms indicated that structural evolution of Mo-POM species presented in solution.
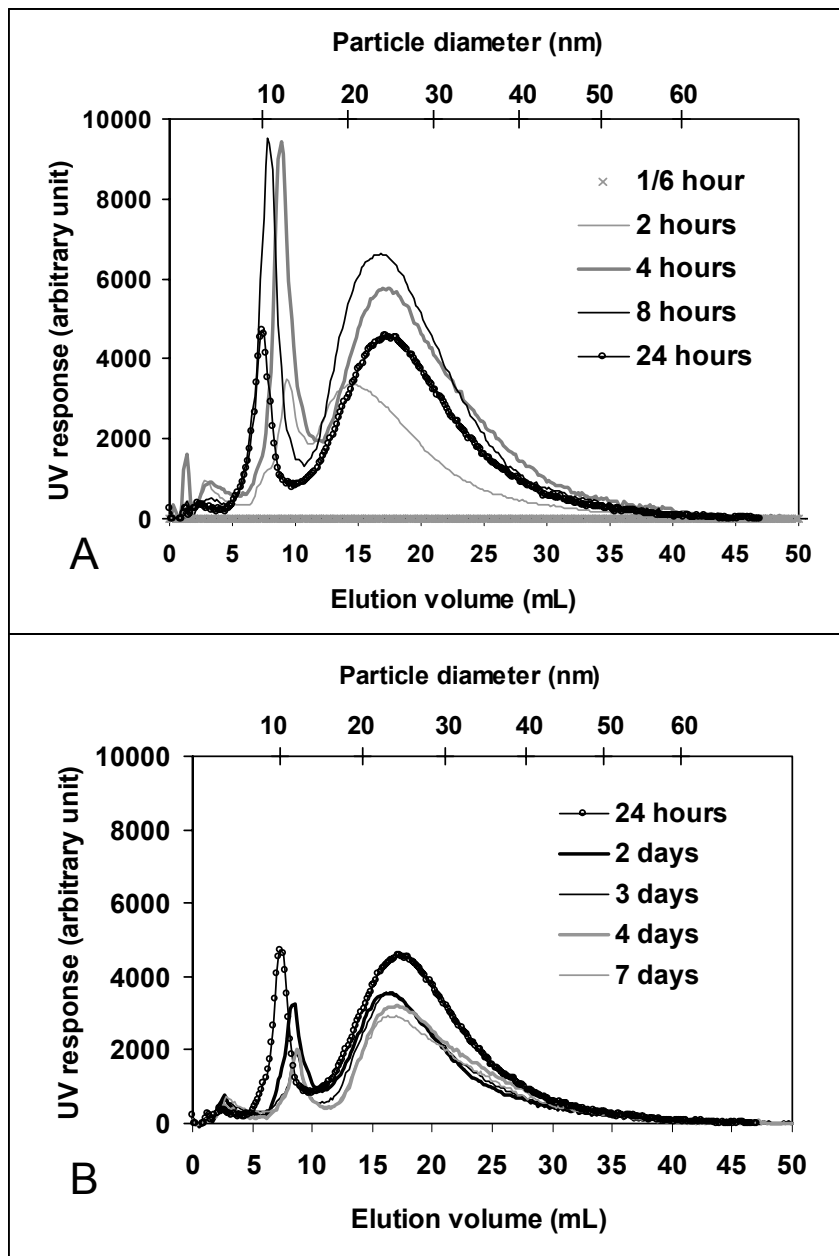
Figure 3.4. FIFFF fractograms of Mo-POM mother liquor with various reaction times (Step **F** in page 2: **Figure 1.1**).

The signal intensity from the solution phase of the published preparation (about 10 minutes after the initiation of the reaction) was very weak, indicating no Mo^V/Mo^{VI} mixed valent material and therefore no keplerate $\{Mo_{132}\}$. Upon standing, the solution phase of the keplerate $\{Mo_{132}\}$ preparation darkened to opaque brown. The UV/Vis signal also increased with time. After ~8 h, the UV/Vis signal was most intense; subsequently the UV/Vis absorbance decreased over two days presumably due to the precipitation of keplerate $\{Mo_{132}\}$. After two days, the UV/Vis response continued to decrease but obviously at a slower rate. In the fractogram, after initiation of the reaction, the fraction assigned to keplerate $\{Mo_{132}\}$ decreased within several hours followed by concomitant evolution of larger particles at d > 10 nm; see **Figure 3.4**. The rates of both particle formation and crystallization slowed down after two days.

Under the given FlFFF experimental conditions (see experimental section), particles with diameter of ~3 t0 75 nm were detected and polydisperse size distributions were observed (**Figure 3.5**). The maximum for each distribution migrated a little with a narrow range: 3.2 ± 0.3 nm, 11.5 ± 1.2 nm, and 25.0 ± 3.0 nm respectively. Although the relative mass of the first peak in the size distribution was very low, the corresponding peak appeared in the fractogram consistently over the period of monitoring. One important thing should be mentioned is that the size of the three populations in the mother liquor of the preparation of keplerate $\{Mo_{132}\}$ did not change significantly over 7 days. This was the major difference from the redissolved dilute keplerate $\{Mo_{132}\}$ solution. The results indicate that the nanoscopic species are thermodynamically stable

after they form in aqueous solution even when they are continuously washed by both channel-flow and cross-flow fluids during an FIFFF run.
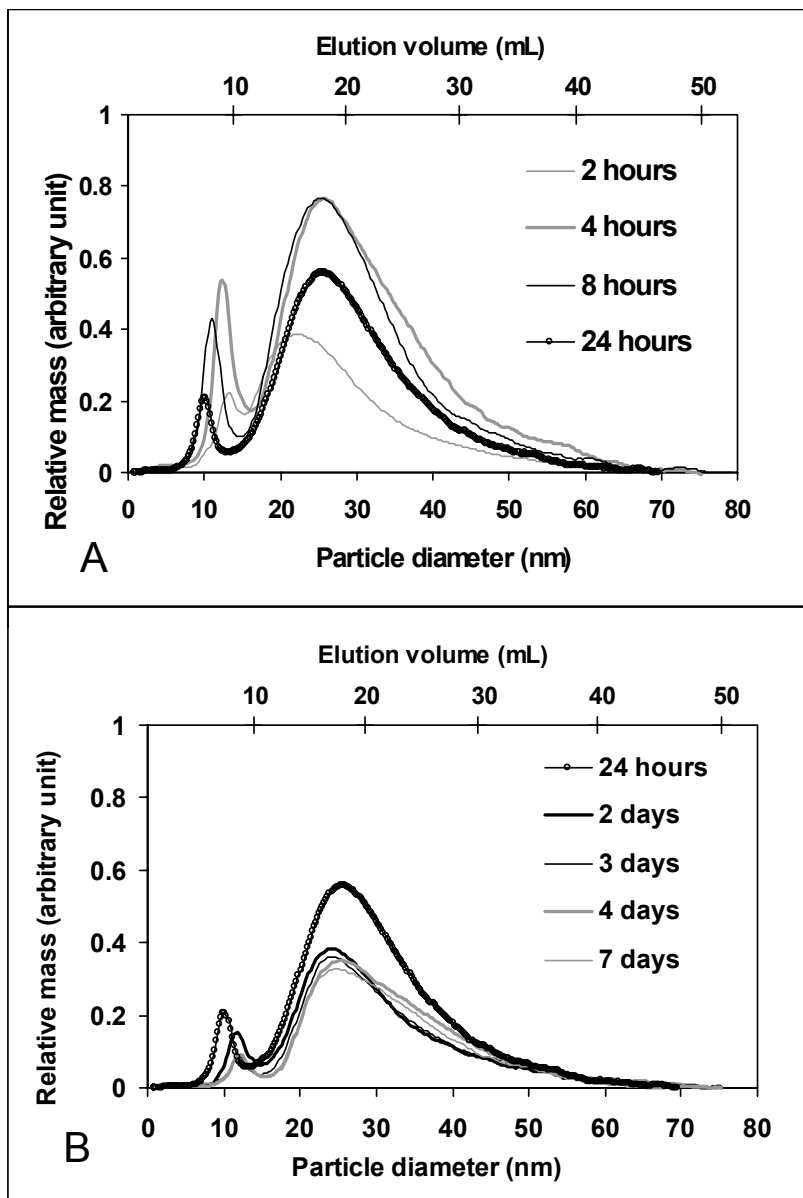
Figure 3.5. Particle mass-based size distributions of Mo-POM mother liquor with various reaction times (Step **F** in page 2: **Figure 1.1**). The corresponding size distribution of each fraction was determined directly from UV fractograms.

The Mo concentration of the mother liquor was monitored by inductively coupled plasma-optical emission spectroscopy (ICP-OES).[28] The results showed that the total $Mo_{(aq)}$ dramatically decreased within the first two days followed by a period of slow decrease after day two, indicating a continuous formation of crystalline keplerate $\{Mo_{132}\}$ (**Figure 3.6A**). After day 30, no detectable change can be determined.
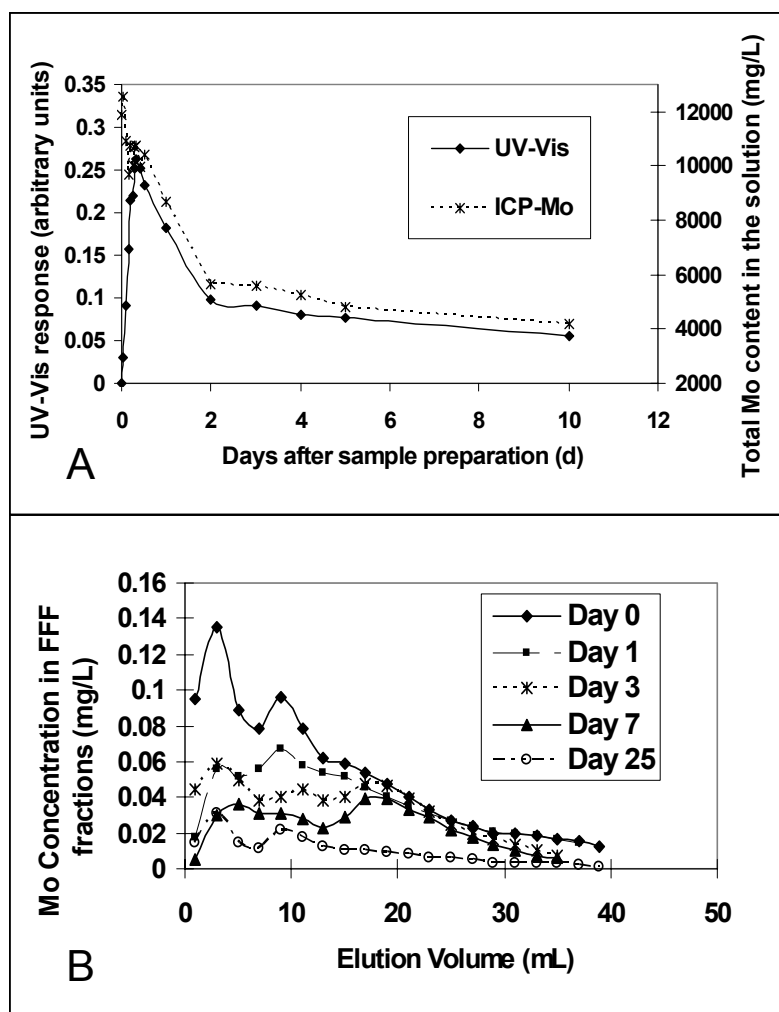
Figure 3.6. (**A**) Time-dependent Mo-concentrations in Mo-POM mother liquor; (**B**) Time-dependent Mo concentrations in eluting fractions (Step **G** in page 2: **Figure 1.1**).

Furthermore, from monitoring the UV/Vis absorption and total Mo content in the solution simultaneously, the UV/Vis detector signals change were coincident with the total Mo by ICP analyses. For some samples, the fractions eluting from FIFFF were collected and Mo compositions were determined off-line by ICP-OES. As shown in **Figure 3.6B,** it is apparent that Mo concentrations in the eluent also decreased continuously over the course of monitoring. **Figure 3.7** presents a clearer picture of the relationship between the ICP Mo distribution and particle mass distribution. The result showed that the Mo mass distribution was not in accordance with the particle mass distribution; higher Mo density was observed for small particles whereas the Mo density decreased for large particles. This indicated that the Mo contents in the particles were not uniform.
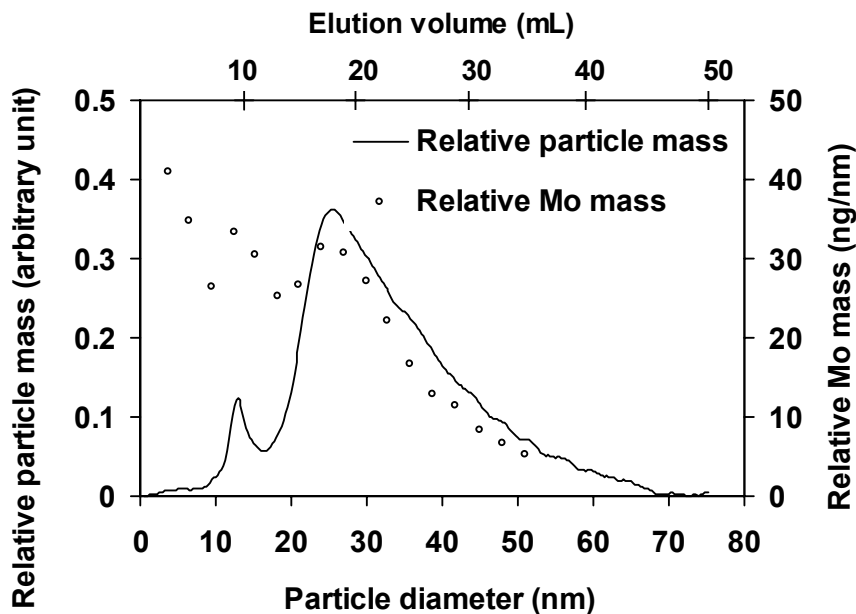
Figure 3.7. Particle mass-based and Mo-based size distributions of Mo-POM mother liquor (Step **G** in page 2: **Figure 1.1**). Calculation of relative Mo mass based on equation **3.5**.

93

There is a possibility that some Mo mass was in the form of large particles too large to be detected by current FlFFF experimental conditions. The hypothesis was tested by slowing down the FlFFF cross-flow rate (V_c) to optimize for measurements of large particles (100 nm to up). Under the FlFFF conditions which generally can sort particles up to 500 nm, no significant contribution from large particles (100 nm and up) was observed in UV fractograms.

Another hypothesis suggests that some large particles may decompose and convert back to UV/Vis–undetectable solution state. This hypothesis was tested by monitoring the UV/Vis absorption and total Mo content in the solution simultaneously (**Figure 3.6A**). The results showed that the UV/Vis response reflected the ICP Mo concentration throughout the reaction. Therefore the particles did not revert to UV-transparent material. Adhesion to the FlFFF membrane during elution could account for "missing Mo." To evaluate how much Mo was recovered after elution, the total Mo of the whole eluted solvent of a fractogram was determined by ICP-OES and compared to the total Mo introduced at the initiation of the FlFFF run. The absolute recovery of the sample was ~80%. This is a typically recovery for an FlFFF run.

To obtain more information about the distribution of Mo in the particles, the Mo concentration was plotted per unit particle mass against the particle diameter (**Figure 3.8**). Based on equation **3.6**, the ratio of the Mo concentration in the eluent to the UV detector is directly related to the composition of Mo in the particles. It is reasonable to assume that Mo per unit of particle mass should be same over the particle size range if the particles are solid.

Figure 3.8 also shows the corresponding surface density distribution of Mo, calculated by assuming the particles are spherical and composed of only a single layer at the surface. The Mo surface density distribution should remain constant *versus* the particle size distribution if the particles are hollow and single layer is contained.
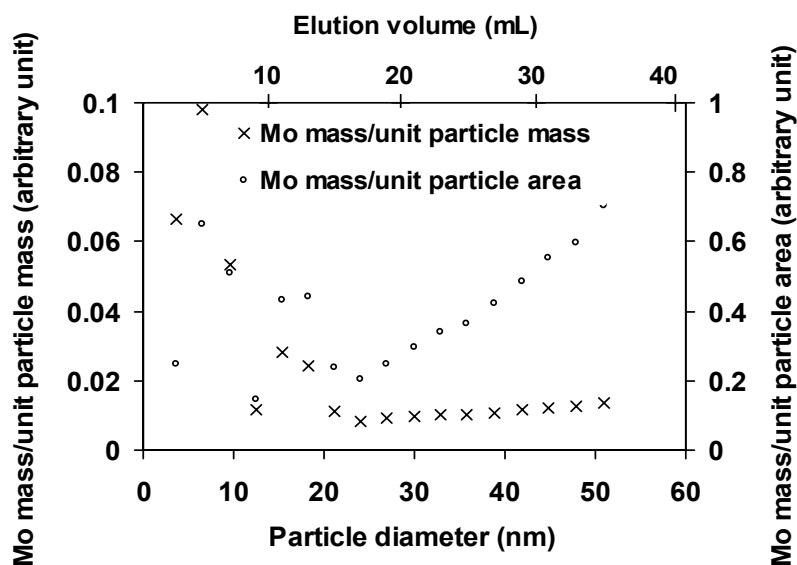

Figure 3.8. Mo content distributions in the particles (Step **G** in page 2: **Figure 1.1**). Calculation of Mo mass per unit particle mass based on equation **3.6**; Determination of Mo mass per unit particle surface area based on equation **3.7**.

It is noteworthy that the Mo concentration maxima of both curves in **Figure 3.8**, coincided in the smallest particles with diameter of about 3 nm. This observation strongly supported the speculation that the smallest particles were denser than larger particles. Initially Mo content substantially decreased as particle size increased from 3 to 25 nm. More remarkably, the minimum of both

curves was observed at diameter of approximately 25 nm, suggesting that denser aggregates of keplerate building blocks were formed below 25 nm and that particles probably organize into thin vesicles or less dense particles at around 25 nm. Between particle diameters 25-52 nm, Mo mass per unit particle mass increased slightly.

The Mo mass per unit of particle surface area increased dramatically within the particle diameter range of 25-52 nm. The non-constant distribution of Mo mass per unit particle surface area suggested that the particles in the mother liquor were not simply aggregated in a single layer of Mo-POM spheres. Particles of diameter 25 nm were most probably vesicular.

3.5 TEM study of keplerate {Mo$_{132}$} mother liquor

The TEM results were consistent with FIFFF results (**Figure 3.9**). Typically the particles sizes with diameters of approximately 7 to 75 nm were imaged in the micrographs. The individual keplerate molecules with diameters of ~3 nm were invisible; probably they merged with the granularity of the micrographs and disappeared in the background. The morphology of the Mo-POM is continuous with morphologies of keplerate {Mo$_{132}$} and **ppt1.1**. More remarkably some micrographs showed nanoscopic features (**Figure 3.9** day 2) diffracted in a homologous manner throughout the entirety of the features and were probably representative of the formation of a smooth, continuous shell of molybdate at the molecular level. These patterns are called moiré patterns which are caused by overlapping lattices.

96
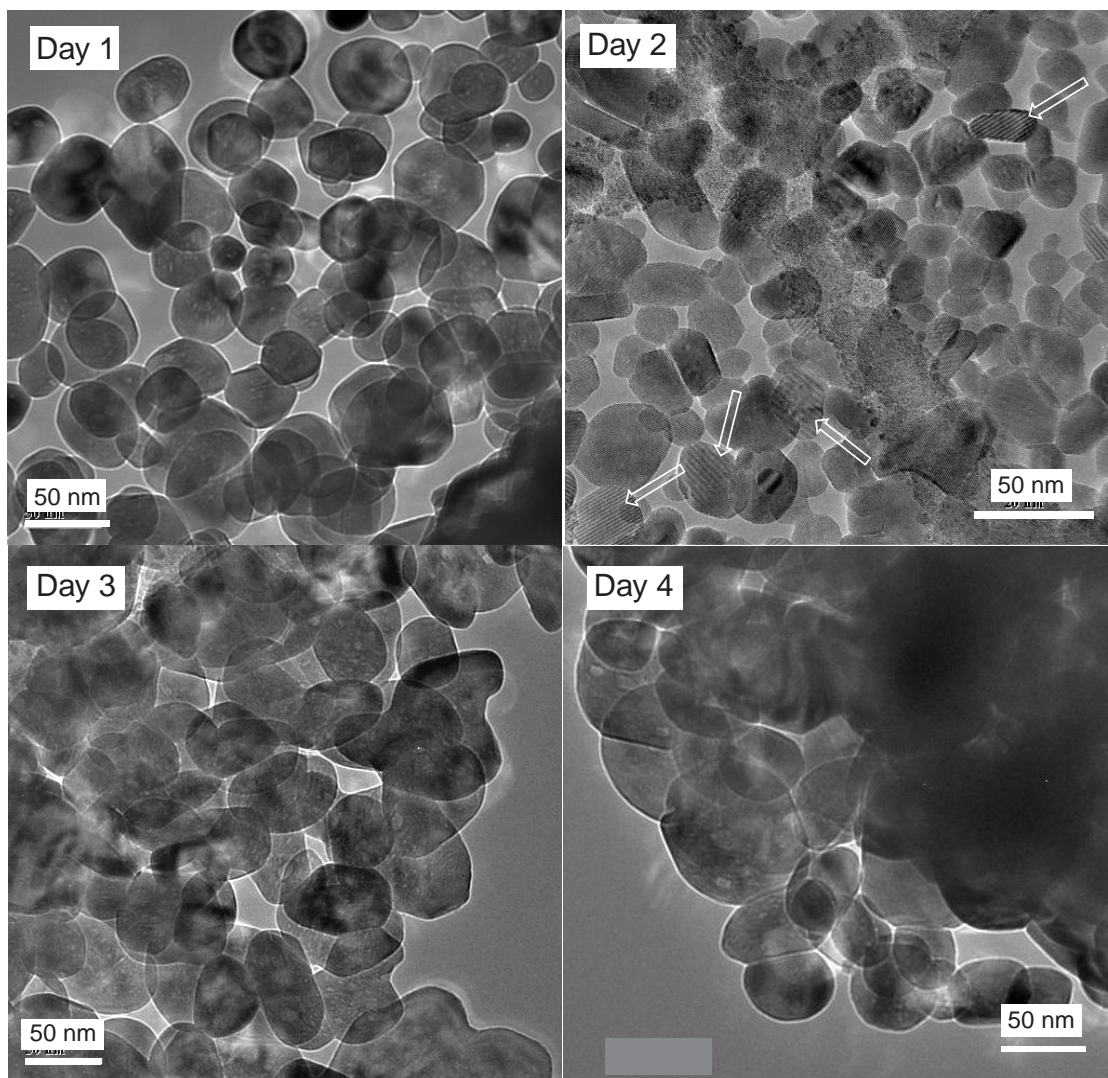
Figure 3.9. High-resolution TEM micrographs of Mo-POM mother liquor with various times (Step **H** in page 2: **Figure 1.1**). White arrows indicate features contain moiré pattern.

In the preparation of TEM samples, the mother liquor was placed on a lacey carbon-support, copper grid and was dried at room temperature and atmospheric pressure prior to introduction into the high-resolution TEM instrument. The nanostructures in the mother liquor probably deformed or

collapsed during the drying process as a result of loss of internal solvent molecules. Larger, less symmetrical features than observed with **ppt1.1** were found in these TEM images (**Figure 3.10A**). We also observed ordered microcrystalline packing across small areas which produced an ordered diffraction pattern (**Figure 3.10B**), presumably due to lattice structures in the solid state.
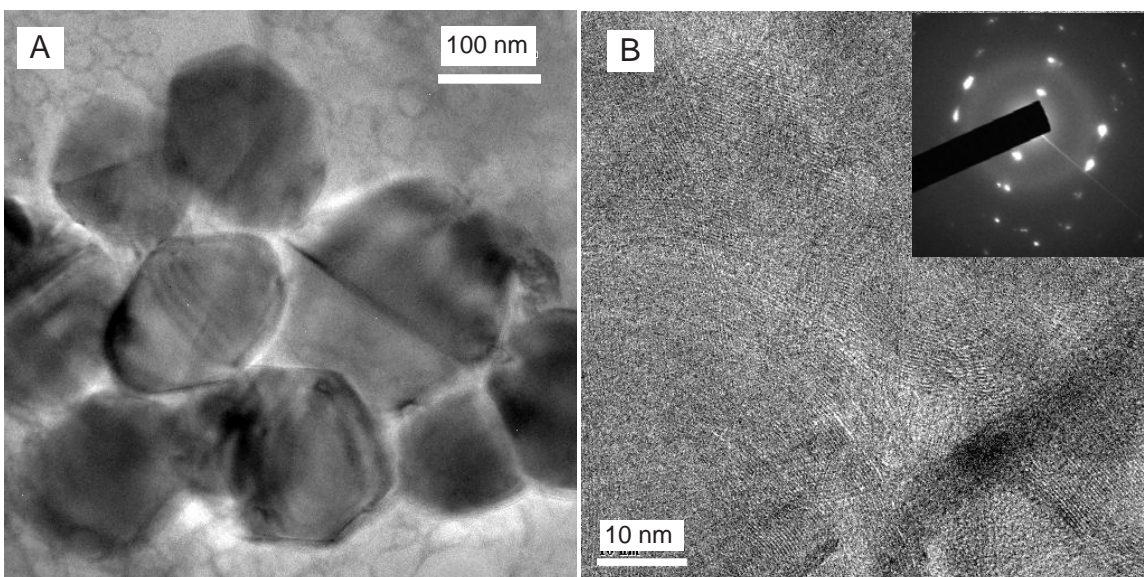
Figure 3.10. (**A**) represents deformed nanoscopic species caught in the TEM images. (**B**) a image of ordered packing over small areas (Step **H** in page 2: **Figure 1.1**). The inserted figure is a diffraction pattern of the area in the image.

3.6 SEM study of the precipitates formed in keplerate {Mo$_{132}$} preparation

　　Solids from the mother liquor of the keplerate preparation were assayed by scanning electron microscopy (SEM). Two representative SEM micrographs were presented in **Figure 3.11**. It is fascinating that two distinct morphologies of precipitates are observed. The well-ordered octahedral crystals corresponded to

keplerate $\{Mo_{132}\}$, determined by indexing these crystals. Some spherical, non-crystalline solids were also present in the material that precipitated over days from the mother liquor of the preparation of keplerate $\{Mo_{132}\}$. These were observed to disappear over time (compare **Figure 3.11A** and **B**) to leave only the crystalline material.
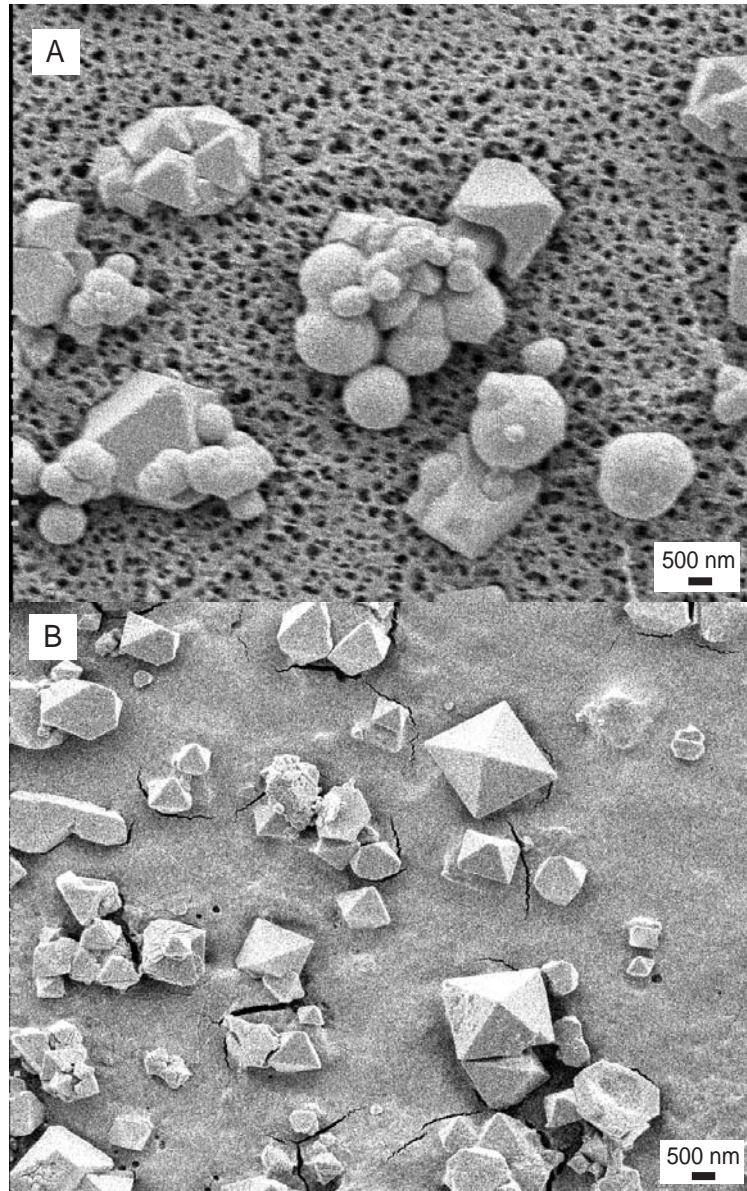
Figure 3.11. SEM micrographs of precipitates formed in the keplerate preparation (Step **I** in page 2: **Figure 1.1**). (**A**): after day 7; (**B**): after day 36.

More remarkably, structural deviation in the spherical species may be caught in some SE micrographs. SEM analysis suggested that the merger of small spherical structures with larger structures. Because spherical structures disappeared with time in a concentrated solution to leave only the octahedral crystals, the material in the spherical structures must have converted to the octahedral structures by either a direct solid-state process or by a re-dissolution/ crystallization process. Like the TEM studies reported in the previous pages, this SEM study supported the notion that spherical nanoscopic solids continued to grow in the Mo-POM mother liquor; the species observed in the SEM study had comparatively large dimensions (100-1500 nm). These dwarfed the structures observed by TEM that adsorbed from the mother liquor onto the lacey carbon copper grids (10-100 nm). It is logical that the nanoscale, spherical material that precipitated would have been bigger than the nanoscale material that was stable in solution. Large polymeric species tend to be less soluble than smaller species.

Based on the results from FIFFF, TEM and SEM studies, two hypotheses were proposed to elucidate the structural evolution of solution-phase Mo-POM nanoscopic species. In both hypotheses the synthesis of keplerate $\{Mo_{132}\}$ is driven forward by an energetically favored crystal-lattice. The two hypotheses differ however in regard to the nature of the solution-state material. In the first hypothesis, single keplerate building blocks function as 'seeds' for the self-aggregation process. At the initiation of the growth, single keplerate units aggregate into small amorphous clumps. The clumps undergo a morphological change to become into vesicles, hollow species at d~25 nm. In a third stage of

growth lamellar accretion increases the vesicle size above 25 nm. In this hypothesis, vesicular growth occurs by adding more layers rather than expanding diameter of a single layer. The vesicles become denser when they attain diameters greater than 25 nm until they are too large to remain in solution. This paradigm is a modification of Liu's single-layer vesicle model for a chemically related Mo-POM.[5] **Figure 3.12** is a schematic representation of Mo-POM growth model (hypothesis **1**) related to keplerate $\{Mo_{132}\}$.
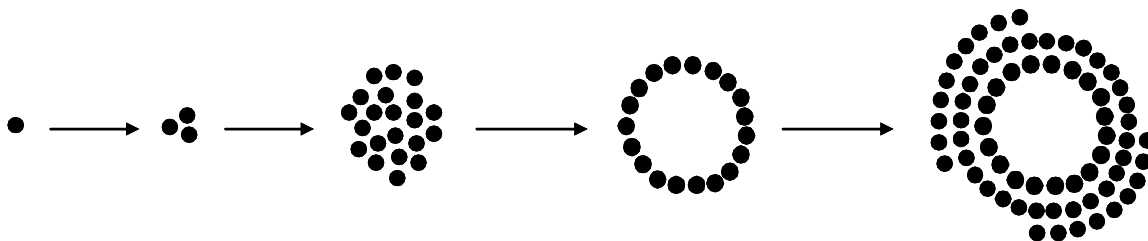
Figure 3.12. Mo-POM growth model (**hypothesis 1**) related to keplerate $\{Mo_{132}\}$.

In the second hypothesis (**Figure 3.13**), the self-aggregation process also starts from keplerate $\{Mo_{132}\}$ building blocks. When keplerate molecules come close enough, they merge into ellipsoidal intermediates. Kinetically unstable, these non-spherical species rearrange to spherical species. Stepwise growth of intermediates results in thin vesicles at d~25 nm. Further growth occurs by the aggregation of vesicular structures.
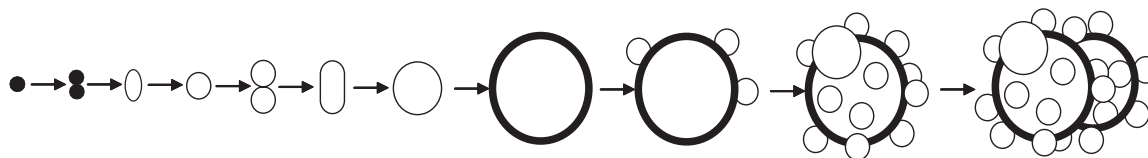
Figure 3.13. Mo-POM growth model (**hypothesis 2**) related to keplerate $\{Mo_{132}\}$.

The merits of both hypotheses need to be evaluated in light of the experimental evidence. The first hypothesis is a modified version of one found in the literature, that was used to explain data from dynamic light scattering.[5] In that work, Liu deduced that most of the mass that was on the surface of nanoscopic species was related to the UV-transparent keplerate $\{Mo_{72}Fe_{30}\}$. He hypothesized that keplerate $\{Mo_{72}Fe_{30}\}$ is a solution-stable species and that the larger nanoscopic species evolve from these smaller units via an *aufbau* process: the building up process. Liu's dynamic light scattering studies and the FlFFF data in the current work can not adequately differentiate the first from the second hypothesis.

However, the first hypothesis does not fare as well in light of the TEM data. By the first hypothesis species of d~7-9 nm should be composed of 6-9 keplerate units that are closed packed in some fashion. However by TEM features in this range of sizes are smoothly constructed. They do not appear to be the result of small species composed of closely packed spheres of keplerate $\{Mo_{132}\}$.

The second hypothesis is favored by the observation of ellipsoidal features in the transmission electron micrographs and the dynamic nature of these polyoxomolybdate structures. When these species were trapped by kinetic precipitation, the elliptical species had one axis twice as long as the other. Asymmetric, smoothly constructed species were also observed in TEM samples of polyoxomolybdate in the mother liquors of keplerate preparations. The nondescript aggregation in hypothesis two is supported by the TE and SE

102

micrographs obtained in the current study. Preliminary time-dependent, kinetic precipitation experiments with **1.1** indicate that aggregated species dominate the TEM field after the dissolved keplerate is left to stand for more than one day. Individual nanoscopic species do not stand out in these micrographs.

3.7 Conclusion

In this study, an unusual combination of analytical techniques (time-dependent FFF, SEM and TEM) has been used to clarify the dynamic nature of partially reduced Mo-POM solutions and to offer information about the long-standing mystery of partially reduced molybdenum oxide aqueous solutions; such as what species are really present in the molybdenum blue solutions.

The current work has demonstrated for the first time that nanoscopic components in partially reduced Mo-POM solutions can be fractionated by using flow field-flow fractionation. Material redissolved from the crystalline keplerate {Mo$_{132}$} and material from the mother liquor was used in this study. Distinct polydisperse size distributions have been observed not only for keplerate {Mo$_{132}$} aqueous solution but also for the Mo-POM mother liquor related to keplerate {Mo$_{132}$}. While the particle size changed over the course of monitoring in keplerate {Mo$_{132}$} aqueous solution, the Mo-POM mother liquor presented a different story. The particle sizes in the mother liquor were almost the constant although their population decreased dramatically at the first two days and then reached a steady state over a longer time. The difference between the dynamic behaviors of these two materials must have been simply because keplerate

{Mo_{132}} upon dissolution was further from thermodynamic equilibrium than the nanoscopic material evolving in the mother liquor of the preparation of keplerate {Mo_{132}}. The most stable state for the polyoxomolybdate in the crystal is keplerate {Mo_{132}}. The most stable state for the polyoxomolybdate in aqueous solution is a distribution of nanoscopic species.

The calculated molybdenum distribution in unit particle mass as well as molybdenum distribution in unit particle surface area presented a clearer picture for understanding Mo distributions in particles. Within the particle size range of 3 to 25 nm, Mo concentrations generally decreased with the increase of particle sizes. After the point of d~25 nm, both Mo mass concentrations started to increase according to particle sizes. These results suggest that the aggregates are not all single-layer vesicles buildup of {Mo_{132}} building blocks but the thickness of the vesicles varies with particle sizes. This conclusion is different from Liu's light scattering studies of a chemically related keplerate {$Fe_{30}Mo_{72}$}. In that study, the author concludes that the large Mo-POM aggregates are single-layer vesicles.[5]

Further TEM results were in accordance with FlFFF results for the particle size distributions. The results indicate that the formed nanostructures are thermodynamically stable over the course of monitoring. SEM study of the precipitates formed in the keplerate preparation showed two distinct nanoscopic components in the solids. Among them, the spherically nanoscaled objects were not stable and they slowly converted to more crystalline octahedral species over the course of weeks.

3.8 Experimental Section

Mo-POM solutions analyzed were derived from the published preparation of the keplerate $\{Mo_{132}\}$.[1] $N_2H_4 \cdot H_2SO_4$ (0.08 g, 0.61 mmol) was added to a 25 mL solution of $(NH_4)_6Mo_7O_{24} \cdot 4H_2O$ (0.56 g, 0.45 mmol) and ammonium acetate (1.25 g, 16.2 mmol) and stirred for 10 min. Aqueous acetic acid (50% vol, 8.3 mL) was subsequently added and the reaction solution was stored in an open flask at 20 °C without further stirring.

FlFFF Carrier Liquid and Standards:

The FlFFF carrier solution was pure, deionized Milli-Q water (Millipore) containing 0.007% (w/v) Triton X-100 surfactant and 0.02% (w/v) sodium azide (NaN_3) bactericide. The carrier fluid was passed through a Millipore HPLC inlet solvent filter with a pore size of 10 µm in the channel and cross-flow delivery lines. In order to monitor the performance of the FlFFF instrument and to calibrate the size distributions of the particular particles, standard polystyrene beads of 20 and 50 nm in diameter (Duke Scientific, Palo Alto, CA, USA) were used. One drop of the original concentrated suspension was dispersed in 5 mL of FlFFF carrier solution to obtain an individual standard solution for the FlFFF injection.

1. Samples

Redissolved Keplerate $\{Mo_{132}\}$: 10 µL solution was directly taken for FlFFF measurement each time. **Mother liquor**: 10 µL suspension in the flask was taken for FlFFF measurement each time. Upon sampling, the suspension was diluted

by 30 μL deionized Milli-Q water. The diluted suspension (5 μL) was then directly injected into the FIFFF channel.

2. FIFFF Instrumentation

FIFFF separations were conducted by using a standard instrument (FFFractionation LLC, Utah, USA, Universal Fractionator model F1000). The dimensions of the channel were 29.4 cm in tip-to-tip length, 0.0197 cm in thickness and 2.0 cm in breadth. The geometrical void volume was 1.09 cm^3. A regenerated cellulose membrane with a 10,000 Dalton molecular weight (about 3 nm) cut-off was used. Sample of about 5 μL was injected into the channel through a Rheodyne sample injection port. Two Intelligent Pump Model 301 HPLC pumps were used to deliver carrier liquid in the channel and non-recirculating cross-flows. A channel flow of 0.5 mL·min^{-1}, a cross-flow of 3.00 mL·min^{-1} and an equilibrium time of 0.72 min were used. During the equilibrium time, the cross-flow establishes a steady-state distribution of the particles in the channel prior to initiation of the channel flow. Fractograms were obtained by monitoring the absorbance of the eluate at 455 nm by using a Linear Instruments Model 200 UV/Visible detector.

Samples for SEM analysis:

A small amount of precipitates was suction-filtered through an alumina filter membrane (Whatman Anodisc 13, pore size 20 nm) and was dried at room temperature. A piece of a carbon conductive tab was adhered onto a copper plate of the SEM specimen holder. The membrane was placed onto the carbon

conductive tab and was finally coated with Au (Emscope, model SC 400) prior to SEM measurement. The materials were examined using a Hitachi S900 field-emission scanning electron microscopy.

Samples for TEM analysis:

About 10 µL reaction solution was daily sampled for TEM measurement. Upon sampling, about 10 µL was placed on a lacey carbon copper grid (Lacey Carbon Type-A, Ted Pella, Inc.). After soaking the grid for 2 min, the excess solution was removed by filter paper and the grid was allowed to air dried at room temperature. The materials were examined using a high-resolution Transmission Electron Microscope (JEOL JEM-2010F).

Samples for ICP analysis:

1: 20 µL of Mo-POM mother liquor was diluted into 10 mL using CH_3COOH/CH_3COONH_4 buffer. Half of this solution was subjected to UV/VIS measurements (UV 3101PC, Shimizu); the left solution was fed directly into the ICP torch of an ICP-OES (VISTA-PRO, Varian) to determined the total Mo content in the mother liquor.   **2:** The eluent from the FlFFF was collected every four minutes and fed directly into the ICP torch to determine the Mo content in the FlFFF fractions. Calibration of instrument was achieved using a standard solution containing 1000 ppm Mo. This standard solution was diluted 100-, 200-, and 2000-fold to obtain calibration curve for Mo element.

References:

(1) Müller, A.; Krickemeyer, E.; Bögge, H.; Schmidtmann, M.; Peters, F. *Angew. Chem. Int. Ed.* **1998**, 37, 3360-3363.

(2) Müller, A.; Meyer, J.; Krickemeyer, E.; Beugholt, C.; Bögge, H.; Peters, F.; Schmidtmann, M.; Kögerler, P.; Koop, M. J. *Chem. Eur. J.* **1998**, 4, 1000.

(3) Xu, R. *Particle Characterization: Light Scattering Methods Particle Technology Series*, Ed.: Scarlett, B.; Kluwer Academic Publishers, **2001**.

(4) Müller, A.; Diemann, E.; Kuhlmann, C.; Eimer, W.; Serain, C.; Tak, T.; Knöchel, A.; Pranzas, P. K. *Chem. Comm.* **2001**, 1928.

(5) Liu, T. *J. Am. Chem. Soc.* **2002**, 124, 10942-10943.

(6) Filella, M.; Zhang, J.; Newman, M. E.; Buffle, J. *Collids Surf. A: Physicochem. Eng. Aspects* **1997**, 120, 27.

(7) Giddings, J. C. *Science* **1993**, 260, 1456-1465.

(8) Schimpf, M.; Caldwell, K. D.; Giddings, J. C. *Field-flow Fractionation Handbook*, John Wiley: New York, **2000**.

(9) Lee, H. K.; Williams, S. K. R.; Anderson, S. D.; Anchordoquy, T. J.; *Anal. Chem.* **2001**, 73, 837-843.

(10) Petteys, M. P.; Schimpf, M. E. *J. Chromatogr.* **1998**, 816, 145-158.

(11) Hassellov, M.; Lyven, B.; Beckett, R. *Environ. Sci. Technol.* **1999**, 33, 4528-4531.

(12) Lautrette, C.; Cardot, P. J. P.; Vermot-Desroches, C.; Wijdenes, J.; Jauberteau, M. O.; Battu, S. *J. Chromatogr. B.* **2003**, 791, 149-160.

(13) Schiundu, P. M.; Liu, G.; Giddings, J. C. *Anal. Chem.* **1995**, 67, 2705-2713.

(14) Jeon, S. J.; Nyborg, A.; Schimpf, M. E. *Anal. Chem.* **1997**, 69, 3442-3450.

(15) Dunkel, M.; Beckett, R.; Tri, N.; Caldwell, K. D. *J. Microcolumn Sep.* **1997**, 9, 177-183.

(16) Tri, N.; Caldwell, K.; Beckett, R. *Anal. Chem.* **2000**, 72, 1823-1829.

(17) Gorse, J.; Schunk, T. C.; Burke, M. F. *Sep. Sci. Technol.* **1985**, 19, 1073-1085.

(18) Giddings, J. C.; Chen, X.; Wahlund, K. G.; Myers, M. N. *Anal. Chem.* **1987**, 59, 1957-1962.

(19) Beckett, R.; Jue, Z.; Giddings, J. C. *Environ. Sci. Technol.* **1987**, 21, 289-295.

(20) Beckett, R.; Hart, B. T. In *Environmental Particles*; Buffle, J., van Leeuwen, H. P., Eds.; Lewis Publishers: Boca Raton, FL, **1993**; Vol. 2., pp165-205.

(21) Chen, B.; Shand, C. A.; Beckett, R. *J. Environ. Monit.* **2001**, 3, 7-14.

(22) Chen, B.; Beckett, R. *Analyst* **2001**, 126, 1588-1593.

(23) Moon, M. H. In *Field-flow Fractionation handbook*; Schimpf, M. E.; Caldwell, K.; Giddings, J. C., Eds.; Wiley-Interscience: New York, **2000**, pp383-396.

(24) Giddings, J. C.; Myers, M. N.; Caldwell, K. D.; Fisher, S. R. *Methods Biochem. Anal.* **1980**, 26, 79-136.

(25) Giddings, J. C. *Sep. Sci. Technol.* **1984**, 19, 831-847.

(26) Janca, J. *Chromatogr. Sci.* **1988**, 39, 336 pp.

(27) Beckett, R.; Hotchin, D. M.; Hart, B. T. *J. Chromatogr.* **1990**, 517, 435.

(28) Clarkson, P. J.; Poole, D. J.; Rya, C. K.; Sharifi, V. N.; Swithenbank, J.; Waarlo, H. –J.; Ardelt, D.; Falk, H. *Anal. Bioanal. Chem.* **2003**, 377, 39-47.

(29) Müller, A.; Koop, M.; Bögge, H.; Schmidtmann, M. Beugholt, C. *Chem. Comm.* **1998**, 1501.

Chapter 4

Conclusion

The work presented in this dissertation was designed to probe the nature of nanoscopic components in partially reduced polyoxomolybdate solutions, a 200-year-old unsolved problem in chemical science.   A kinetic precipitation protocol was developed to trap solution state structures of aqueous polyoxomolybdate with designed chelating agents. This technique allowed solution state structures of polyoxomolybdate to be preserved in the solid state. This was confirmed by kinetic precipitation of tripodal compound **1.1** and aqueous keplerate Mo-POM in which the polydisperse size distributions and the particle morphologies were snap shots of the solution-phase structures. Comparing the morphologies of **ppt1.1** from the preparative mother liquor with the morphologies of **ppt1.1** from the dissolution of keplerate $\{Mo_{132}\}$ and coprecipitation of Mo-POM provide definitive evidence for kinetic precipitation. Furthermore, the fact that structures in material derived from Mo-POM alone were less stable than **ppt1.1** and observed structural instability in the coprecipitates over the course of weeks provides further evidence for kinetic precipitation.

Kinetic precipitation study of a series of structurally analogous hosts **2.1-2.3** aimed at understanding the relationship between the structure of the molecular host and the formation of nanostructures. It was found that optimum encapsulation of polyoxomolybdate was best done with molecular hosts

possessing three-fold symmetric components, especially with tripodal **1.1**. The evidence from the TEM investigations indicated that geometrical and electronic complementarity in the molecular encapsulation could possibly involve the properties of the inorganic guest and organic host. Speculatively, the micrographs obtained thus far invite the speculation that solution state nanostructures can be both smoothly constructed from polyoxomolybdate building blocks at molecular level and constructed from discrete clusters at the size of keplerate or larger. While some nanoscale features appeared to be smooth, some other features appeared to be the result of the aggregation of nanoscopic species.

A clearer picture of the nature of solution state species of aqueous Mo-POM comes from monitoring the dynamic solution behavior of polyoxomolybdate by using flow field-flow fractionation, electron microscopy and inductively coupled plasma analyses. The polydisperse size distributions observed for the solution state species of Mo-POM distinguished them from small inorganic molecules, which generally distribute uniformly in the solution,

It is worthy to point out that unusual solution behavior generates when molecules have nanometer sizes. The evolution of Mo-POM solution state nanostructures requires days. While the particle growth was observed over the course of a week for keplerate $\{Mo_{132}\}$ background solution, the particle size distributions didn't change significantly for Mo-POM mother liquor from the preparation of keplerate $\{Mo_{132}\}$. The current work turned out that Mo-POM nanoscopic species in solution can exist as single keplerate molecules as well as

aggregates buildup of basic building blocks. More remarkably, these solution state nanoscopic species of aqueous Mo-POM are thermodynamically stable even in very dilute solutions.

Another thing that comes to the front from this study is the nature of these solution state nanostructures; it is more complicated than originally anticipated. A conjunction of FlFFF with ICP-OES study suggests that the aggregated particles are not all single layer vesicles consist of {Mo_{132}} building blocks, the thickness of the vesicles varies with particle sizes. Particle growth occurs by the aggregation of vesicular structures. With the increase of particle sizes (d > 25 nm), the vesicles become thicker and thicker until finally precipitate out. The FlFFF results were corroborated by TEM results. The particle sizes of nanostructures obtained from FlFFF measurements and TEM analyses are consistant.

These observations could possibly be extended to other Mo-POM systems. Preliminary study of carbohydrate-modified Mo-POM shows that the control of the distribution of sizes in Mo-POM by replacing acetate ligands with other functionalities, such as carbohydrate structures, could be possible.

Appendices

A.1: ^{1}H & ^{13}C NMR of tripodal compound **1.1**.
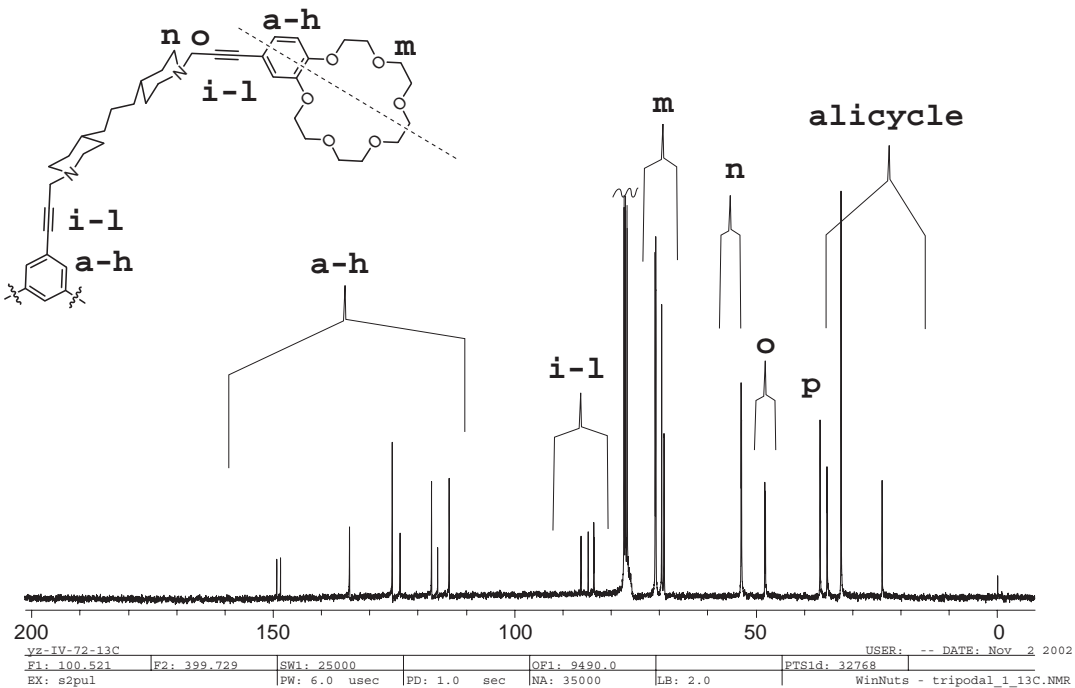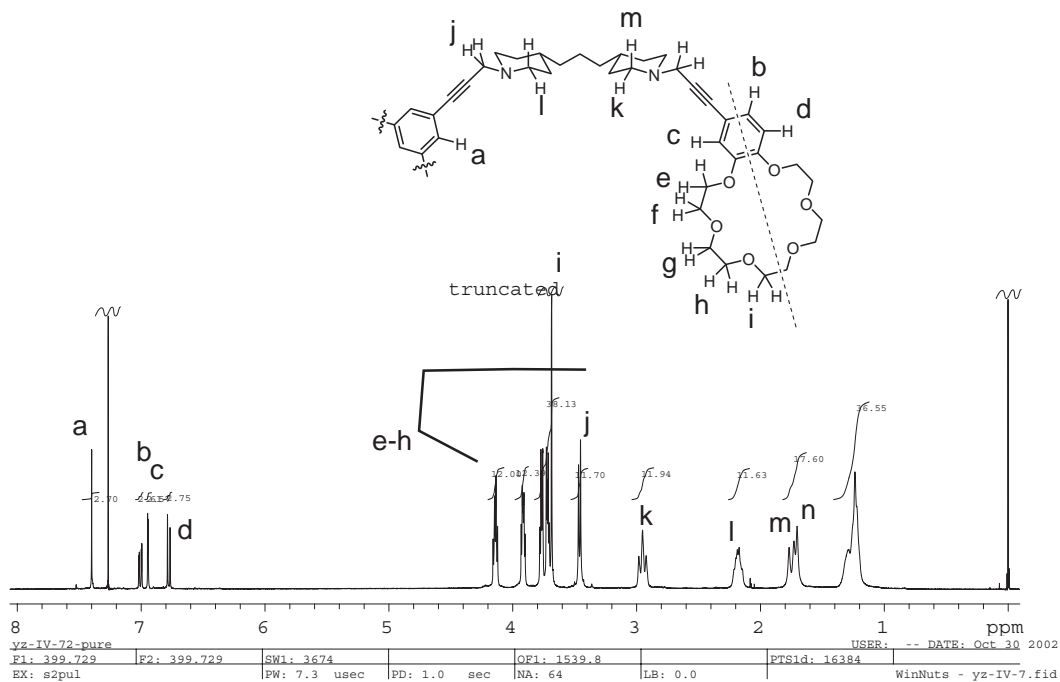
A.2: ^{1}H & ^{13}C NMR of tripodal compound **2.1**.
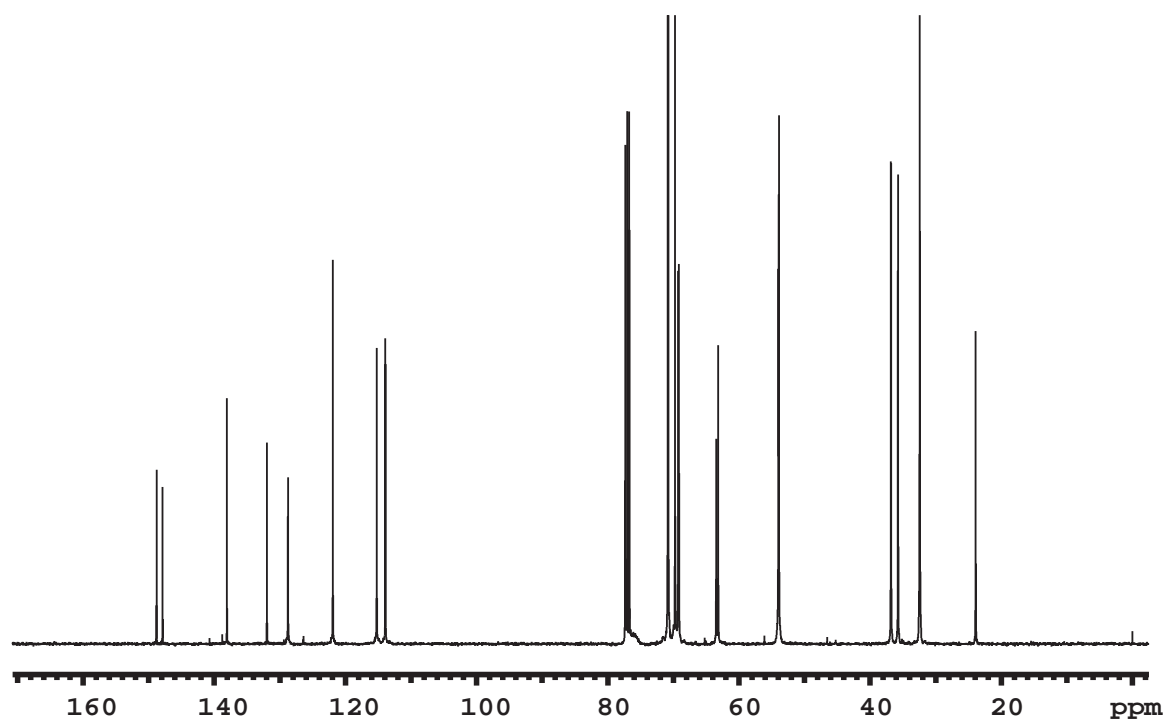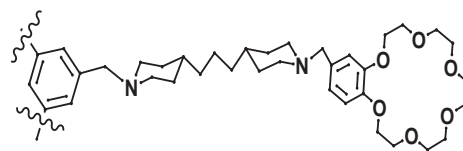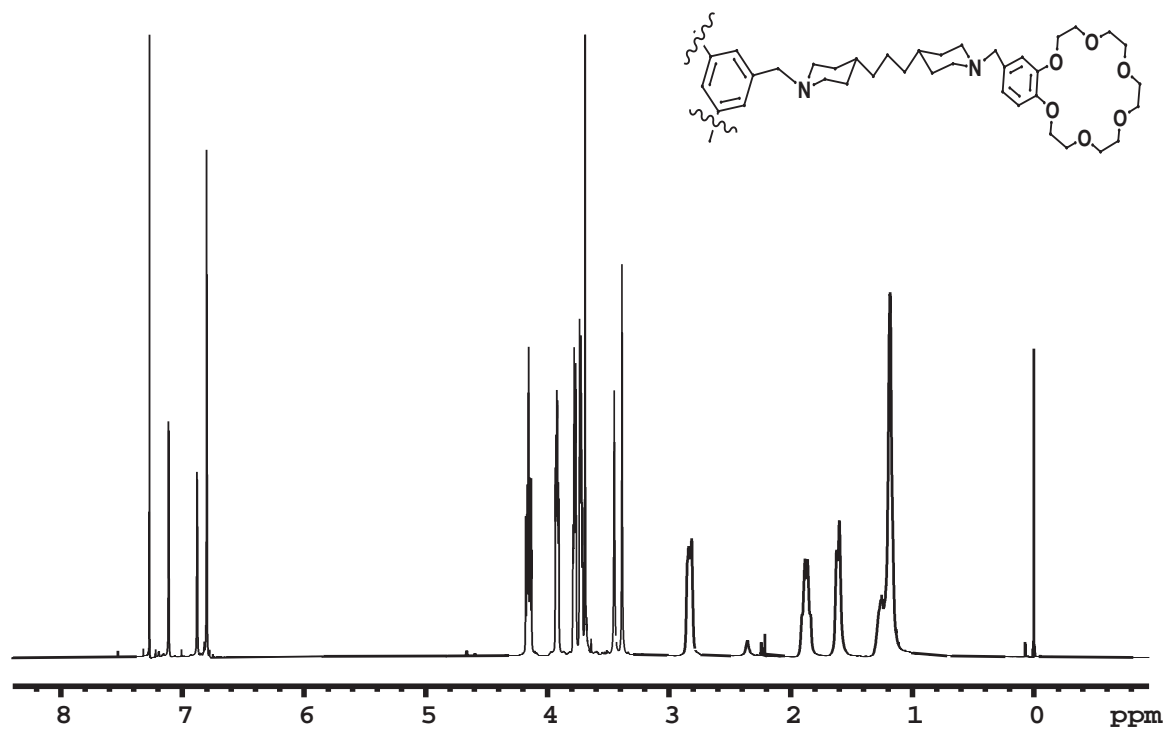
A.3: ^{1}H & ^{13}C NMR of tripodal compound **2.2**.
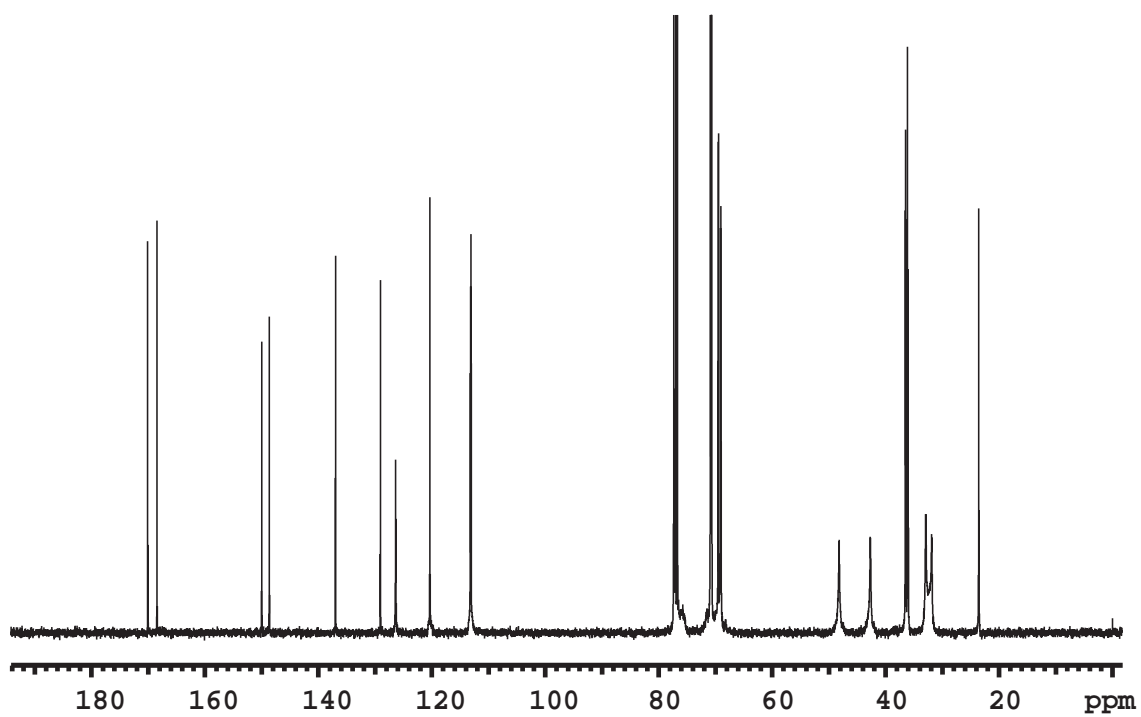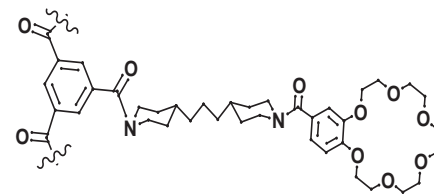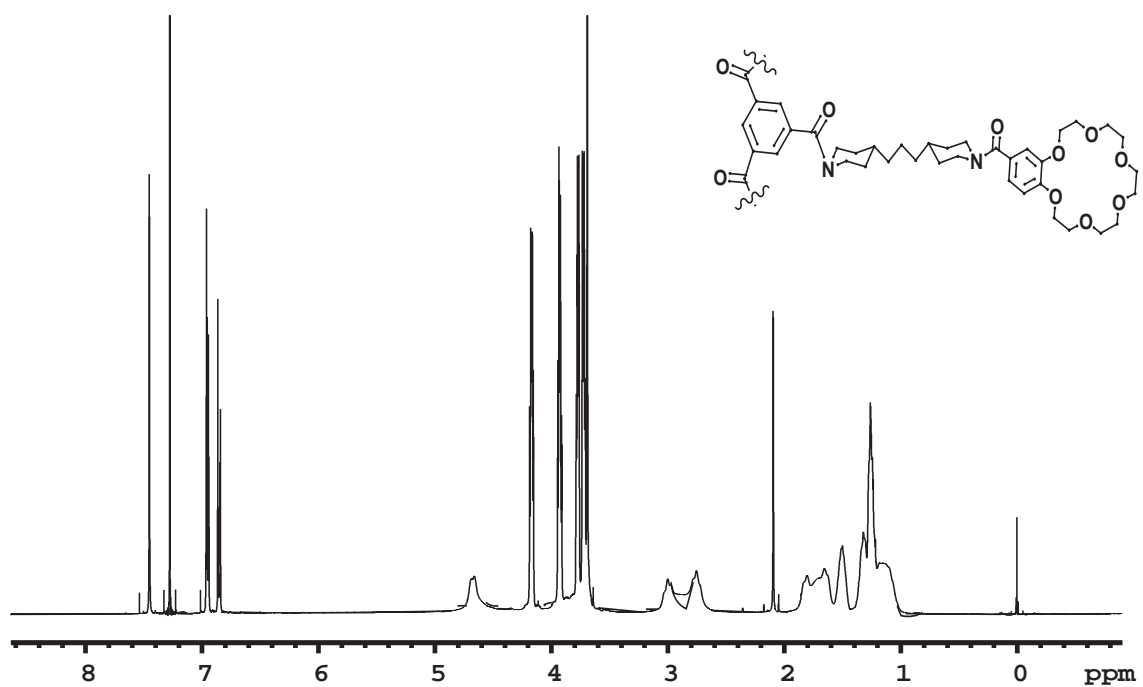
A.4: ^{1}H & ^{13}C NMR of tripodal compound **1.2**.
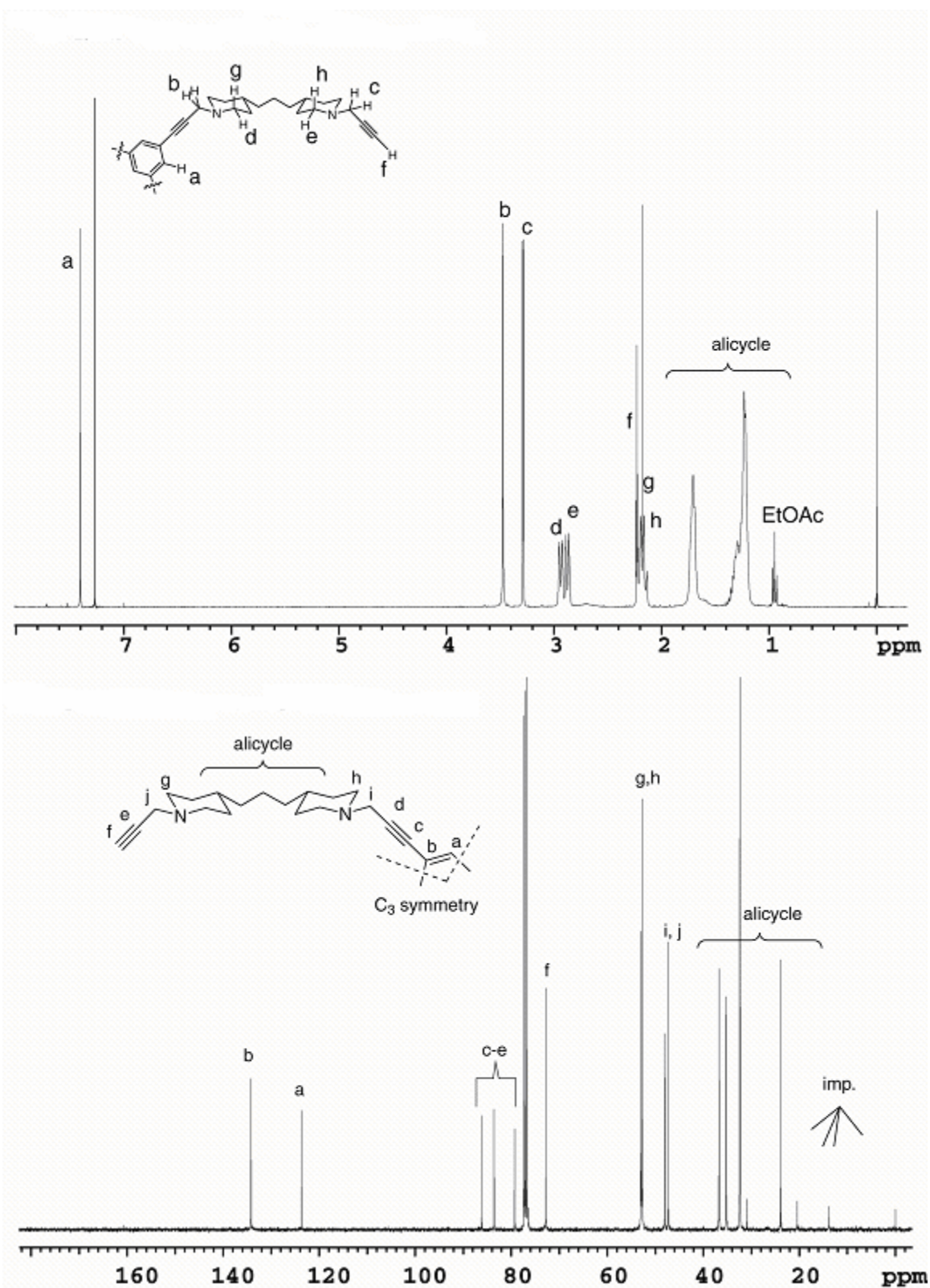
A.5: ^{1}H & ^{13}C NMR of bipodal compound **2.3a**.
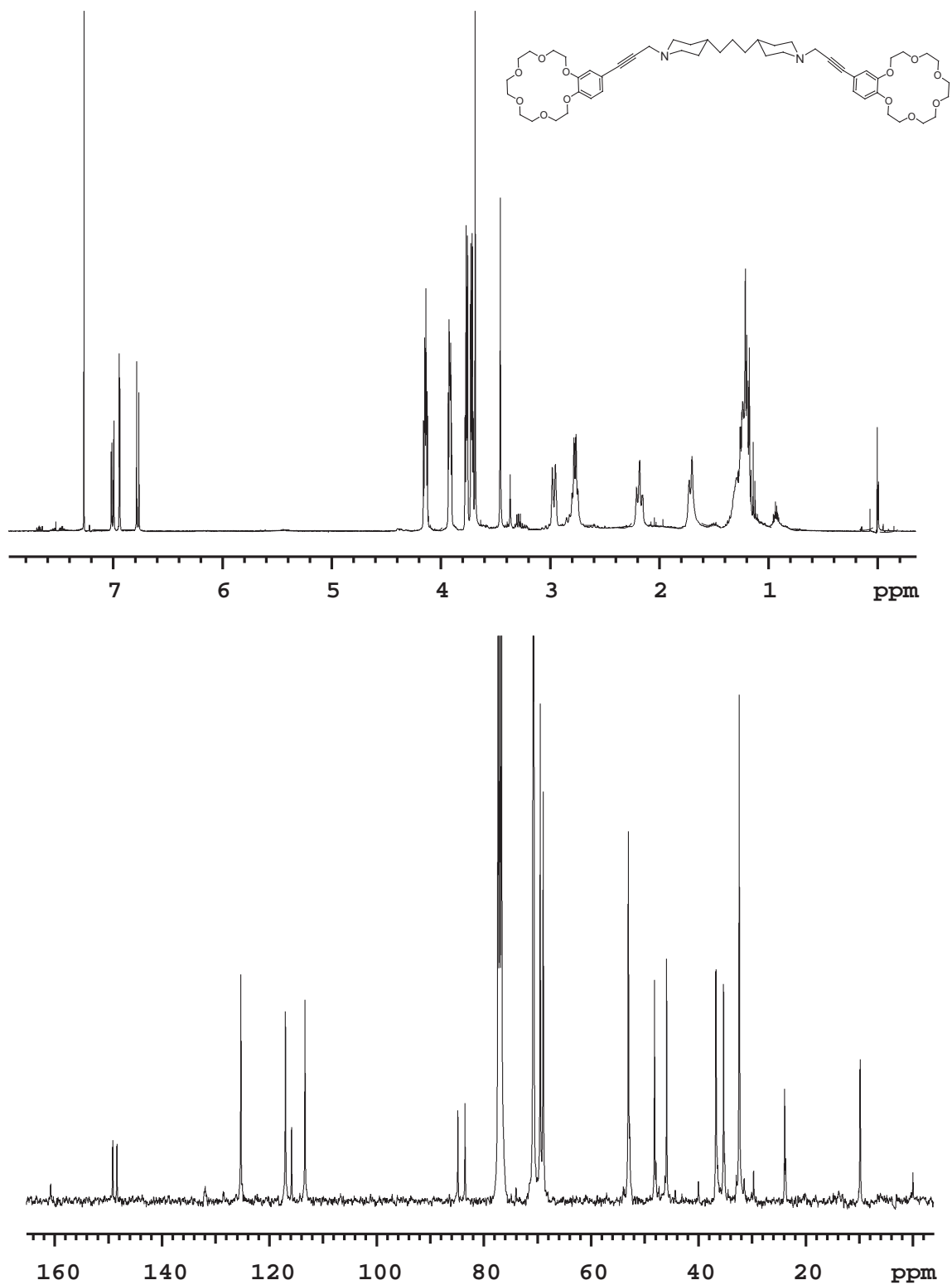
A.6: ^{1}H & ^{13}C NMR of bipodal compound **2.3b**.
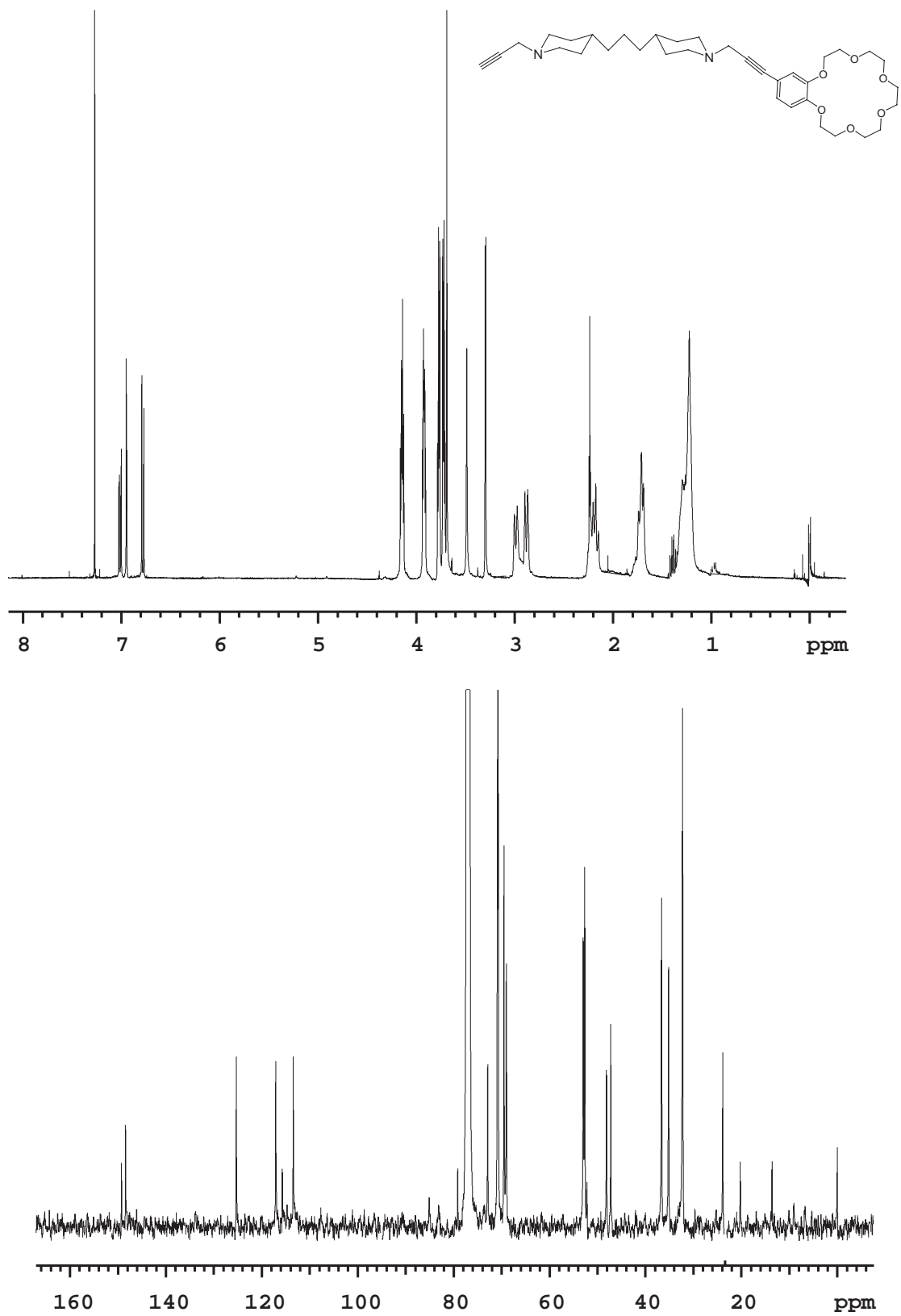
A.7: [^1]H & [^13]C NMR of bipodal compound **2.3c**.
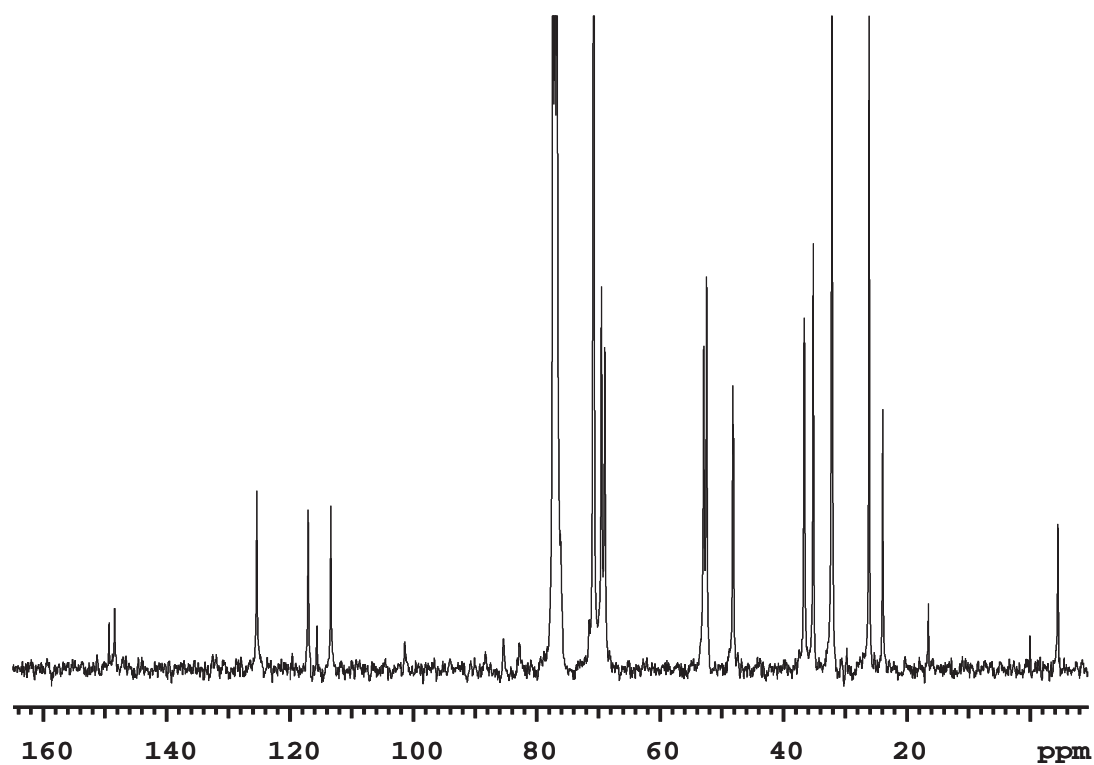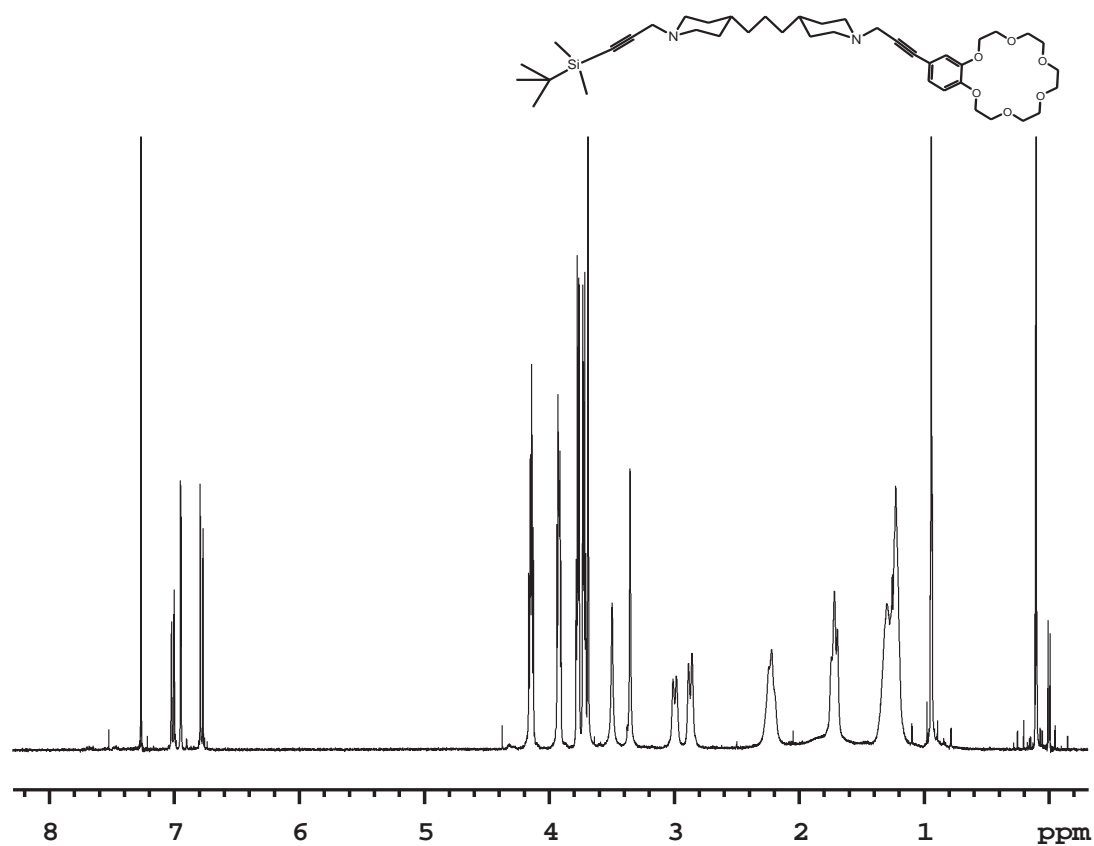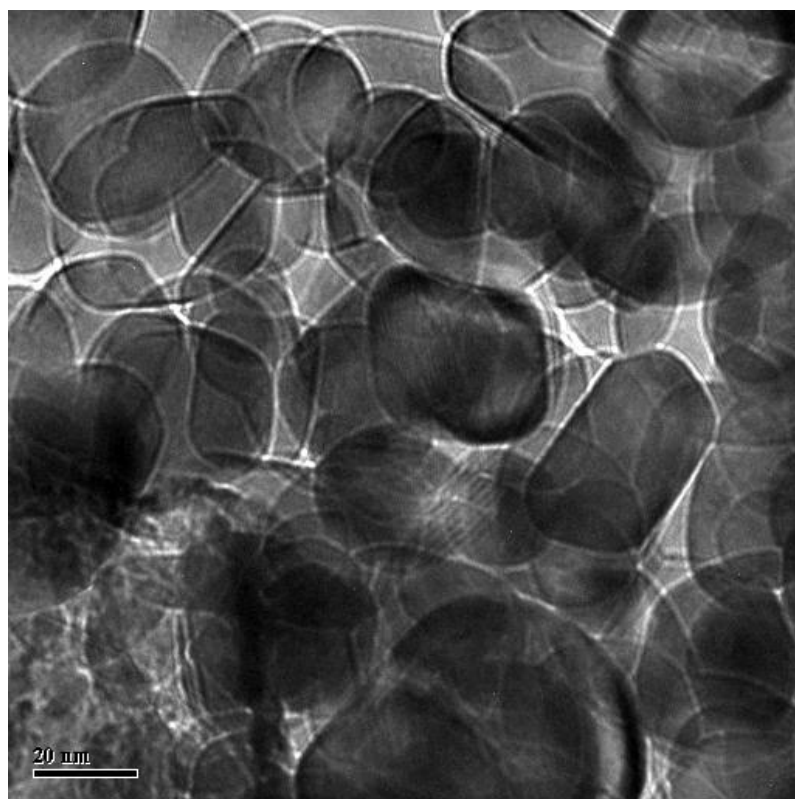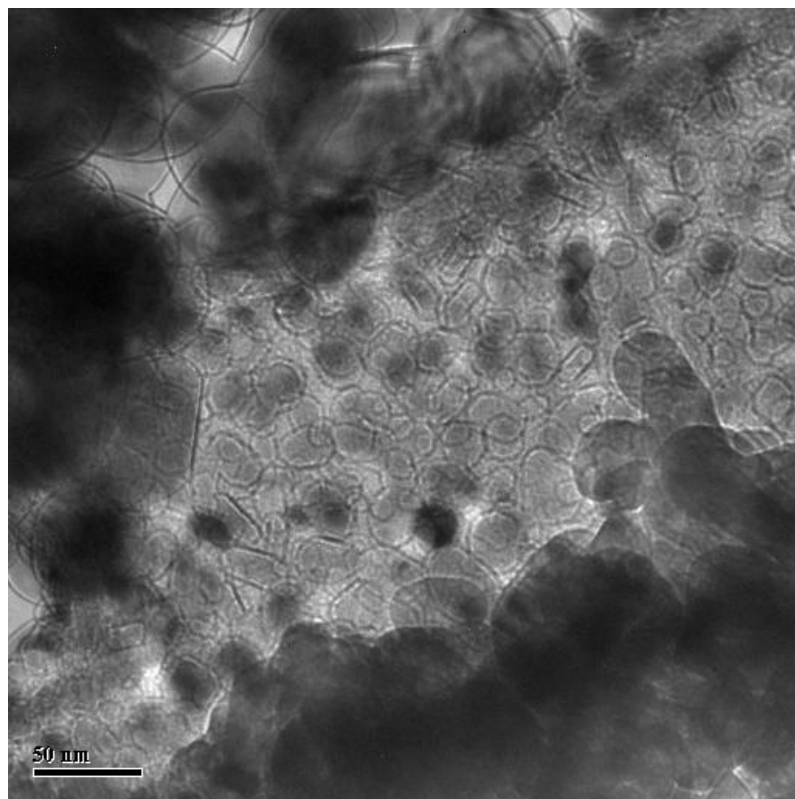
A.8: TEM micrograph of **ppt1.1**.
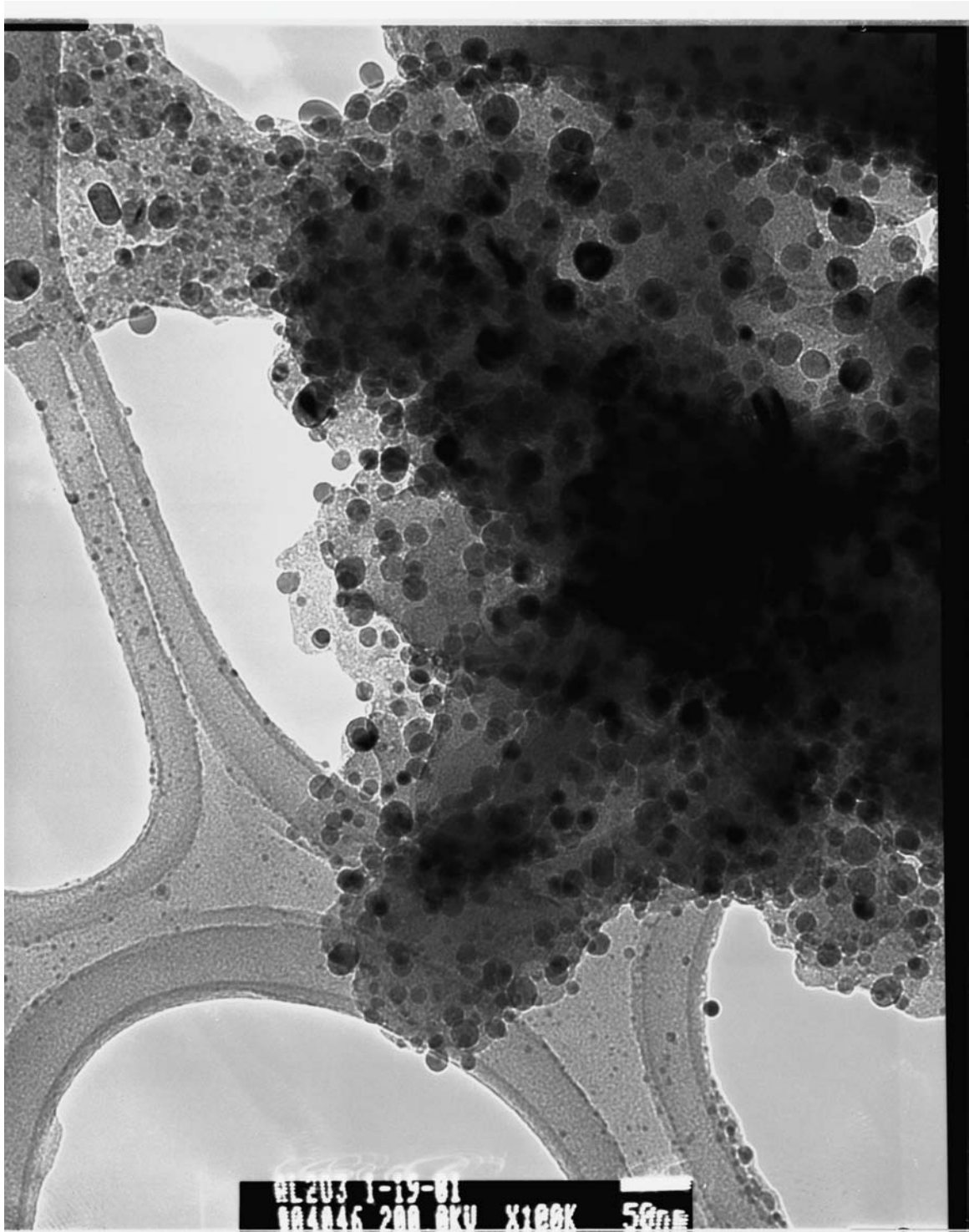
A.9: TEM micrograph of **ppt1.1**.
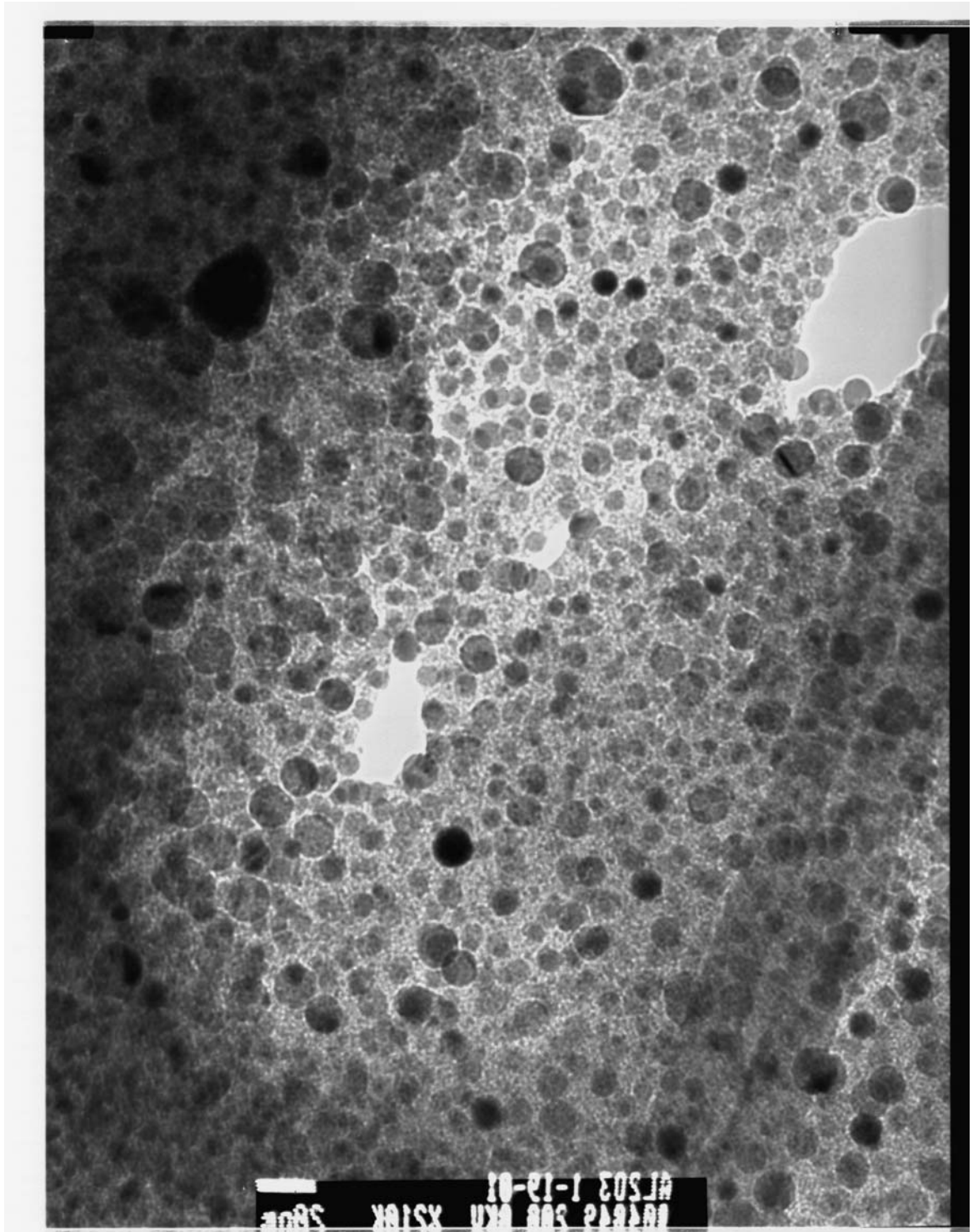
A.10: TEM micrograph of **ppt1.1'**.
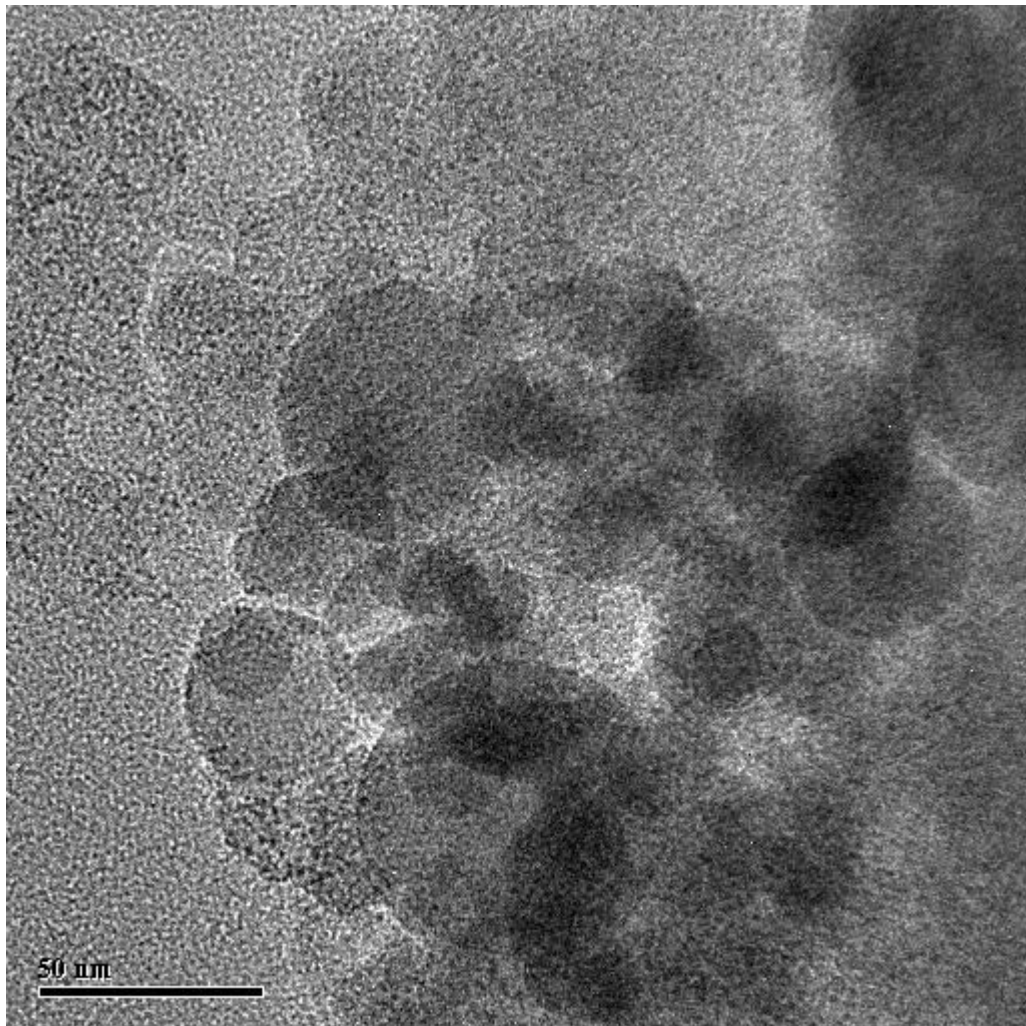
A.11: TEM micrographs of crystalline keplerate {Mo$_{132}$}.

A.12: TEM micrograph of the mother liquor of the keplerate preparation (day 1).
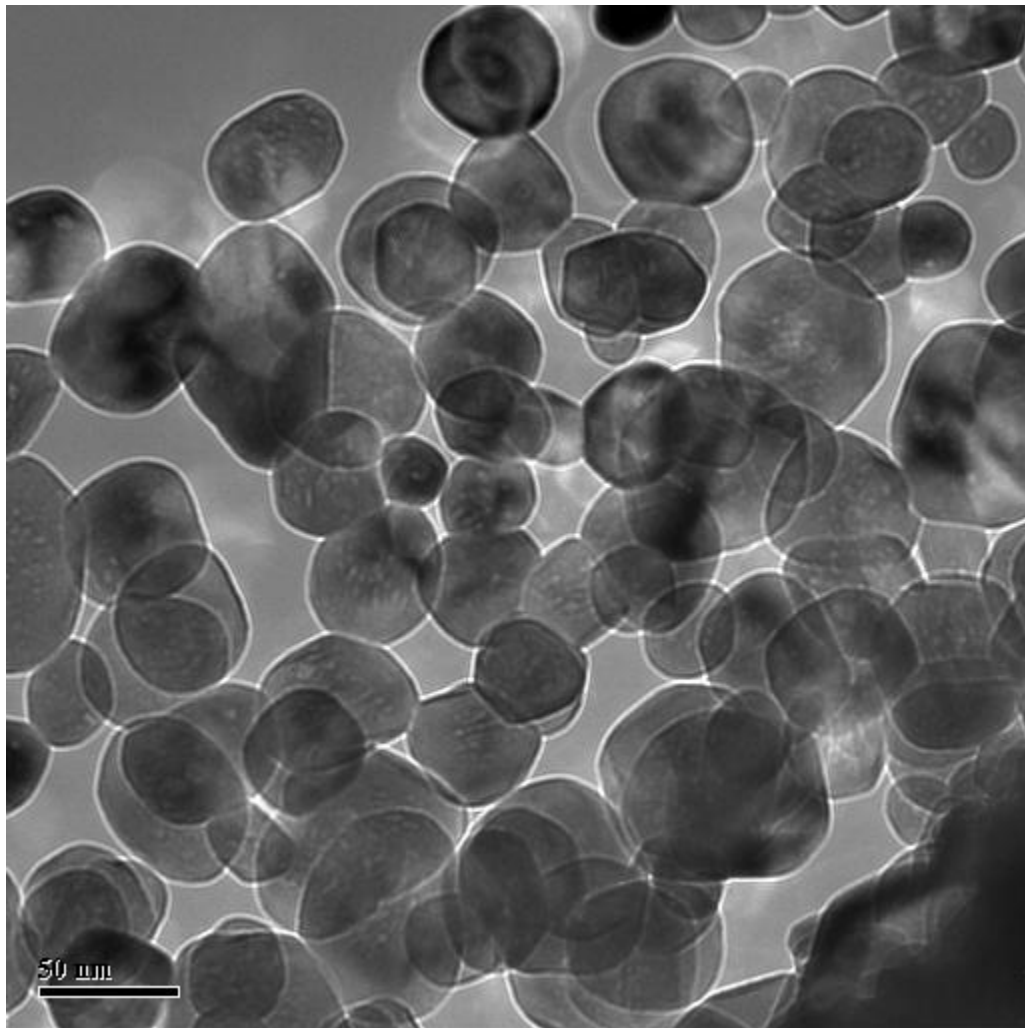
A.13: TEM micrograph of the mother liquor of the keplerate preparation (day 2).
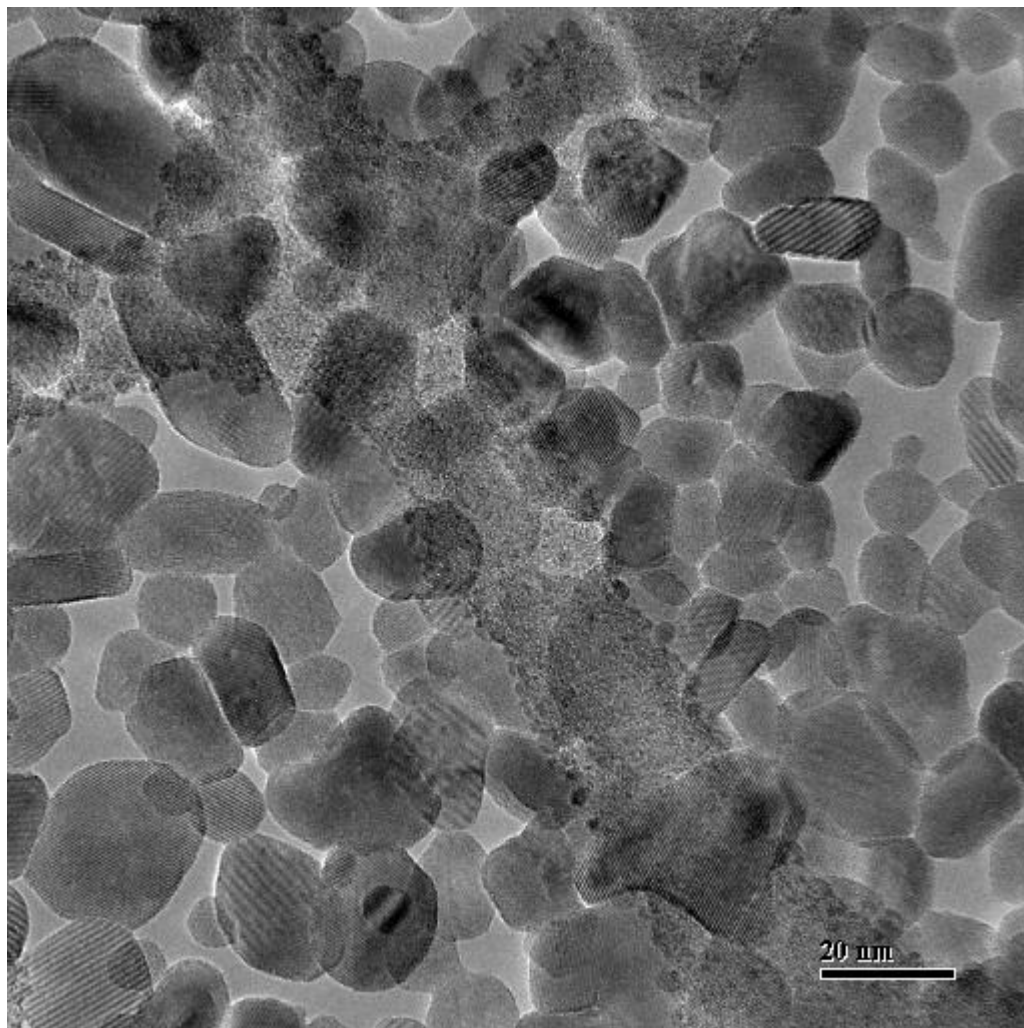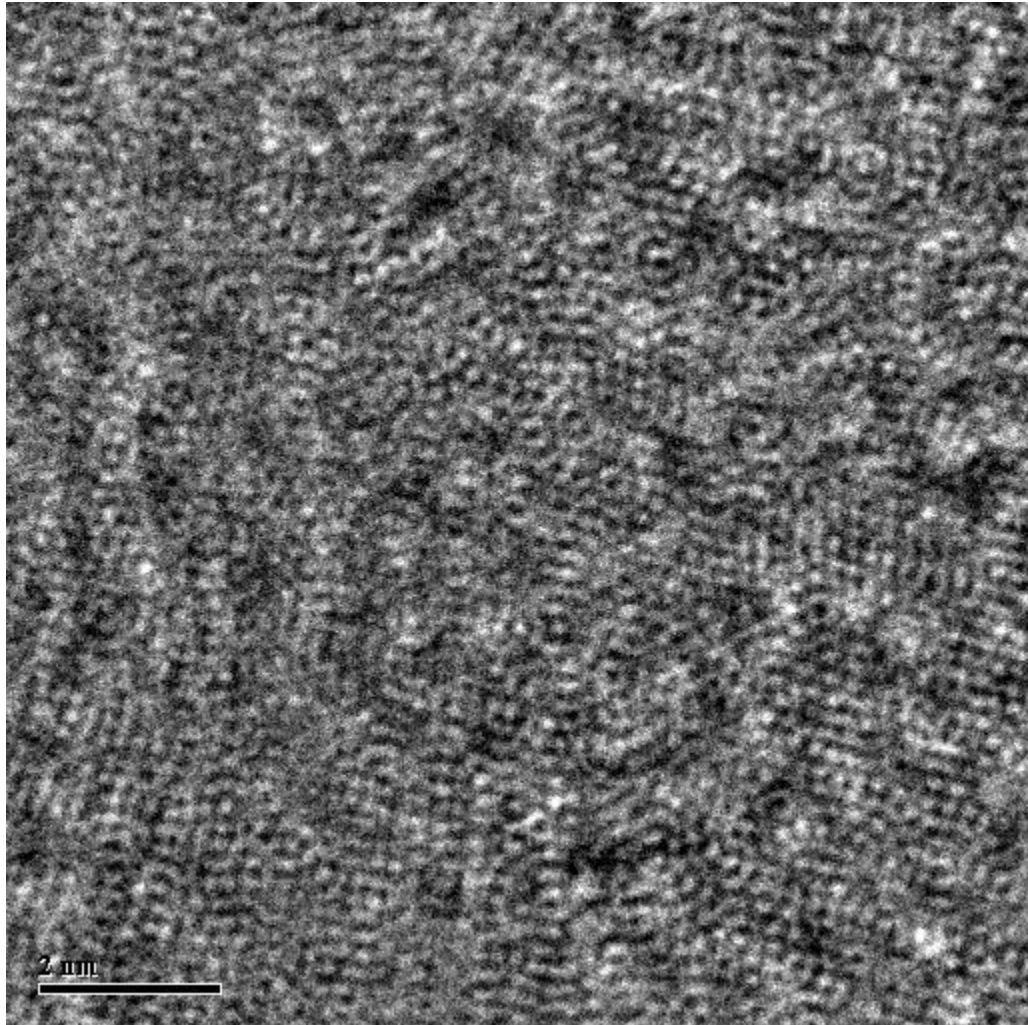
A.14: TEM micrograph of the mother liquor of the keplerate preparation (day 3).
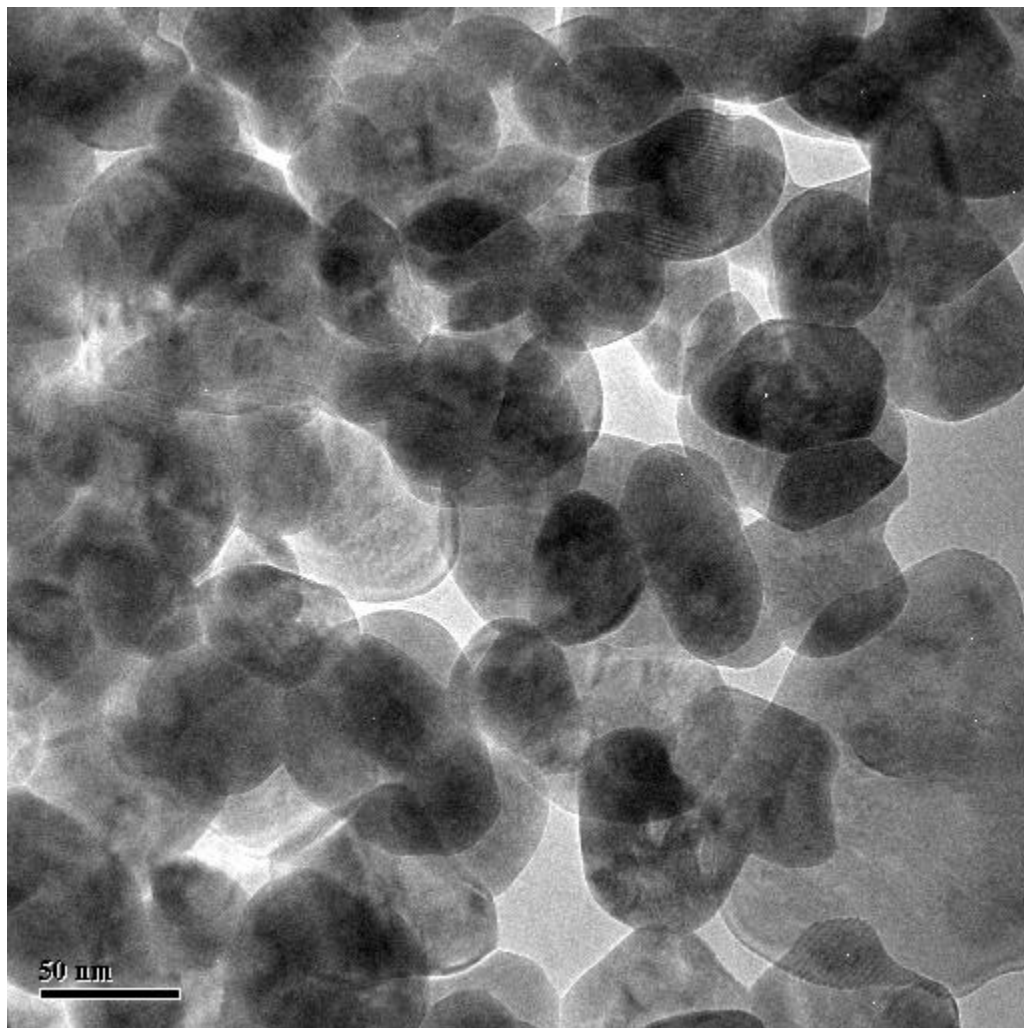
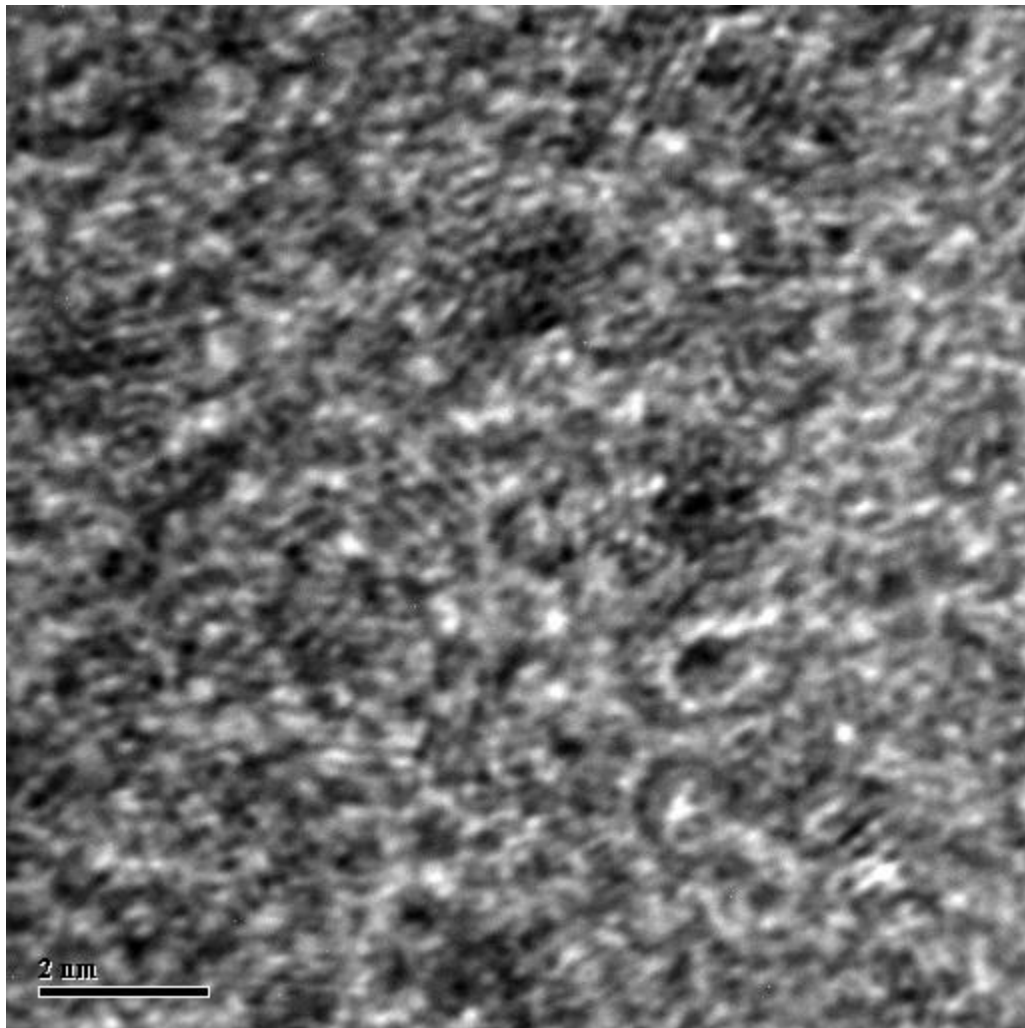**A.15:** TEM micrograph of the mother liquor of the keplerate preparation (day 4).
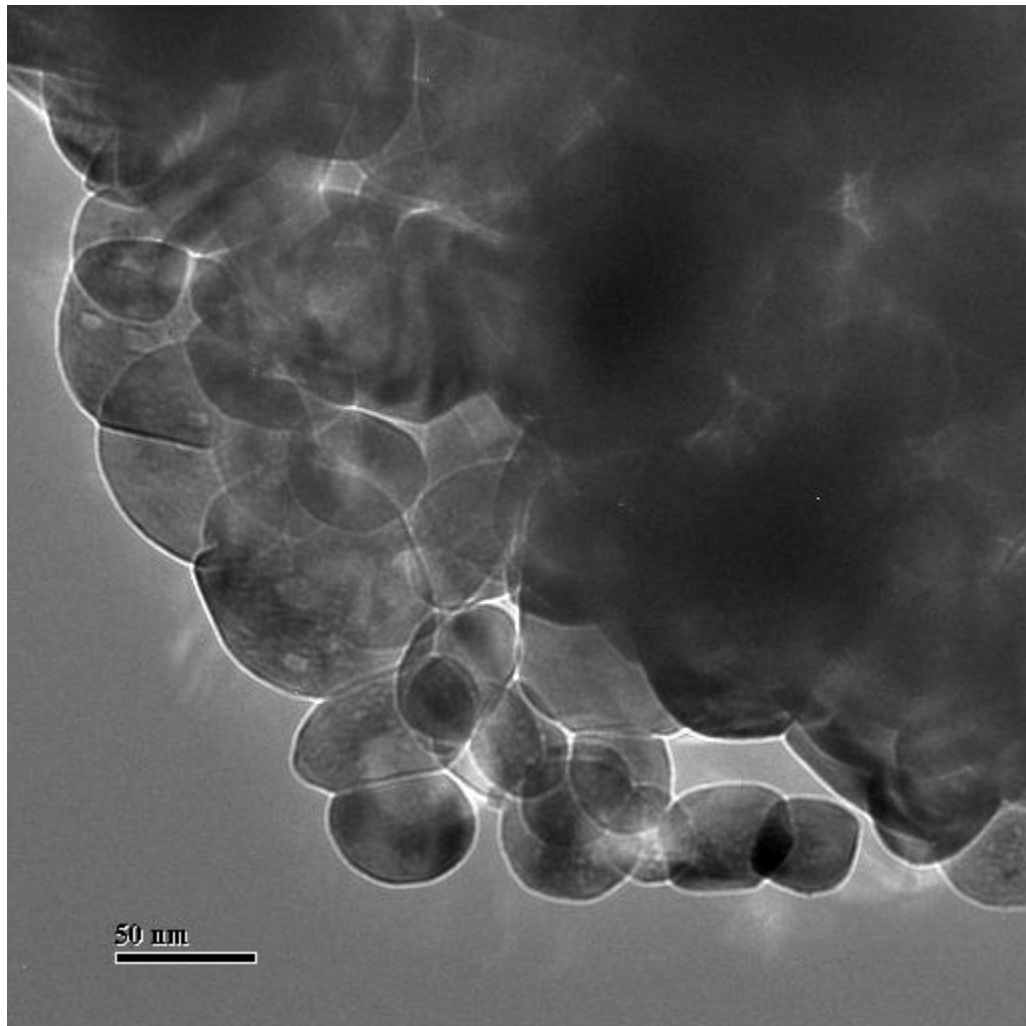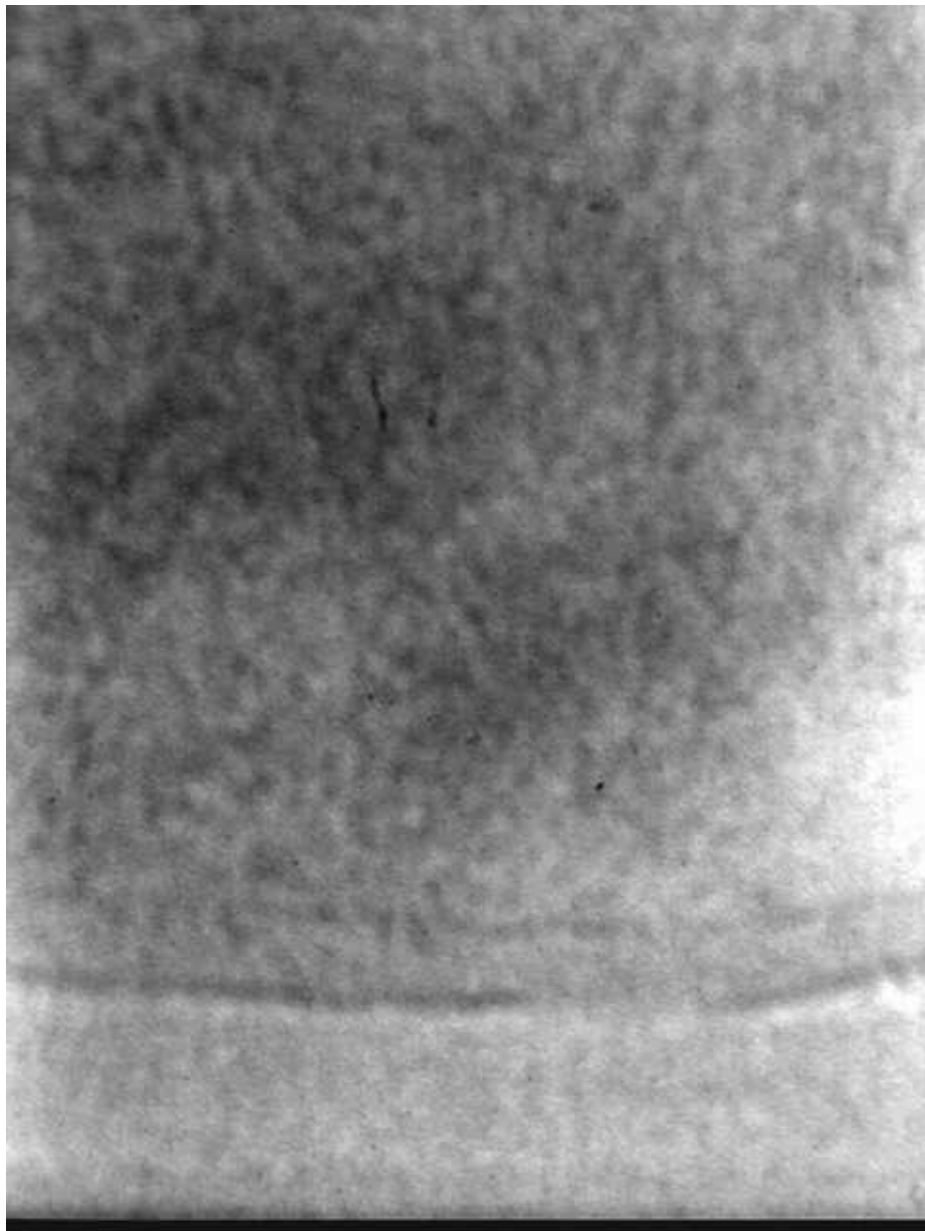
A.16: TEM micrograph of **ppt1.2**.
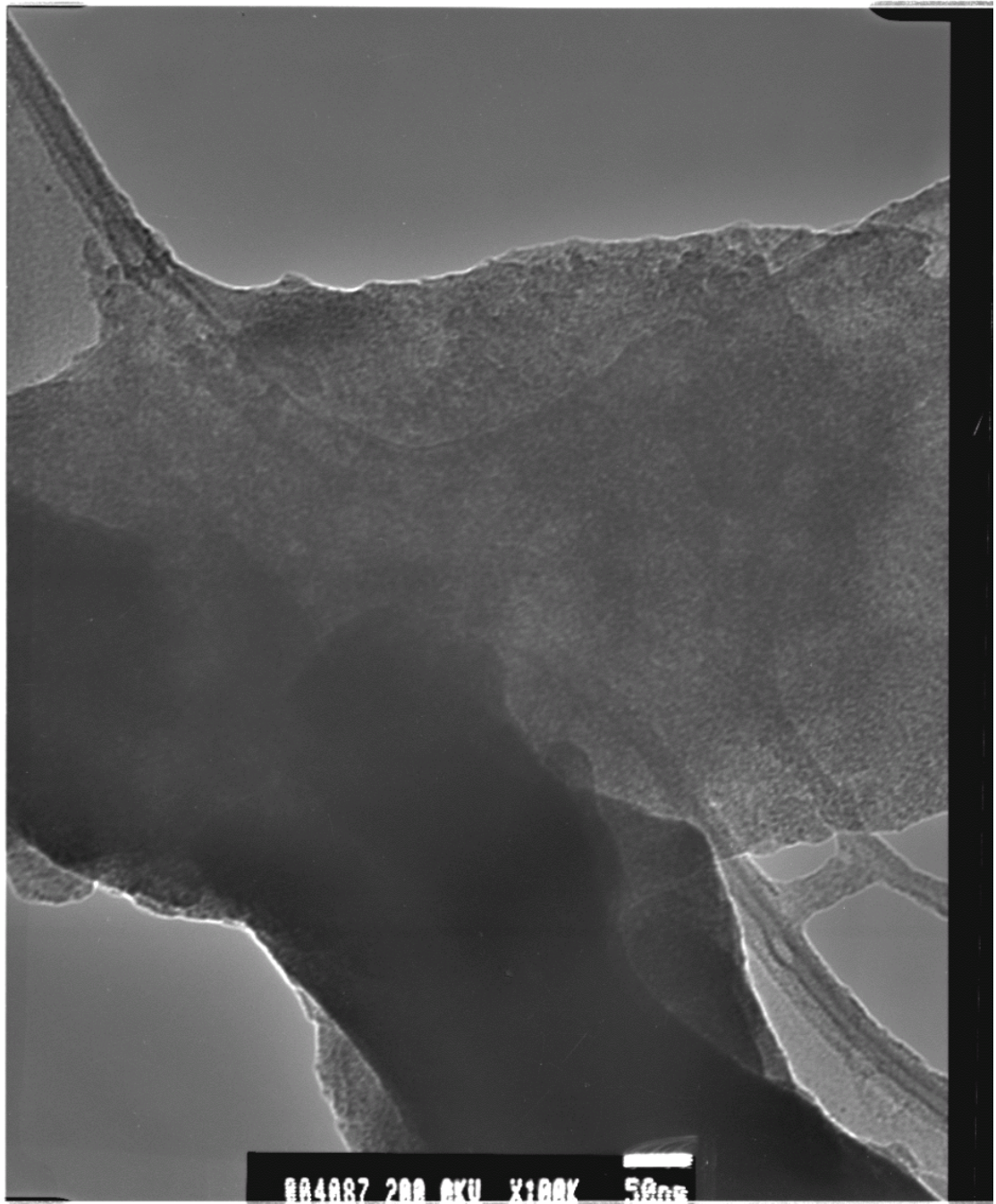
A.17: TEM micrograph of **ppt2.1**.
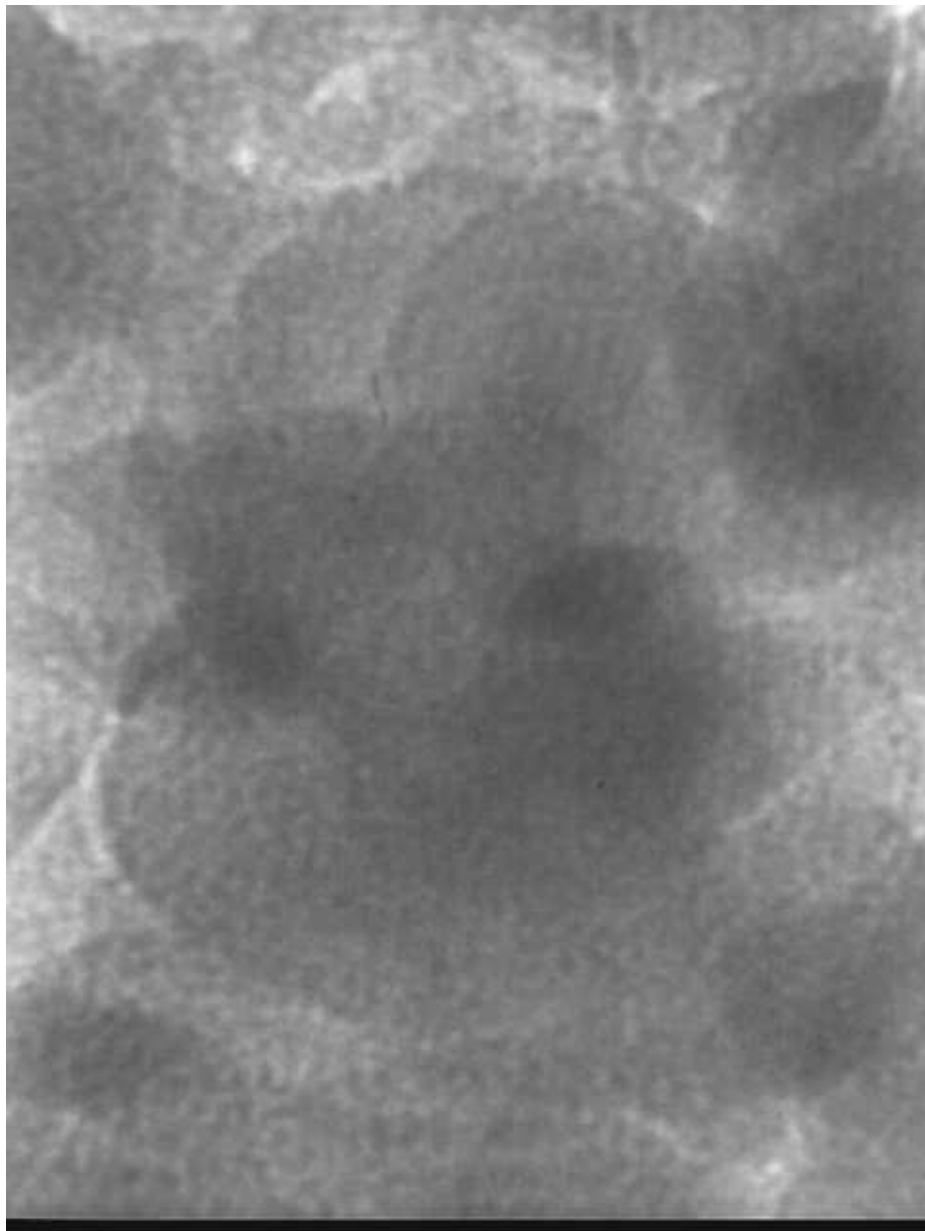
A.18: TEM micrograph of **ppt2.2**.
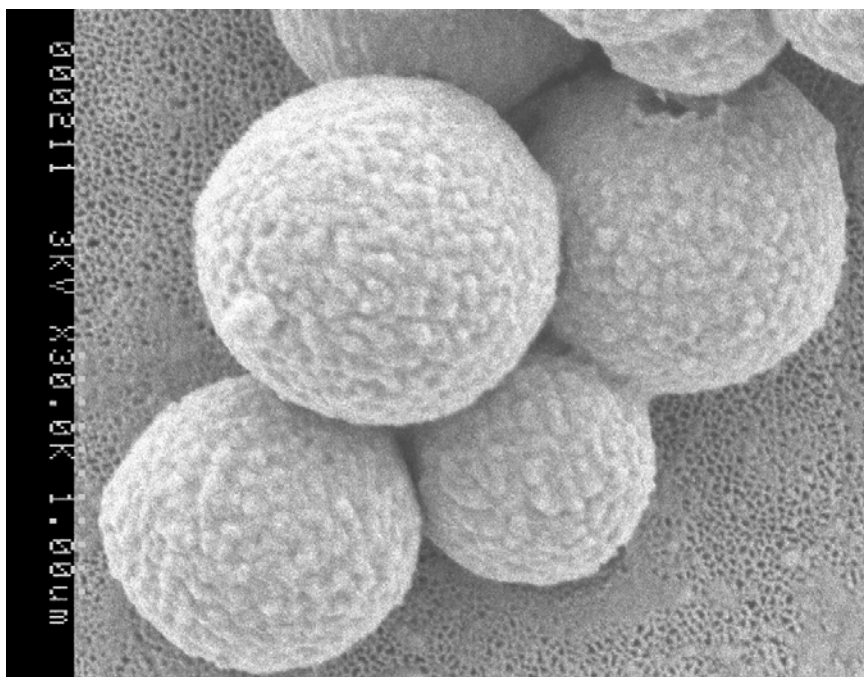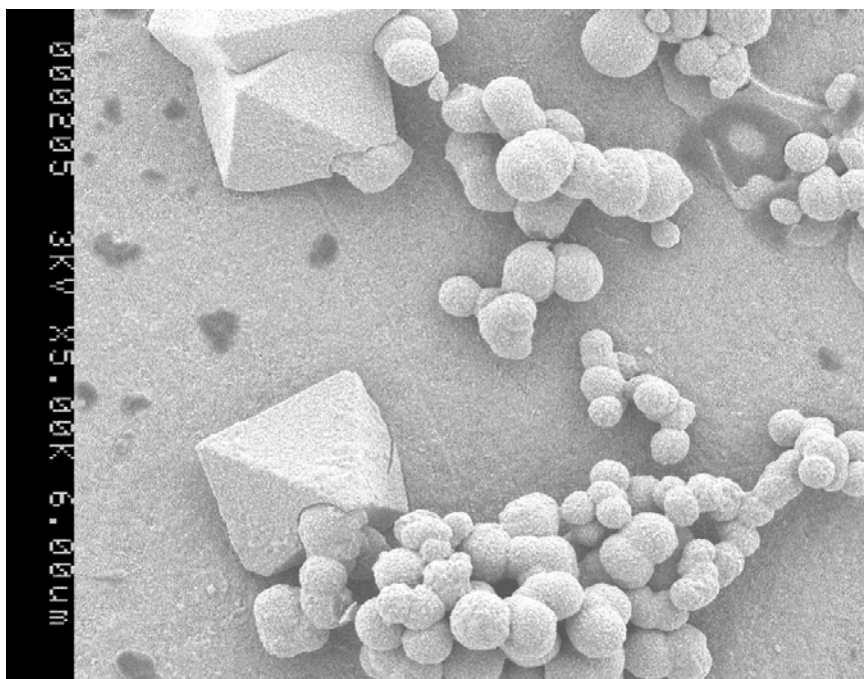
A.19: TEM micrograph of **ppt2.3a**.
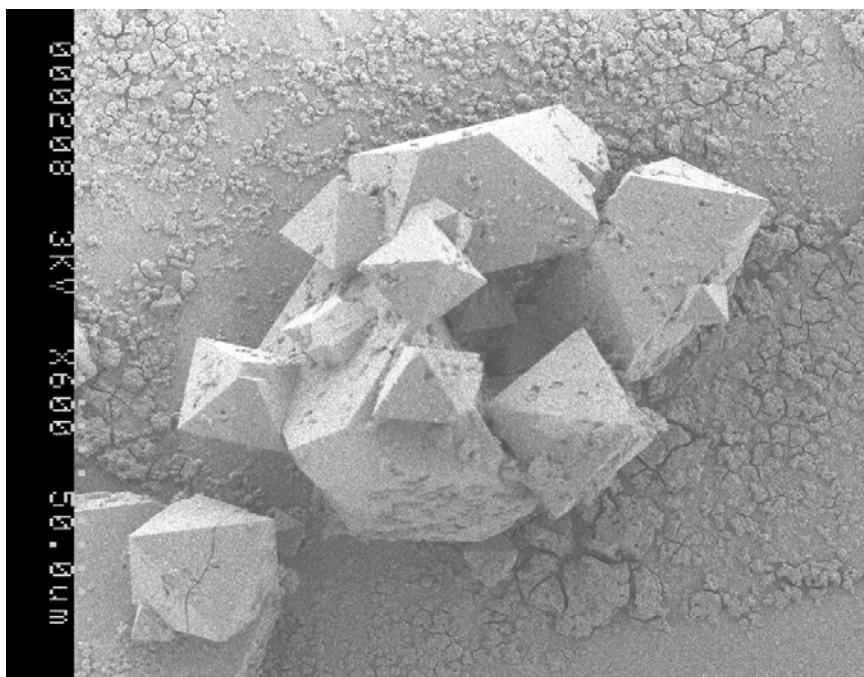
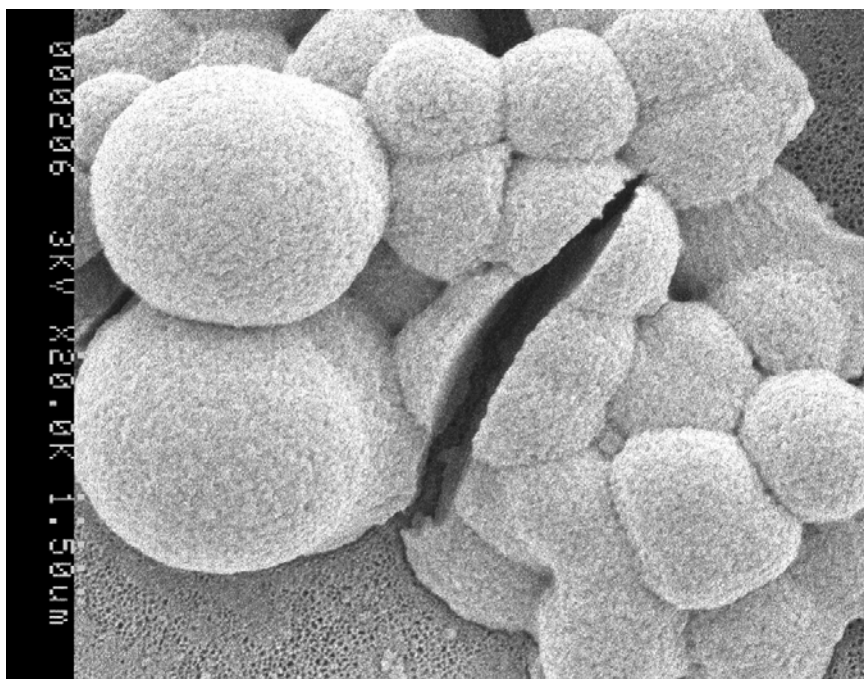**A.20:** TEM micrograph of **ppt2.3b**.

A.21: TEM micrograph of **ppt2.3c**.

A.22: SEM micrographs of precipitates from the keplerate preparation (day 1).

A.23: SEM micrographs of precipitates from the keplerate preparation (day 4).

A.24: SEM micrographs of precipitates from the keplerate preparation (day 7).
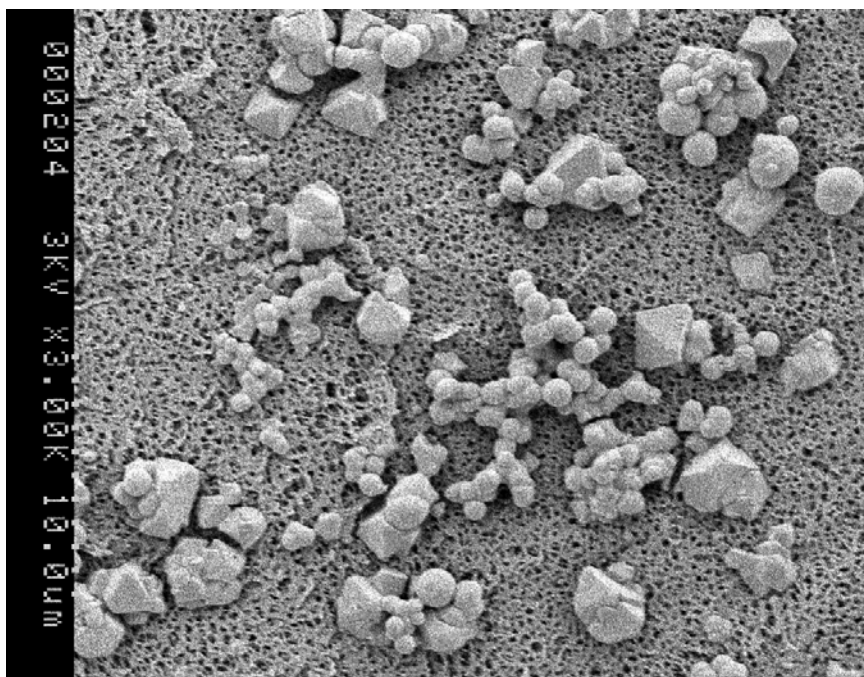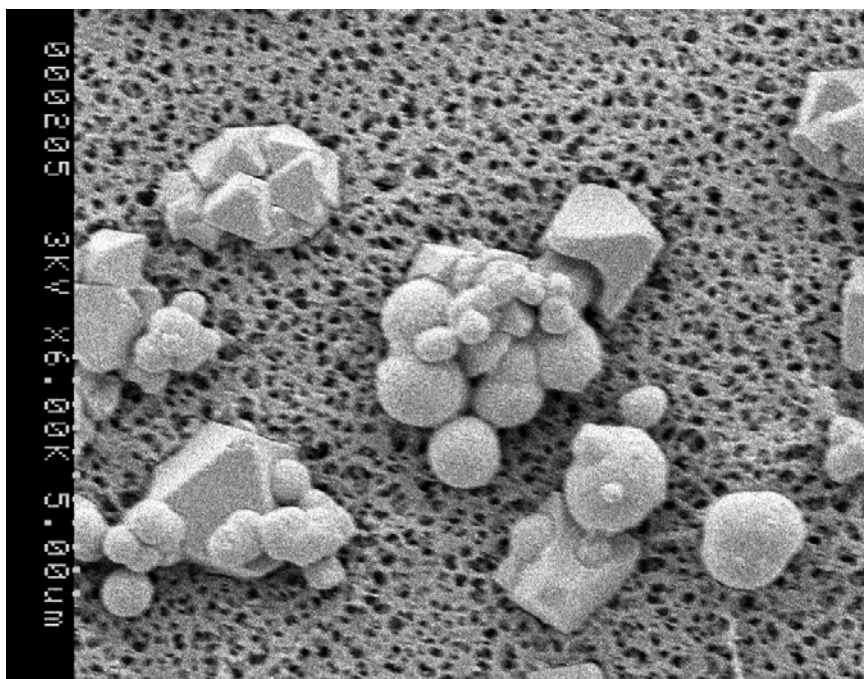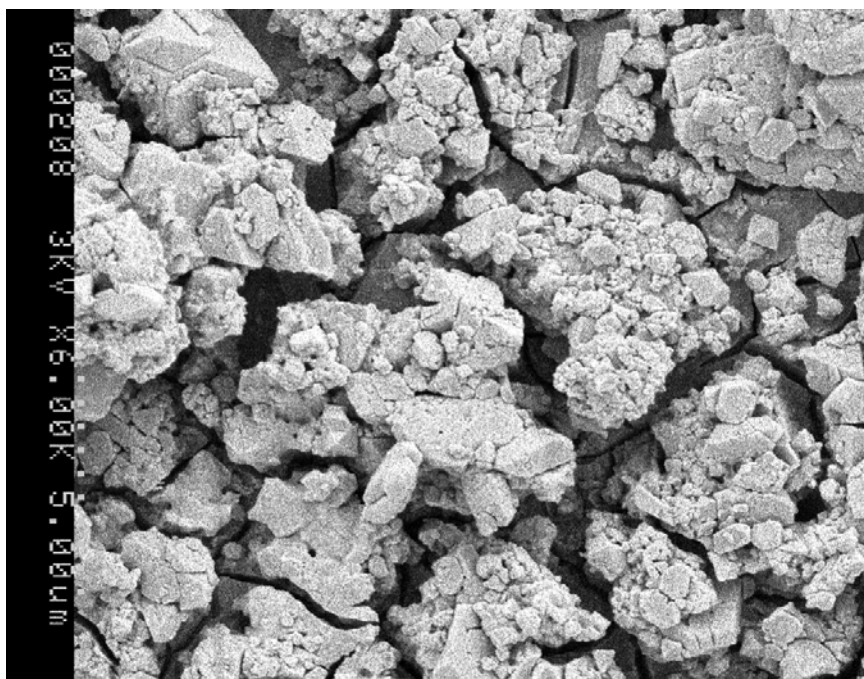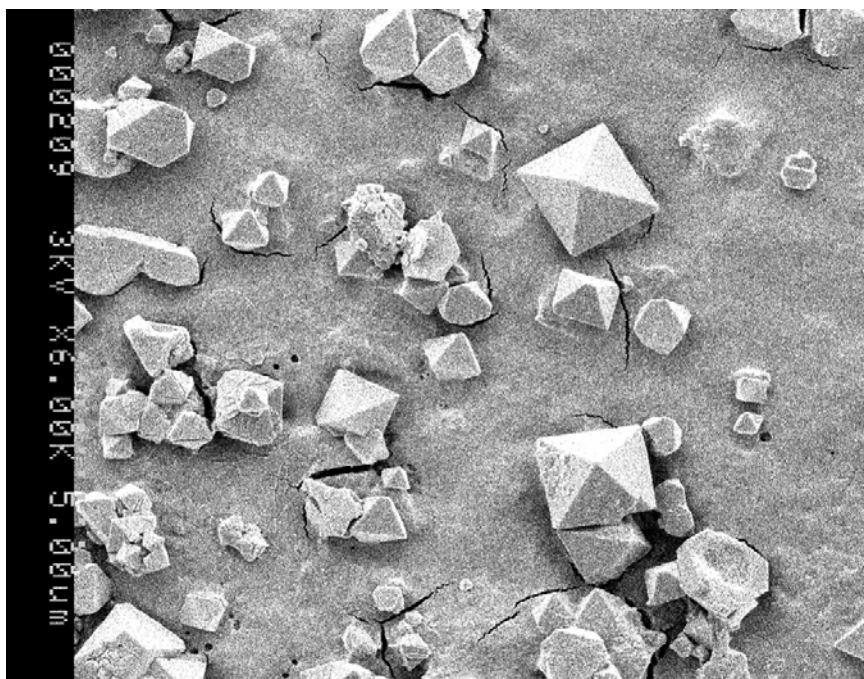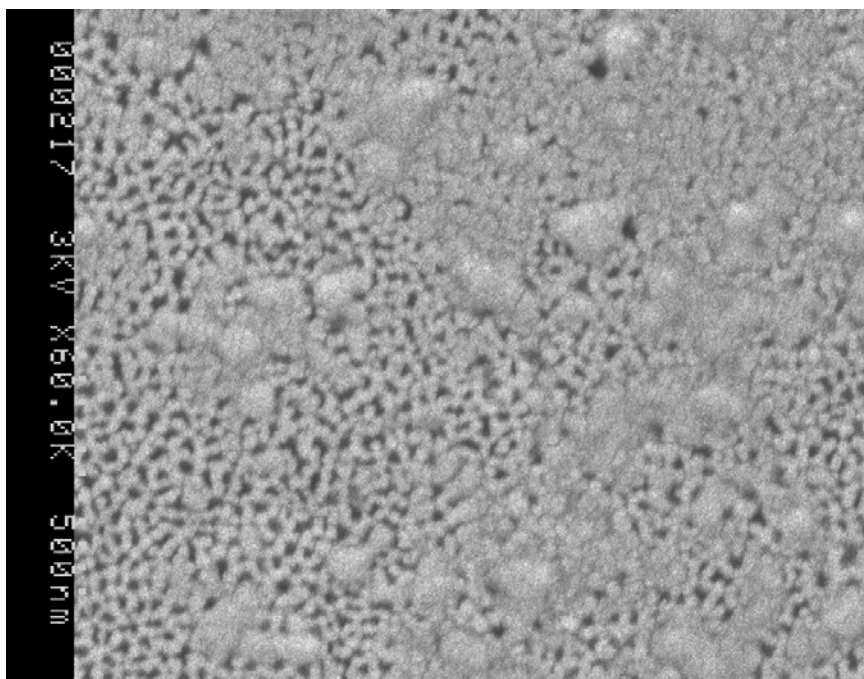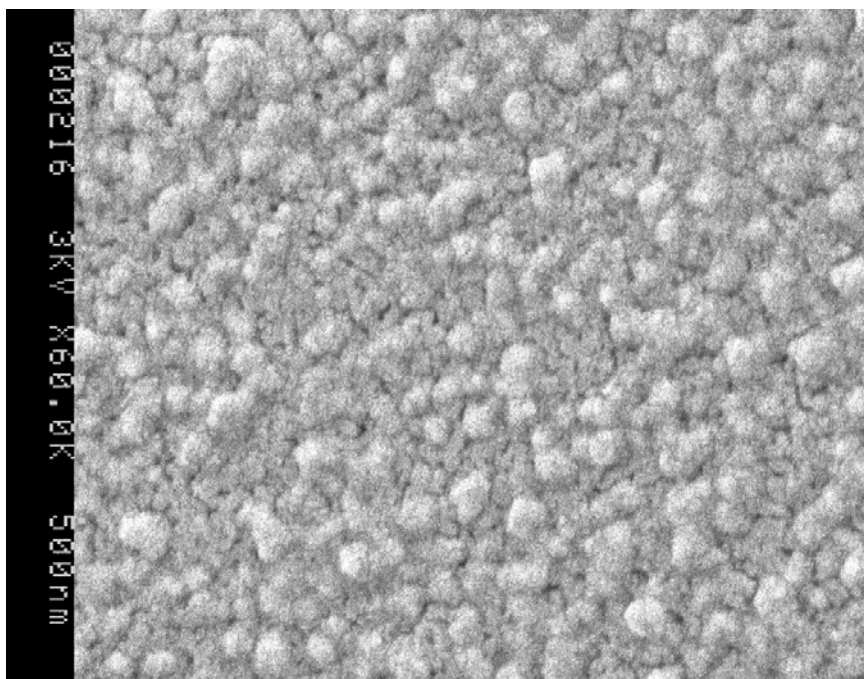
A.25: SEM micrographs of precipitates from the keplerate preparation (day 36).

A.26: SEM micrographs of the mother liquor from the keplerate preparation (day 1).

Bibliography

(1) Ander, N. G.; Keay, B. A. *Chem. Rev.* **2001**, 101, 997-1030.

(2) Atwood, J. L.; Barbour, L. J.; Nichols, P. J.; Raston, C. L.; Sandoval, C. A. *Chem.-Eur. J* **1999**, 5, 990-996.

(3) Beckett, R.; Hart, B. T. In *Environmental Particles*; Buffle, J., van Leeuwen, H. P., Eds.; Lewis Publishers: Boca Raton, FL, **1993**; Vol. 2., pp165-205.

(4) Beckett, R.; Jue, Z.; Giddings, J. C. *Environ. Sci. Technol.* **1987**, 21, 289-295.

(5) Berzelius, J. J. Beitrag zur näheren Kenntniss des Molybdäns. *Poggend. Ann. Phys. Chem.* **1826**, 6, 369-392.

(6) Bethune, D. S.; Johnson, R. D.; Salem, J. R.; de Vries, M. S.; Yannoni, C. S. *Nature* **1993**, 366, 123-128.

(7) Branda, N.; Grotzfeld, R. M.; Valdes, C.; Rebek, J. Jr*. J. Am. Chem. Soc.* **1995**, 117, 85-88.

(8) Branda, N.; Wyler, R.; Rebek, J. Jr. *Science* **1994**, 263, 1267-1269.

(9) Böhm, V. P. W.; Hermann, W. A. *Eur. J. Org. Chem.* **2000**, 3679-3681.

(10) Buszek, K. R.; Yeong, J. *Synth. Commun.* **1994**, 24, 2461-2472.

(11) Canceill, J.; Lacombe, L.; Collet, A. *J. Am. Chem. Soc.* **1986**, 108, 4230-4232.

(12) Caspar, D. L. D.; Klug, A. *Cold Spring Harbor Symp. Quant. Biol.* **1962**, 27, 1.

(13) Caulder, D. L.; Powers, R. E.; Parac, T. N.; Raymond, K. N. *Angew. Chem. Int. Ed. Engl.* **1998**, 37, 1840-1843.

(14) Chand, D. K.; Biradha, K.; Fujita, M.; Sakamoto, S.; Yamaguchi, K. *Chem. Commun.* **2002**, 2486-2487.

(15) Chen, B.; Beckett, R. *Analyst* **2001**, 126, 1588-1593.

(16) Chen, B.; Shand, C. A.; Beckett, R. *J. Environ. Monit.* **2001**, 3, 7-14.

(17) Chen, X. L.; Jenekhe, S. A. *Langmuir* **1999**, 15, 8007-8017.

(18) Clarkson, P. J.; Poole, D. J.; Rya, C. K.; Sharifi, V. N.; Swithenbank, J.; Waarlo, H. –J.; Ardelt, D.; Falk, H. *Anal. Bioanal. Chem.* **2003**, 377, 39-47.

(19) Clegg, W.; Errington, R.; Fraser, K. A.; Lax, C.; Richards, D. G. In *Polyoxometalates: from Platonic Solids to Anti-Retroviral Activity;* Pope, M. T., Müller, A., Eds.; Kluwer Academic Publishers: Dordrecht, The Netherlands, **1994**, p113.

(20) Cram, D. J.; Tanner, M. E.; Thomas, R. *Angew. Chem. Int. Ed. Engl.* **1991**, 30, 1024-1027.

(21) Davidson, L.; Freebairn, K. W.; Russell, A. T.; Trivedi, H. S.; Hayes, W. *Synlett* **2002**, 251-254.

(22) Day, A.; Blanch, R. J.; Arnold, A. P.; Lorenzo, S.; Lewis, G. R.; Dance, I. *Angew. Chem. Int. Ed. Engl.* **2002**, 41, 275-277.

(23) Douglas, T.; Young, M. *Nature* **1998**, 393, 152-155.

(24) Dubuis, M.; Deme, B.; Culik-Krzywichi, T.; Dedieu, J-C.; Vautrin, C.; Desert, S.; Perez, E.; Zemb, T. *Nature* **2001**, 411, 672-675.

(25) Dunkel, M.; Beckett, R.; Tri, N.; Caldwell, K. D. *J. Microcolumn Sep.* **1997**, 9, 177-183.

(26) Dziunikowski, B. *Energy dispersive x-ray fluorescence analysis*, Elsevier, **1989**.

(27) Edelmann, F. T. *Angew. Chem. Int. Ed. Engl.* **1995**, 34, 981-985.

(28) Farina, V.; Baker, S. R.; Benigni, D. A.; Sapino, C. *Tetrahedron Lett.* **1988**, 29, 5739-5742.

(29) Faul, C. F. J.; Antonietti, M. *Adv. Mater.* **2003**, 15, 673-683.

(30) Filella, M.; Zhang, J.; Newman, M. E.; Buffle, J. *Collids Surf. A: Physicochem. Eng. Aspects* **1997**, 120, 27-46.

(31) Fujita, M.; Umemoto, K.; Yoshimura, M.; Fujita, N.; Kusukawa, T.; Biradha, K. *Chem. Commun.* **2001**, 509-518.

(32) Giddings, J. C. *Chemical and Engineering News*, **1988**, 66, 35.

(33) Giddings, J. C. *Science* **1993**, 260, 1456-1465.

(34) Giddings, J. C. *Sep. Sci. Technol.* **1984**, 19, 831-847.

(35) Giddings, J. C.; Chen, X.; Wahlund, K. G.; Myers, M. N. *Anal. Chem.* **1987**, 59, 1957-1962.

(36) Giddings, J. C.; Myers, M. N.; Caldwell, K. D.; Fisher, S. R. *Methods Biochem. Anal.* **1980**, 26, 79-136.

(37) Glemser, O.; Lutz, G. *Z. Anorg. Allg. Chem.* **1951**, *264*, 17-33.

(38) Gorse, J.; Schunk, T. C.; Burke, M. F. *Sep. Sci. Technol.* **1985**, 19, 1073-1085.

(39) Gouzerh, P; Proust, A. *Chem. Rev.* **1998**, 98, 77-112.

(40) Hassellov, M.; Lyven, B.; Beckett, R. *Environ. Sci. Technol.* **1999**, 33, 4528-4531.

(41) Heinz, T.; Rudkevich, D. M.; Rebek, J. Jr. *Nature* **1998**, 394, 764-766.

(42) Hille, R. *Trends in Biochemical Sciences*, **2002**, 27, 360-367.

(43) Hundertmark, T.; Littke, A. F.; Buchwald, S. L.; Fu, G. C. *Org. Lett.* **2002**, 2, 1729-1731.

(44) Janca, J. *Chromatogr. Sci.* **1988**, 39, 336 pp.

(45) Jenekhe, S. A.; Chen, X. L. *Science* **1998**, 279, 1903-1907.

(46) Jeon, S. J.; Nyborg, A.; Schimpf, M. E. *Anal. Chem.* **1997**, 69, 3442-3450.

(47) Kabalka, G. W.; Wang, L.; Namboochiri, V.; Pagni, R. M. *Tetrahedron Lett.* **2000**, 41, 5151-5154.

(48) Kajigaeshi, S.; Kakinami, H.; Yamasaki, H.; fujisaki, S.; Kondo, M.; Okamoto, T. *Chem. Lett.* **1988**, 795-798.

(49) Kang, J.; Rebek, J. Jr. *Nature* **1996**, 382, 239-241.

(50) Kiriy, A.; Gorodyska, G.; Minko, S.; Jaeger, W.; stepánek, P.; Stamm, M. *J. Am. Chem. Soc.* **2002**, 124, 13454-13462.

(51) Lautrette, C.; Cardot, P. J. P.; Vermot-Desroches, C.; Wijdenes, J.; Jauberteau, M. O.; Battu, S. *J. Chromatogr. B.* **2003**, 791, 149-160.

(52) Lee, H. B.; Huh, D. H.; Oh, J. S.; Min, G-H.; Kim, B. H.; Lee, D. H.; Hwang, J. K.; Kim, Y. G. *Tetrahedron* **2001**, 57, 8283-8290.

(53) Lee, H. K.; Williams, S. K. R.; Anderson, S. D.; Anchordoquy, T. J.; *Anal. Chem.* **2001**, 73, 837-843.

(54) Levine, A.J. *Viruses*, W. H. Freeman, New York, **1992**

(55) Liu, T. *J. Am. Chem. Soc.* **2002**, 124, 10942-10943.

(56) Liu, T. *J. Am. Chem. Soc.* **2003**, 125, 312-313.

(57) Liu, T.; Wan, Q.; Xie, Y.; Burger, C.; Liu, L. –Z.; Chu, B. *J. Am. Chem. Soc.* **2001**, 123, 10966-10972.

(58) Luetzen, A.; Renslo, A. R.; Schalley, C. A.; O'leary, B. M.; Rebek, J. Jr. *J. Am. Chem. Soc.* **1999**, 121, 7455-7456.

(59) MacGillivray, L. R.; Atwood, J. L. *Angew. Chem. Int. Ed.* **1999**, 38, 1018-1033.

(60) MacGillivray, L. R.; Atwood, J. L. *Nature* **1997**, 389, 469-472.

(61) Meissner, R. S.; de Mendoza, J.; Rebek, J. Jr. *Science* **1995**, 270, 1485-1488.

(62) Miller, M. W.; Johnson, C. R. *J. Org. Chem.* **1997**, 62, 1582-1583.

(63) Moon, M. H. In *Field-flow Fractionation handbook*; Schimpf, M. E.; Caldwell, K.; Giddings, J. C., Eds.; Wiley-Interscience: New York, **2000**, pp383-396.

(64) Mori, A.; Kawashima, J.; Shimada, T.; Suguro, M.; Hirabayashi, K.; Nishihara, Y. *Org. Lett.* **2000**, 2, 2935-2937.

(65) Müller, A.; Diemann, E.; Kuhlmann, C.; Eimer, W.; Serain, C.; Tak, T.; Knöchel, A.; Pranzas, P. K. *Chem. Comm.* **2001**, 1928-1929.

(66) Müller, A.; Diemann, E.; Shah, S. Q. N.; Kuhlmann, C.; Letzel, M. C. *Chem. Commun.* **2002**, *222*, 440-441.

(67) Müller, A.; Kögerler, P.; Bögge, H. *Structure and Bonding*, **2000**, *96*, 203-236.

(68) Müller, A.; Kögerler, P.; Dress, A. W. M. *Coord. Chem. Rev.* **2001**, 222, 193-218.

(69) Müller, A.; Koop, M.; Bogge, H.; Schmidtmann, M.; Beugholt, C. *J. Chem. Soc. Chem. Comm.* **1998**, 1501-1502.

(70) Müller, A.; Krickemeyer, E.; Bögge, H.; Schmidtmann, M.; Peters, F. *Angew. Chem. Int. Ed.* **1998**, *37*, 3360-3363.

(71) Müller, A.; Krickemeyer, E.; Meyer, J.; Bögge, H.; Peters, F.; Plass, W.; Diemann, E.; Dillinger, S.; Nonnenbruch, F.; Randerath, M.; Menke, C. *Angew. Chem., Int. Ed.* **1995**, 34, 2122-2124.

(72) Müller, A.; Meyer, J.; Krickemeyer, E.; Beugholt, C.; Bögge, H.; Peters, F.; Schmidtmann, M.; Kögerler, P.; Koop, M. J. *Chem. Eur. J.* **1998**, *4*, 1000-1006.

(73) Müller, A.; Meyer, J.; Krickemeyer, E.; Diemann, E. *Angew. Chem. Int. Ed.* **1996**, *35*, 1206-1208.

(74) Müller, A.; Sarkar, S.; Shah, S. Q. N.; Bögge, H.; Schmidtmann, M.; Sarkar, S.; Kögerler, P.; Hauptfleisch, B.; Trautwein, A. X.; Schünemann, V. *Angew. Chem., Int. Ed.* **1999**, 38, 3238-3241.

(75) Müller, A.; Serain, C. *Acc. Chem. Res.* **2000**, 33, 2-10.

(76) Olenyuk, B.; Whiteford, J. A.; Fechtenkötter, Stang, P. J. *Nature* **1999**, 398, 796-799.

(77) Orr, G. W.; Barbour, J.; Atwood, J. L. *Science* **1999**, 285, 1049-1052.

(78) Parac, T. N.; Caulder, D. L.; Raymond, K. N. *J. Am. Chem. Soc.* **1998**, 120, 8003-8004.

(79) Petroski, J. M.; Green, T. C.; El-sayed, M. A. *J. Phys. Chem. A.* **2001**, 105, 5542-5547.

(80) Petteys, M. P.; Schimpf, M. E. *J. Chromatogr.* **1998**, 816, 145-158.

(81) Pope, M. T. in *Comprehensive Coordination Chemistry*, *Vol. 3.* Eds.: Wilkinson, G.; Gillard, R. D.; McCleverty, J. A. Pergamon Press, **1987**, pp. 1023-1058.

(82) Pope, M. T. *Heteropoly and Isopoly Oxometalates*; Springer-Verlag: New York, **1983**.

(83) Pope, M. T.; Müller, A. *Angew. Chem. Int. Ed. Engl.* **1991**, 30, 34-48.

(84) Pope, M. T., Müller, A., Eds. *Polyoxometalates: From Platonic Solids to Anti-Retroviral Activity:* Kluwer Academic Publishers: Dordrecht, The Netherlands, **1994**.

(85) Proust, A.; Villanneau, R. In *Polyoxometalate Chemistry, From Topology via Self-Assembly to* Applications; Pope, M. T., Müller, A., Eds.; Kluwer Academic Publishers: Dordrecht, The Netherlands, **2001**, p23-38.

(86) Rebek, J. Jr. *Acc. Chem. Res.* **1999**, 32, 278-286.

(87) Russ, J. C. *Fundamentals of energy dispersive x-ray analysis*, Butterworths, **1984**.

(88) Saito, I.; Yamaguchi, K.; Nagata, R.; Murahashi, E. *Tetrahedron Lett.* **1990**, 31, 7469-7472.

(89) Schimpf, M.; Caldwell, K. D.; Giddings, J. C. *Field-flow Fractionation Handbook*, John Wiley: New York, **2000**.

(90) Schinner, F. B. J.; Audrieth, L. F.; Gross, S. T.; McClellan, D. S.; Seppi, L. J. *J. Am. Chem. Soc.* **1942**, *64*, 2543-2545.

(91) Schiundu, P. M.; Liu, G.; Giddings, J. C. *Anal. Chem.* **1995**, 67, 2705-2713.

(92) Schneler, C.; Caruso, F. *Biomacromolecules* **2001**, 2, 921-926.

(93) Sharma, C. V. K.; Clearfield, A. *J. Am. Chem. Soc.* **2000**, *122*, 1558-1559.

(94) Shen, W.; Thomas, S. A. *Org. Lett.* **2000**, 2, 2857-2860.

(95) Sherman, J. C.; Knobler, C. B.; Cram, D. J. *J. Am. Chem. Soc.* **1991**, 113, 2194-2204.

(96) Sonogashira, K. In *Comprehensive Organic Synthesis*; Trost, B. M., Eds; Pergamon: New York, **1991**, Chapter 2.4.

(97) Sonogashira, K. In *Metal-Catalyzed Cross-Coupling Reactions*; Diederich, F., Stang, P. J., Eds.; Wiley-VCH: New York, **1998**, Chaper 5.

(98) Sonogashira, K.; Tohda, Y.; Hagihara, N. *Tetrahedron Lett.* **1975**, 4467-4470.

(99) Souchay, P. 'Polyanions et polycations', Oauthier-Villars, **1963**.

(100) Treadwell, W. D.; Schaeppi, Y. *Helv. Chim. Acta.* **1946**, *29*, 771-783.

(101) Tri, N.; Caldwell, K.; Beckett, R. *Anal. Chem.* **2000**, 72, 1823-1829.

(102) Umemoto, K.; Yamaguchi, K.; Fujita, M. *J. Am. Chem. Soc.* **2000**, 122, 7150-7151.

(103) Volkmer, D.; Du Chesne, A.; Müller, A.; *J. Am. Chem. Soc.* **2000**, 122, 1995-1998.

(104) Wyler, R.; de Mendoza, J.; Rebek, J. Jr. *Angew. Chem. Int. Ed. Engl.* **1993**, 32, 1699-1701.

(105) Xia, W-S.; Schmehl, R. H.; Li, C-J. *Tetrahedron* **2000**, 56, 7045-7049.

(106) X-ray structure of Mo$\{_{132}\}$ keplerate (CSD-410097, Fachinformationszentrum Karlsruhe, CRYSDATA@FIZ-Karlsruhe.DE) had Mo-Mo distances 2.6-3.9 Å.

(107) Xu, R. *Particle Characterization: Light Scattering Methods Particle Technology Series*, Ed.: Scarlett, B.; Kluwer Academic Publishers, **2001**.

(108) Yanase, M.; Haino, T.; Fukazawa, Y. *Tetrahedron Lett.* **1999**, 40, 2781-2784.

(109) Zhong, Z.; Ikeda, A.; Ayabe, M.; Shinkai, S.; Sakamoto, S.; Yamaguchi, K. *J. Org. Chem.* **2001**, 66, 1002-1008.

Vita

Yan Zhu was born on the 18th of March, 1972 in Kuitun, Xinjiang, China. She got her high school diploma from No. 2 High School in Urumqi, Xinjiang in July 1989. She received her Bachelors degree in Applied Chemistry from East China University of Science & Technology in Shanghai, China in July 1993 and her Master degree from the same institution in July 1996. From 1996 to 1998 she worked as a research scientist for Shanghai Research Institute of Chemical Industry in Shanghai, China. In August of 1998, she joined the graduate program at the department of Chemistry, University of Kentucky. She will join the laboratory of Dr. David A. Jaeger in University of Wyoming as a postdoctoral associate in December 2003.

Publications resulting from this research:

1.   Yan Zhu, Arthur Cammers-Goodwin*, Bin Zhao, Alan Dozier, Elizabeth C. Dickey. "Kinetic Precipitation of Solution Phase Polyoxomolybdate Followed by TEM: A Window to Solution Phase Nanostructure". Accepted by *Chem. Eur. J.*

2.   Yan Zhu, Bailin Chen, Huijian Jiang, John P. Selegue, Arthur Cammers-Goodwin. "A Dynamic Description of the Evolution of Nanometer-scale Solution-state Species Related to the $\{Mo_{132}\}$ keplerate". Manuscript in preparation, will submit soon.

3.   Yan Zhu, Arthur Cammers-Goodwin. "Synthesis and Characterization of Sugar-modified Polyoxomolybdates and their Antibacterial Activity Study". In progress.

Yan Zhu

(Author of Dissertation)